Chemical Science

ROYAL SOCIETY OF CHEMISTRY

REVIEW

Cite this: *Chem. Sci.*, 2021, **12**, 12874

Nanofluidic osmotic power generators – advanced nanoporous membranes and nanochannels for blue energy harvesting

Gregorio Laucirica, [a] María Eugenia Toimil-Molares,[b] Christina Trautmann,[bc] Waldemar Marmisollé*[a] and Omar Azzaroni *[a]

The increase of energy demand added to the concern for environmental pollution linked to energy generation based on the combustion of fossil fuels has motivated the study and development of new sustainable ways for energy harvesting. Among the different alternatives, the opportunity to generate energy by exploiting the osmotic pressure difference between water sources of different salinities has attracted considerable attention. It is well-known that this objective can be accomplished by employing ion-selective dense membranes. However, so far, the current state of this technology has shown limited performance which hinders its real application. In this context, advanced nanostructured membranes (nanoporous membranes) with high ion flux and selectivity enabling the enhancement of the output power are perceived as a promising strategy to overcome the existing barriers in this technology. While the utilization of nanoporous membranes for osmotic power generation is a relatively new field and therefore, its application for large-scale production is still uncertain, there have been major developments at the laboratory scale in recent years that demonstrate its huge potential. In this review, we introduce a comprehensive analysis of the main fundamental concepts behind osmotic energy generation and how the utilization of nanoporous membranes with tailored ion transport can be a key to the development of high-efficiency blue energy harvesting systems. Also, the document discusses experimental issues related to the different ways to fabricate this new generation of membranes and the different experimental set-ups for the energy-conversion measurements. We highlight the importance of optimizing the experimental variables through the detailed analysis of the influence on the energy capability of geometrical features related to the nanoporous membranes, surface charge density, concentration gradient, temperature, building block integration, and others. Finally, we summarize some representative studies in up-scaled membranes and discuss the main challenges and perspectives of this emerging field.

Received 30th June 2021
Accepted 25th August 2021

DOI: 10.1039/d1sc03581a

rsc.li/chemical-science

1 Introduction

The growing demand for energy on top of the concern due to environmental pollution has triggered active research to develop new efficient ways to obtain sustainable energy.[1,2] Over the last few decades, methods based on wind, water, geothermal and solar sources have attracted special interest due to their reliability, availability, and technological potential.[3–6] In this context, the possibility to obtain salinity gradient energy (SGE) (so-called salinity gradient power or blue energy) emerges as a promising candidate due to its great theoretical potential. SGE is based on the conversion of Gibbs free energy released from the mixing of solutions with different saline concentrations into electrical energy.[7–9] It is estimated that energy of 0.8 kW h m^{-3} can be harnessed at the sea–river confluence exploiting the entropy changes involved in the mixing.[10,11]

One of the pioneering studies related to this sustainable energy was published by R. E. Pattle in 1954.[12] In this work, the author assures that the free energy involved when a river mixes with the sea is comparable to those obtainable for a waterfall of 680 ft (interestingly, nowadays the confluence is often referred to as the "silent waterfall").[8] Furthermore, the first reverse electrodialysis (RED) system was implemented by stacking cation and anion exchange membranes separated by alternating seawater and river water. Then, in 1974 Norman *et al.* designed a new way to harvest SGE by using osmotic membranes in a process called pressure retarded osmosis (PRO).[13] Except for some pioneering studies and patents

[a]*Instituto de Investigaciones Fisicoquímicas Teóricas y Aplicadas (INIFTA), Departamento de Química, Facultad de Ciencias Exactas, Universidad Nacional de La Plata, CONICET, CC 16 Suc. 4, 1900 La Plata, Argentina. E-mail: wmarmi@inifta.unlp.edu.ar; azzaroni@inifta.unlp.edu.ar; Web: http://softmatter.quimica.unlp.edu.ar; www.twitter.com/softmatterlab*

[b]*GSI Helmholtzzentrum für Schwerionenforschung, 64291 Darmstadt, Germany*

[c]*Technische Universität Darmstadt, Materialwissenschaft, 64287 Darmstadt, Germany*

published around the nineteen seventies, the difficulty to create suitable membranes was hindering further advances in the field.[14–16] Later on, advances in technology and materials science, and the development of more efficient membranes paved the way for extensive progress in this field,[17,18] to the extent that, currently, there is a broad knowledge about different approaches to efficiently harness SGE either by membrane-based processes (*e.g.* RED and PRO) or electrochemical-based methods such as capacitive mixing.[19–22] Also, some pilot plants have shown promising results demonstrating the real technological potential of the membrane-based SGE methods.[23–27] However, conventional membranes containing subnanopores exhibit limited flux ion efficiency and it is difficult to further improve their properties.

In the last few decades, the development of new nanofabrication techniques with precise control at the nanometer scale has encouraged rapid and continuous growth in the study and design of nanodevices with a wide variety of applications.[28,29] Motivated by the fascinating properties of biological ion channels and exploiting the concept of "learning from nature", the creation of platforms based on solid-state nanochannels (SSNs) has attracted the attention of the scientific community.[30–38] In this scenario, the development of membrane-containing SSNs appeared as promising components for energy harvesting systems.[39–42] The immense potential of the combination of nanotechnology and energy-related applications rapidly captured the attention of the scientific community causing full and continuous progress in the field of nanoporous membrane-based energy harvesting.[11,43]

The possibility of this new generation of nanoporous membranes to operate as energy harvesters mostly comes from the presence of charged groups on the surface of nanometric pores (this property will be addressed in more detail below). So far, different methods to harvest energy using charged nanoporous membranes have been reported including streaming current,[44] diffusion current,[45] and diffusio-osmotic current.[46] In some cases, the differences reside not only in the experimental set-up but also in the basic principles. The streaming current is generated by applying an external mechanical force such as a pressure drop.[47,48] This fact establishes the selective transport of counter-ions in the electrical double layer which enables the conversion of an external mechanical force into electrical energy. Beyond its technological relevance, this method has also become useful for physicochemical surface characterization.[49] On the other hand, the diffusion current is obtained by the exposure of an ion-selective nanoporous membrane to a gradient concentration.[50,51] As detailed below, an asymmetric electrolyte concentration combined with the membrane permselectivity promotes a net flux of counter-ions across the membrane. This results in the creation of transmembrane potential and enables the conversion of Gibbs free energy of mixing into electrical energy without applying external forces. Finally, the diffusio-osmotic current is generated in a similar way to the diffusion current, but in contrast, the phenomenon involves the energy harvesting through the osmotic pressure gradient in the interfacial diffuse layer established by the salt concentration difference.[46] The last two processes influence the SGE harnessing methods and are addressed in detail in this review.

The application of the new generation of nanoporous membranes is considered a promising strategy to exceed the commercial benchmark value of 5 W m^{-2} proposed in previous investigations for salinity gradient energy technologies.[39,41,52–56] To achieve this goal, several strategies have been reported, most of them require both the development of membranes based on new materials and the integration of functional building blocks into the membrane pores to render unique features related to the ion selectivity and flux.[57,58] However, considering the current state-of-the-art, the future of nanoporous membranes for RED remains controversial. In particular, while laboratory-scale experiments demonstrated the supremacy of the results obtained for nanoporous membranes over the traditional ones, much work is necessary to transfer these results into scaled-up systems. In particular, a close and interdisciplinary effort among engineering, materials science, nanotechnology, physical chemistry, and electrochemistry will play a crucial role in increasing energy conversion capabilities and make possible the scaling up of this technology (Fig. 1).

This article presents an overview of the state-of-the-art of nanofluidic reverse electrodialysis (NRED) employing a new generation of nanoporous membranes. The next section introduces some basic terminology that will be employed throughout the review. Then, the main fundamental concepts about ion selectivity in charged nanoporous membranes and salinity gradient energy generation principles are presented. Sections 4 and 5 are focused on the analysis of the experimental set-ups and the various nanofabrication methods, respectively. The impact of different experimental variables on the performance of NRED devices is analyzed in Section 6, while the different scaled-up devices for NRED based on multi-channel, two-dimensional (2D), and three-dimensional (3D) membranes are introduced in Section 7. Finally, the review article finishes with two sections including the upcoming challenges, the conclusions, and perspectives related to this emerging field to take a step towards the evolution of these novel innovations at the lab-scale into technological platforms with favored features both in economic and environmental terms.

2 Basic definitions

To avoid ambiguities, this brief section introduces the main conventions used in this review to describe the different nanostructures. In all cases, the term *nano* is used for structures that contain at least one dimension in the nanometric range (1–100 nm). In the case of single-pore or low pore-density systems, the term "nanochannel" will refer to channels with a high aspect ratio (length $\gg$ aperture size) whereas the term "nanopores" will be used for "channels" with a low aspect ratio (length $\sim$ aperture size).[59] Typical examples of nanochannels are those obtained in ion-track-etched membranes and anodic aluminum oxide (AAO). Typical examples of nanopores are pores obtained in atomically thin 2D membranes such as boron-nitride, SiN, or MoS_2 (Fig. 1).

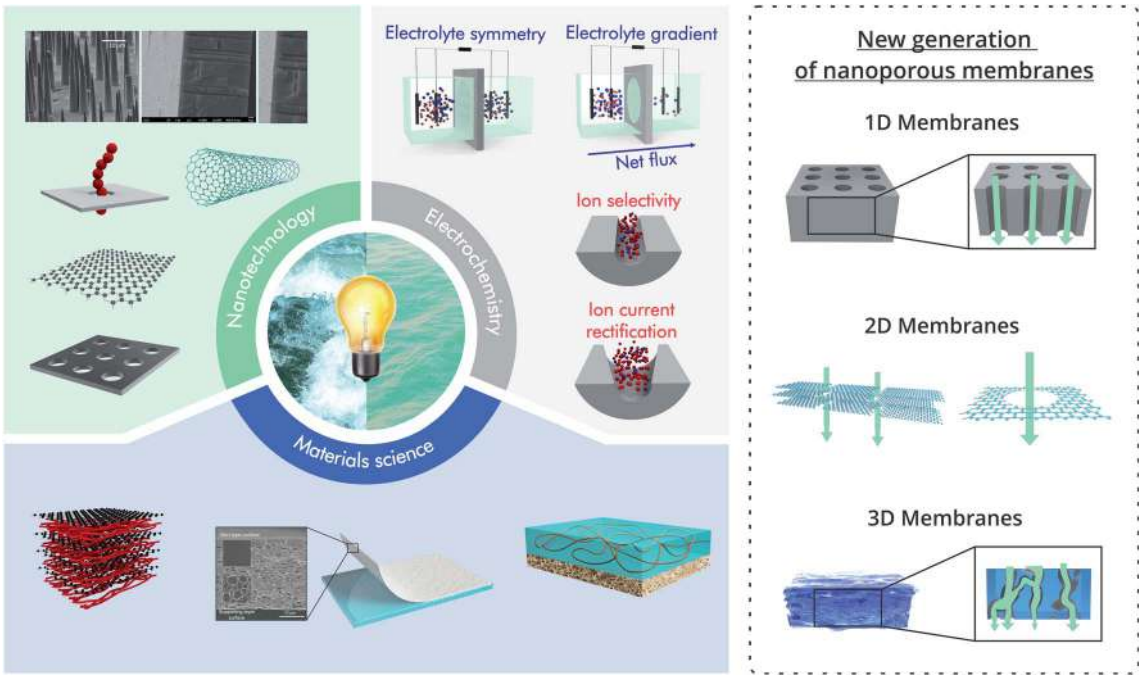

Fig. 1 Scheme illustrating the combination of the knowledge from different areas such as nanotechnology, materials science, and electrochemistry with the aim to harvest salinity gradient energy. On the right, schematic examples of the different types of nanoporous membranes are shown. Scanning electron microscopy images in the nanotechnology section were adapted with permissions from ref. 38 and 63. Copyright © 2018 WILEY-VCH Verlag GmbH & Co. KGaA, Weinheim. Copyright © 2020 Published by Elsevier B.V. Membranes in the Materials science section were reproduced with permission from ref. 64 and 65. Copyright 2020, The Author(s). Published by Springer Nature. Copyright © 2020, Oxford University Press.

In the case of up-scaled membranes (membranes with a high density of channels/pores), three major kinds of systems are addressed in this article: multi-channel membranes (or 1D membranes), 2D laminar membranes, and 3D membranes (Fig. 1). Multi-channel membranes refer to membranes containing a high density of discrete parallel oriented nanochannels such as the case of multi-channel track-etched and AAO membranes. 2D laminar membranes refer to ultrathin membranes of large lateral dimensions created by the stacking of nanosheets of materials such as MXene, graphene, or black phosphorus.[60] While it is possible to create 2D membranes with a single discrete pore *via* nanofabrication techniques such as focused ion beam or electron beam (as shown in Fig. 1), in the case of up-scaled energy conversion systems, the laminar structure (stacked nanosheets) forming interstitial nanochannels is the most common 2D membrane design.[61] Finally, 3D membranes refer to membranes consisting of micrometric networks with interconnected pores such as hydrogel-based membranes. The main aim of these definitions is to distinguish between the different mechanisms of ionic transport (Fig. 1). In the case of multi-channel and 3D membranes, the transport of ions is across the different channels and interconnected pores respectively, whereas in the case of 2D layered membranes the interstitial spaces between the nanosheets act as "lamellar channels" enabling the ion transport.[43] Finally, the terminology *nanoporous membrane* is intended to encompass all the membranes discussed throughout this review, *i.e.* commonly thin ion-selective membranes (length $\sim<$ 100 μm) with pore (or channel) size in the nanometric range.[62]

3 Osmotic energy conversion – fundamental concepts

3.1 Selectivity mechanism in charged nanoporous membranes

The immersion of a charged surface in an electrolyte solution promotes spatial ionic redistribution due to the influence of the surface electrostatic potential. The interface region in the solution is usually called the electrical double layer (EDL).[66–68] As a result of the interactions between the ions and the surface electrostatic potential in the EDL, an enrichment of counter-ions (ions with the opposite charge type to the surface charge) and a depletion of co-ions (ions with the same charge type of the surface charge) is produced. Even though it is difficult to exactly determine the extension of the EDL, under certain conditions, it is possible to obtain an equation that accounts for the behavior of the surface electrostatic potential in terms of the distance to the surface. As an example, for low electrical potentials ($<|25$ mV$|$) and planar surfaces, the electrical potential expression can be reduced to the Debye–Hückel approximation (one-dimensional):[69–71]

$$\psi(x) = \psi_0 \exp[-\kappa x] \quad (1)$$

where $\psi(x)$ is the electrostatic potential at distance x from the charged surface with respect to the potential in the bulk volume, ψ_0 is the electrostatic potential at the charged surface ($x = 0$) with respect to the potential in the bulk and κ is a decay constant related to the Debye length (λ_D) as follows (for a monovalent salt 1 : 1):

$$\lambda_D = \frac{1}{\kappa} = \sqrt{\frac{\varepsilon\varepsilon_0 k_B T}{2C_0 e^2}} \quad (2)$$

where k_B is the Boltzmann constant, T is the temperature, C_0 is the salt concentration, e is the electron charge and, ε_0 and ε are the vacuum and solvent permittivity, respectively. λ_D is usually referred to as the characteristic thickness of the electrical double layer and, as shown in eqn (2), it only depends on the temperature and bulk ion concentration ($C_0 = C(x \rightarrow \infty)$) (Fig. 2(a)). For different salt concentrations, it follows from eqn (1) that the electrical surface potential vanishes most rapidly for increasing bulk concentrations due to the more effective screening of surface charges (Fig. 2(a)). Furthermore, considering these expressions and the Boltzmann equation, a relationship between the anion and cation concentrations in terms of the x-distance from the charged surface can be obtained as follows:[67]

$$C_i(x) = C_0 \exp\left[\frac{-z_i\psi(x)e}{k_B T}\right] \quad (3)$$

where $C_i(x)$ is the i-ion concentration at distance x of the charged surface and z_i is the i-ion charge. Eqn (3) reveals a clear anion enrichment (counter-ion) and cation depletion (co-ion) at the vicinity of positively charged surfaces (Fig. 2(b)).

It is worth mentioning that these equations are only valid for flat surfaces and low surface electrostatic potential (*i.e.* low surface charge density) and when some of these assumptions are broken, the equations need to be modified. As an example, if cylindrical surface and Debye–Hückel approximation are assumed, a derivation in terms of the surface charge density can be obtained by applying sophisticated mathematical methods:[70]

$$\psi(r) = \sigma K_0(\kappa r)/[\varepsilon\kappa K_1(\kappa r_c)] \quad (4)$$

where r is the radial distance from the axis of the cylinder, σ is the surface charge density, r_c is the radius of the cylinder and, K_0 and K_1 are the second kind Bessel functions of zero and first order.

In contrast, if the geometry is maintained (flat surfaces) but now the surface electrostatic potential is higher than *ca.* 26 mV, the Gouy–Chapman expression becomes valid:[70,72]

$$[\exp(ze\psi(x)/2k_BT) - 1]/[\exp(ze\psi(x)/2k_BT) + 1] = \{[\exp(ze\psi_0/2k_BT) - 1]/[\exp(ze\psi_0/2k_BT) + 1]\}\exp[-\kappa x] \quad (5)$$

This equation reduces to eqn (1) when low surface electrostatic potential is considered. In comparison with eqn (1), for highly charged surfaces, the electrostatic potential predicted by eqn (5) displays a more pronounced diminution as x increases.[70,71] While flat surfaces are still considered in the deduction of this equation, this could be valid in the case of SSN with a radius much higher than the Debye length.[28]

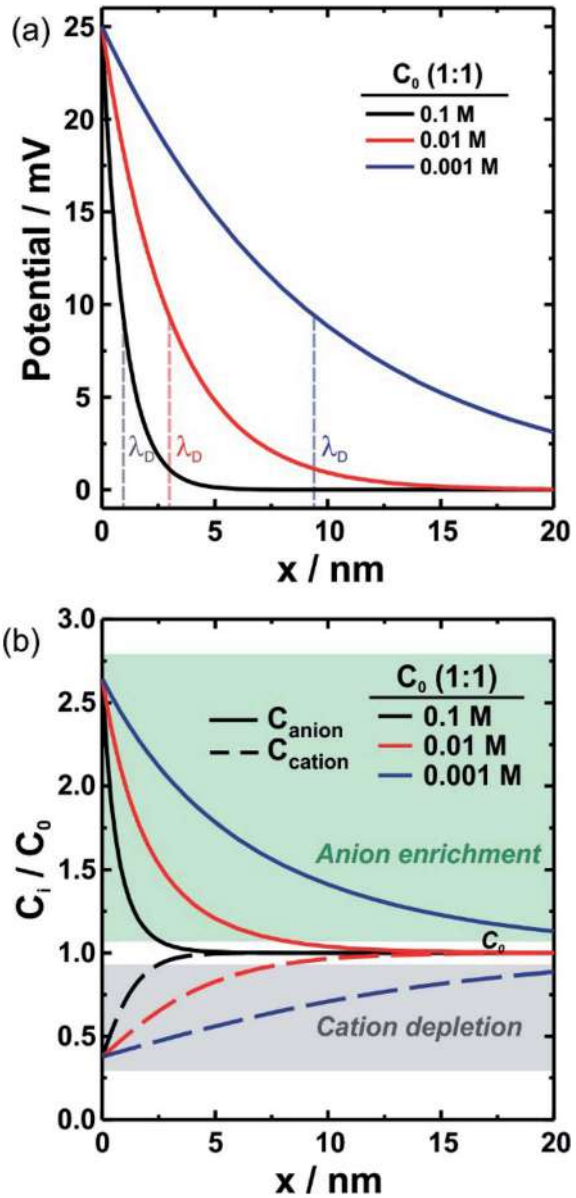

Fig. 2 (a) Electrical potential as a function of the distance to the charged surface for different monovalent electrolyte concentrations. As bulk salt concentration (C_0) increases, the electrostatic potential vanishes more abruptly. (b) Relative concentration of anion (solid lines) and cation (dashed lines) as a function of the distance to the charged surface for different monovalent bulk concentrations. Decreasing the bulk concentration causes an enrichment phenomenon at longer distances. λ_D: Debye length.

As can be seen in eqn (4) and (5), the expression complexity drastically increases as fewer assumptions are considered. In the case of nanocurved and highly charged (ψ_0 > 26 mV) surfaces, as it is the case of several SSNs, numerical methods are usually needed to describe the ion concentration inside the channel.[28,73] In this context, even though the Debye–Hückel approximation is only applicable for low surface potentials,

from a qualitative perspective, the equation not only successfully describes the effects of electrolyte concentration and valence state but also enables easy understanding of the effect of the experimental variables on the electrostatic potential. For this enormous conceptual value, in this review, we usually refer to eqn (1) and equations derived from it. Further details on these models can be found in ref. 28 and 70.

The fact that λ_D represents the characteristic length of EDL denotes great relevance for ion transport processes across nanofluidic devices with sizes in the order of λ_D. Surface charges are expected to promote a non-negligible enrichment of counter-ions inside of the nanostructure leading to an increase in the counterion concentration in the channel which results in surface-charge-governed transport.[30,74] While the relationship between the λ_D and channel size is the most used theoretical framework to explain the selectivity in channels with $r_c \sim \lambda_D$, a recent study has demonstrated that a more complete criterion of selectivity is provided by analyzing the Dukhin length (l_{Du}).[75] l_{Du} is defined as the ratio between the surface and bulk conductance and can be expressed in terms of the surface charge σ as:

$$l_{Du} = \frac{\sigma}{eC_0} \quad (6)$$

Consequently, the relationship between the l_{Du} and the channel radius r_c can be used as a reliable criterion of selectivity (or Dukhin number $Du = (l_{Du}/r_c)$). More in detail, when $l_{Du}/r_c > 1$, the system can display a selective behavior independent of the ratio λ_D/r_c. Considering the topic addressed in this review, the analysis in terms of Du allows us to conclude that, similar to traditional ion-selective membranes, it is possible to achieve ion selectivity in membranes with larger nanopores (*e.g.* 10–100 nm).[75] Finally, this ion-selective behavior arising from the sessile surface charges fulfills the prime requirement for acting as a nanofluidic RED (NRED) membrane and, therefore, allows the nanoporous membranes to become good candidates for osmotic energy conversion applications.

The slippage, another important phenomenon in nanochannels, is given by the friction of liquid/solid at the interface (for further details see ref. 72, 76 and 77). This phenomenon can have profound implications on electrical and diffusive transport and for this reason, it has been widely studied.[78–81] The slippage can be characterized with a slip length b defined as the distance where the linear extrapolation of the velocity component vanishes which depends on the fluid viscosity and the friction coefficient of the surface.[72,76,77] This parameter highly depends on the features of the surface such as roughness and the strength of the surface–liquid interaction. One of the most remarkable consequences of this phenomenon is related to the appearance of important values of zeta potentials even on surfaces with low charges.[78,79] Regarding the focus of this review, the hydrodynamic slip has been highlighted as a phenomenon that can strongly enhance blue energy conversion in RED systems by reducing the solid–liquid viscous friction.[82–84]

3.2 Salinity gradient energy

The worldwide growing demand for energy and environmental problems caused by the burning of fossil fuels leads to increased research into new ways of sustainable energy generation.[85] In this context, the salinity gradient energy (SGE) is perceived as a promising sustainable approach for electrical energy with great potential and availability.[19,85–87] The fundamental concept of SGE comes from the production of electrical energy through the Gibbs free energy involved when two electrolyte solutions of different activities are mixed.[88] The Gibbs free energy of mixing (ΔG_{mix}) released in mixing processes between concentrated and diluted solutions is described by the following equation:[19,52,89]

$$\Delta G_{mix} = G_m - (G_c + G_d) \quad (7)$$

where G_m, G_c, and G_d correspond to the Gibbs free energy of the final mix, the concentrated and the diluted solution, respectively. Note that G_m represents the final state whereas the term $G_c + G_d$ corresponds to the initial state. Also, the Gibbs free energy of the system (G) can be written as:

$$G = \sum n_i \mu_i \quad (8)$$

where n_i and μ_i are the number of moles and chemical potential of i-compound in the solution, respectively. In the absence of pressure gradients and an electrical potential applied, μ_i is expressed as:

$$\mu_i = \mu_i^0 + RT \ln(\gamma_i x_i) \quad (9)$$

with μ_i^0, γ_i and x_i being the standard chemical potential, the activity coefficient of i-compound, and the mole fraction of i-compound respectively. Finally, combining (8) and (9) and replacing n_i with the product of concentration and volume (C_iV_i), it is possible to write the following equation:[90,91]

$$\Delta G_{mix} = \sum [C_{i,m} V_m RT \ln(\gamma_{i,m} x_{i,m}) - (C_{i,c} V_c RT \ln(\gamma_{i,c} x_{i,c}) + C_{i,d} V_d RT \ln(\gamma_{i,d} x_{i,d}))] \quad (10)$$

Eqn (10) allows estimating the Gibbs free energy involved in the mixing process. For instance, ΔG_{mix} is estimated to be around −1.5 MJ (negative magnitude indicates released energy) when mixing 1 m^3 of river water (0.01 M NaCl) and 1 m^3 of seawater (0.5 M NaCl).[19] This process is irreversible and when two solutions are directly mixed, this energy is rapidly dissipated.[91,92] From this perspective, the main goal of an SGE system is focused on controlling the mixing process in such a way that the energy involved could be harnessed and efficiently converted into electrical energy. As already mentioned, several methods have been reported to tackle this goal, *e.g.* RED, diffusion-osmotic, PRO, and capacitive mixing.[91] Considering the characteristic of nanoporous membranes addressed in this review, the attention will be focused on the RED process and diffusion–osmotic mechanism.

3.3 Nanofluidic reverse electrodialysis (NRED)

In contrast to the conventional reverse electrodialysis, the NRED entails the "controlled" mixing employing nanoporous membranes rather than the conventional "dense" membranes containing sub-nanopores. The utilization of these nanoporous membranes for energy conversion has attracted special attention due to its technological potential in the energy production field ensured by the combination between ion selectivity and low resistance.[93]

When a charged membrane that contains channels is exposed to an electrolyte solution, this will attract counterions while expelling co-ions due to the electrostatic interactions (Donnan exclusion) (see Section 3.1). Considering that the counterion concentration inside of the membrane is higher than those in the adjacent solution and the opposite occurs for the co-ion, a concentration gradient is established that promotes a flux of co-ions from the solution to the membrane and in the opposite direction for the counterions. However, the net flux of ions is null since this concentration gradient is counterbalanced due to the appearance of an electrical potential, the so-called Donnan potential ψ_D, which is given by:[94–96]

$$\psi_D = \psi_m - \psi_s = \frac{1}{Fz_i} \times \left(RT \ln \frac{a_s}{a_m} + V_{m_i} \Delta\pi \right) \quad (11)$$

where ψ_m and ψ_s refer to the potential in the membrane and solution respectively, a_m and a_s are the ion activities in the membrane and solution respectively, V_{m_i} is the partial volume of i-component and $\Delta\pi$ the osmotic pressure differences between the two phases.

In the case of NRED, the method consists of exposing a membrane that contains charged nanochannels or nanopores to a concentration asymmetry, *i.e.* to electrolyte solutions with different concentrations at each side (Fig. 3). This fact establishes an ion flux across the membrane creating a transmembrane potential (E_m) with three components:[50,94,95,97,98]

$$E_m = \psi_s^\beta - \psi_s^\alpha = \psi_{diff} + (\psi''_D - \psi'_D) \quad (12)$$

where ψ_s^β and ψ_s^α refer to the potential on each side of the membrane and ψ''_D and ψ'_D to the respective Donnan potentials. ψ_{diff} denotes the diffusion potential due to the different numbers of ions transported into the channel (Fig. 3). In particular, the Donnan potential in the more concentrated reservoir (ψ'_D) is lower due to the more efficient screening of the surface charges. Also, the difference in the transport numbers of the ions (*i.e.* the fraction of the current transported by each ion) into the channel generates a concentration gradient in the membrane with its respective potential ψ_{diff}. Furthermore, as can be seen in Fig. 3 (zoom-in), at the membrane–solution interface a diffusion boundary layer is formed due to the different transport numbers of the ions in the solution compared to those in the membrane.[89,91,98] This fact causes a partial diminution in the ion activities in the concentrated reservoir whereas it produces an increase in the ion activities in the diluted reservoir. This concept, referred to as ion concentration polarization (ICP), will be addressed in detail along with the review.

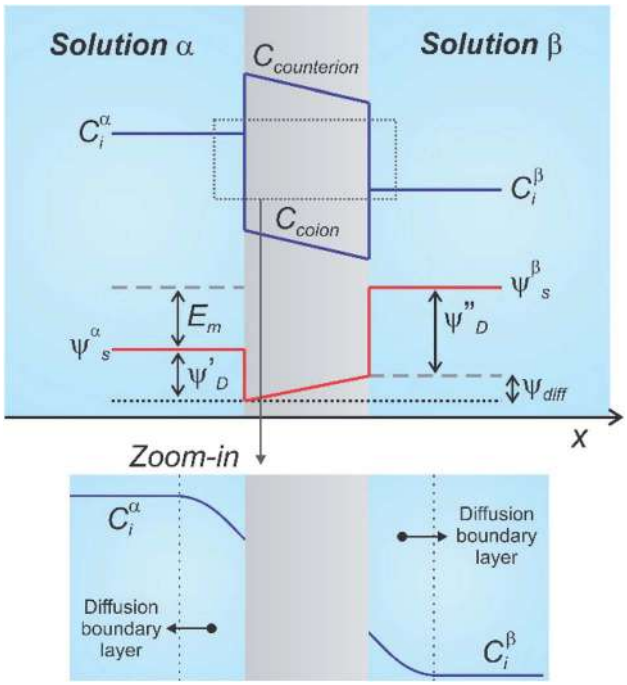

Fig. 3 Schematic representation describing the concentration (C) and electrical potentials (ψ) involved when a charged membrane is placed separating a concentration gradient. The zoom-in illustrates the formation of diffusion boundary layers at both sides of the membrane/solution interfaces. More detailed approaches are available in ref. 94, 95 and 98. E_m: membrane potential; subindex: *i*: *i*-ion; s: solution; D: Donnan; diff: diffusion.

To derive a useful expression for E_m and the experimental variables, the transference number t_i is introduced which denotes the fraction of the current carried by the i-species (I_i):[66]

$$t_i = \frac{I_i}{I} \quad (13)$$

$$\sum t_i = 1 \quad (14)$$

with I being the total current. For an electrolyte of type $A^{+n}B^{-n}$,

$$t_+ + t_- = 1 \quad (15)$$

where the sub-index ± indicates the charge of the ion.

The magnitude of E_m depends on the asymmetry of charges at each side of the membrane which is related not only to the ion activities but also to the capability of the ion to be transported through the membrane:[66,95,99]

$$\Delta G = -FE_m = \sum \frac{t_i}{z_i} \Delta\mu_i \quad (16)$$

where ΔG denotes the Gibbs free energy change due to the transport of one mole of the electrolyte from the concentrated to the diluted compartments without any change in the compartment bulk concentrations.

Considering the case of a monovalent salt:

$$E_m = -\frac{1}{F}(t_+ \Delta\mu_+ - t_- \Delta\mu_-) \quad (17)$$

Introducing the expression for the chemical potentials,

$$\Delta\mu_+ \cong \Delta\mu_- \cong RT \ln\left(\frac{a^{\beta}_{salt}}{a^{\alpha}_{salt}}\right) \quad (18)$$

where a^{β}_{salt} and a^{α}_{salt} are the salt activities in the diluted (a_L) and concentrated (a_H) reservoirs respectively. Finally,

$$E_m = (t_+ - t_-)\frac{RT}{F} \ln\left(\frac{a_H}{a_L}\right) \quad (19)$$

$$E_m = (2t_+ - 1)\frac{RT}{F} \ln\left(\frac{a_H}{a_L}\right) \quad (20)$$

Therefore, exposing a perm-selective membrane to a concentration gradient gives rise to a transmembrane voltage difference (Nernstian) that depends on both the gradient magnitude as well as the membrane capability to transport counter-ions over co-ions. Furthermore, this equation depicts the possibility to estimate the transport number under the operative conditions, and therefore, to analyze the membrane selectivity by measuring E_m.[50,100] Note that this equation was derived neglecting the water transport. If the solvent transport was considered, the final equation would look like eqn (19) but the transport numbers would be apparent rather than the real values.[95] Finally, it is worth mentioning that an equivalent equation can be derived *via* Teorell, Meyer, and Sievers theory (TMS theory) by employing eqn (12) as the starting point.[97,99]

Taking into account the existence of E_m, the electrical potential generated in the nanochannels by the ionic current can be expressed as:[101–103]

$$V_t = E_m - IR_c \quad (21)$$

where V_t is the applied external transmembrane voltage and R_c is the channel resistance (this is a simplification because, for high-pore densities, the presence of additional resistances coming from the solutions, electrodes, and interface membrane/solution should be considered). In the absence of additional voltage drops, eqn (21) indicates that E_m is acquired from the interpolation of the *I–V* curve at $I = 0$. Furthermore, this equation can be rewritten for the case of electrodes connected to an electrical load (resistance load, R_{load}):[104]

$$E_m = I \times (R + CR_{load}) \quad (22)$$

One of the most important parameters to characterize the system performance in energy-conversion is power (P):

$$P = I \times V_t \text{ or } P = I^2 \times R_{load} \quad (23)$$

Combining eqn (22) and (23), the following useful expression for P in terms of R_{load} is obtained:[101,104,105]

$$P = \frac{{E_m}^2 R_{load}}{(R_{load} + R_c)^2} \quad (24)$$

When $R_{load} = R_c$, the output power acquires the maximum value (P_{max}):

$$P_{max} = \frac{{E_m}^2}{4R_c} \quad (25)$$

Applying eqn (21) for the case $V_t = 0$ yields:

$$P_{max} = \frac{I_{osm}E_m}{4} \quad (26)$$

where I_{osm} is the osmotic current and, similar to E_m, in the absence of additional drop voltage, I_{osm} is easily extracted from the *I–V* curve. In the case of up-scaled membranes, the maximum power is usually reported in terms of the maximum power density (PD_{max}), *i.e.* the P_{max} value is divided by the area of the exposed membrane (working or testing area). As can be seen, in the case of single-pore systems, PD_{max} is determined *via* the channel cross-section area, but this value is not very relevant because the relationship between the pore-density and output power is not linear.[106]

Finally, combining (24) and (18), P_{max} can be expressed as:

$$P_{max} = \frac{\left[(2t_+ - 1)\frac{RT}{F} \ln\left(\frac{a_H}{a_L}\right)\right]^2}{4R_c} \quad (27)$$

This equation has a high conceptual relevance since it denotes the need to achieve an adequate balance among the gradient concentration, the channel resistance, and the selectivity of the nanofluidic device for optimizing P_{max}. In other words, a permselectivity membrane is not sufficient to obtain high P_{max} values. For instance, Fig. 4 shows the effects on the power of variables such as the concentration gradient, membrane resistance, and selectivity. According to eqn (27), to increase the energy harvested, the increment and diminution of ion selectivity and membrane resistance are necessary since these parameters would enable more efficient mixing (Fig. 4(a) and (b)). In the case of the gradient, an increase of the difference of concentration between the high- and low-concentration reservoirs promotes an increase in the driving force of the SGE method and thus, an increment in the power (this trend is also evidenced in eqn (10)) (Fig. 4(c)). However, it is worth mentioning that this equation only considers the resistance due to the membrane but, in practice, additional resistances that affect (*e.g.* resistances from solution and diffusion boundary layers) the output power must be considered.[107,108] For its part, variation in the reservoir concentrations can significantly affect the membrane selectivity, which would also generate a deviation from the power value predicted by eqn (27). These issues will be addressed in detail throughout the review.

Another parameter with paramount relevance for SGE systems is the efficiency (η) of the energy-conversion system which was defined by Fair and Osterle as the energy recovered compared to the ΔG_{mix} applied:[109]

$$\eta = \frac{I \times V_t}{J_s RT \ln\left(\frac{a_H}{a_L}\right)} \quad (28)$$

where J_s is the solute flux. For a monovalent salt, J_s is defined as follows:[102,109]

$$J_s = J_+ + J_- \tag{29}$$

The current generated by the selective ion diffusion can in turn be expressed in terms of the fluxes of the cation and anion:

$$I = zF(J_+ - J_-) \tag{30}$$

with z being the absolute valence number.

As the cation transference number is the cation contribution to the current, it can be defined as follows:[103]

$$t_+ = \frac{|I_+|}{|I_+| + |I_-|} = \frac{|J_+|}{|J_+| + |J_-|} \tag{31}$$

Considering that the maximum power is obtained when $R_{load} = R_c$ and therefore, $V_t = E_m/2$, the maximum efficiency (η_{max}) can be expressed as:

$$\eta_{max} = \frac{F(J_+ - J_-)E_m}{2(J_+ + J_-)RT \ln\left(\frac{a_H}{a_L}\right)} \tag{32}$$

Combining eqn (32) with eqn (19) gives

$$\eta_{max} = \frac{(J_+ - J_-)(t_+ - t_-)}{2(J_+ + J_-)} \tag{33}$$

$$\eta_{max} = \frac{(t_+ - t_-)^2}{2} \tag{34}$$

Finally, considering the definition of the transference number, eqn (34) can be rewritten:

$$\eta_{max} = \frac{(2t_+ - 1)^2}{2} \tag{35}$$

The maximum efficiency acquires values between 0 and 0.5 (or 0–50 when expressed in percentage value). Values around 0.5 can be obtained by maximizing the membrane selectivity, thus creating highly asymmetric ionic transport. This method for the efficiency calculation is an oversimplification since it does not consider other processes that contribute to the loss of efficiencies such as water transport and unutilized energy.[110] However, as we will see, it is the most common way to estimate the efficiency in blue energy systems at the lab scale.

3.4 Diffusio-osmotic mechanism

As was pointed out in a pioneering study by Derjaguin,[111] when a solid surface is exposed to a salinity gradient, an osmotic pressure gradient is generated in the diffusion layer yielding a diffusion-osmotic flow. In contrast to the NRED process (and RED), the diffusion–osmotic flow can be achieved even in membranes without ion permselectivity due to the interaction between the ions and the surface.[11,77,112] For this reason, the diffusion–osmotic process is considered an intermediate between RED and PRO. More in detail, the gradient concentration promotes an interfacial osmotic pressure gradient in the first few nanometers from the surface that generates a water flux with a plug-like profile. The velocity of this flow (V_{DO}) can be estimated with the following expression:[46]

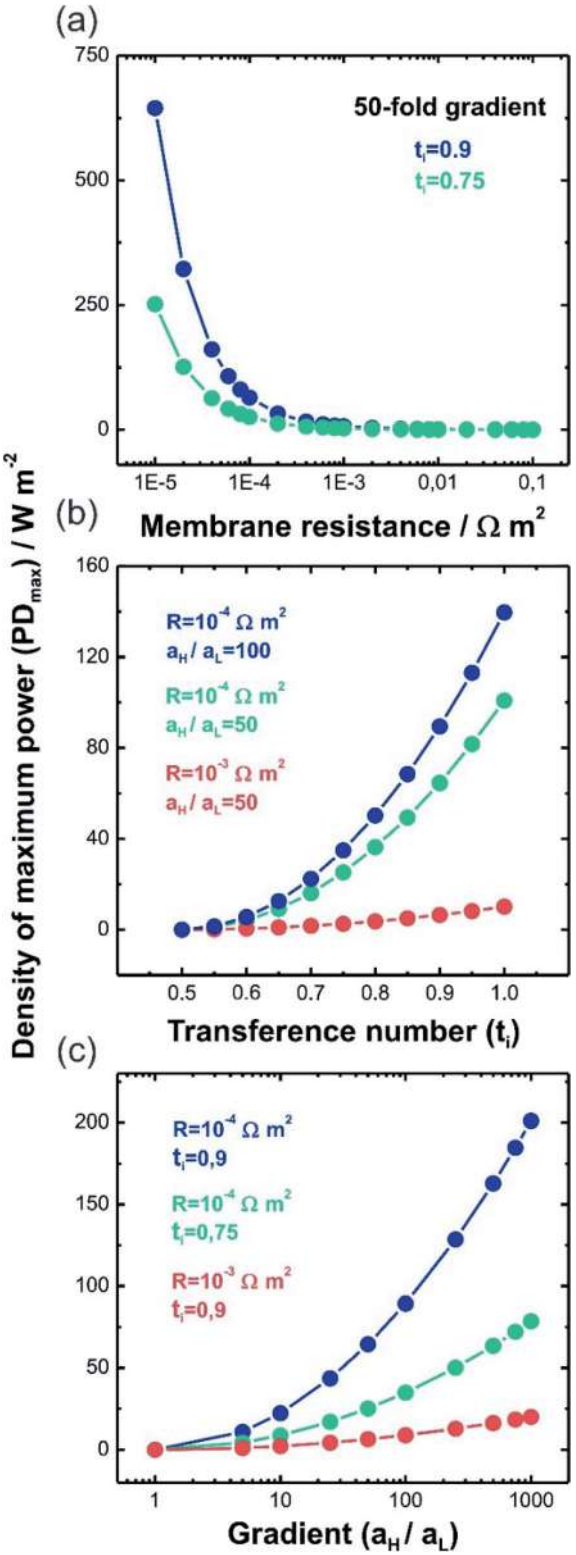

Fig. 4 Density of maximum power (PD_{max}) predicted by eqn (27) as a function of (a) membrane resistance (R), (b) transference number and (c) gradient concentration (a_H/a_L) (T = 298 K).

$$V_{DO} = \frac{k_B T}{8\pi l_B \eta} \frac{\Delta \log C}{L} \quad (36)$$

where η is the water viscosity, l_B is the Bjerrum length ($\sim$0.7 nm in water at room temperature), $\Delta \log C$ is the concentration gradient, and L the pore length. If the surface contains a net charge density (σ) different from 0, this flow carries the excess of ions and, concomitantly, generates a diffusion–osmotic current (I_{DO}) that obeys the following expression:[46]

$$I_{DO} = N 2\pi r_c \sigma V_{DO} \quad (37)$$

where N and r_c are the number and radii of the pores. It is worth mentioning that this expression is valid for highly charged surfaces. In the case of low-charge surfaces, it is expected that $I_{DO} \propto \sigma^3$.[46] For this process, the increment in the surface area entails increments in the diffusion–osmotic current.[11]

4 SGE: experimental aspects

Fig. 5(a) shows a typical half-cell (or unit cell) used for NRED (or diffusion–osmotic) experiments at a laboratory scale. The nanoporous membrane is placed in a cell and separates two reservoirs filled with two electrolyte solutions of different activities (*e.g.* NaCl or KCl) and, to obtain the osmotic energy parameters, an arrangement of two or four electrodes is connected to a potentiostat or an external circuit with a load resistance (Fig. 5(b)). Typically, this kind of lab-scale experiment is performed by using a pair of Ag/AgCl electrodes. Taking into account that each electrode is immersed in a chloride-based solution with a different activity, the cell can be represented by the following scheme:[66]

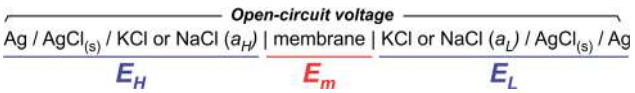

If Ag/AgCl electrodes are considered to be identical, a concentration cell is generated due to the voltage drop at the electrode surfaces. The potential magnitude of this concentration cell is E_{redox}:

$$E_{redox} = E_L - E_H = \frac{RT}{F} \ln\left(\frac{a_H}{a_L}\right) \quad (38)$$

So, under these conditions, the open-circuit voltage (OCV) is given by:

$$OCV = E_m + E_{redox} \quad (39)$$

In this way, the open-circuit voltage (OCV) or reversal voltage corresponds not only to the contribution provided by the membrane (*i.e.* E_m) but also experiences an additional voltage drop due to E_{redox}. Therefore, to obtain pure osmotic energy contribution, E_{redox} must be subtracted. This aim can be accomplished by different methods. On the one hand, the voltage drops at the electrode surface can be prevented by working with Ag/AgCl electrodes with salt bridges and immersing both electrodes in the same electrolyte concentration, typically 3 M KCl.[63,113,114] However, depending on the salt type used in the experiments, additional junction potentials must be considered.[115] In long-time experiments, ion leakage from the salt bridge can change the electrolyte concentration in the reservoirs (especially in the low concentration reservoir) which produces a negative impact on the energy performance.[51] On the other hand, if the experiments are carried out with Ag/AgCl electrodes without salt bridges, the E_{redox} contribution can be either directly estimated from eqn (38) or measured by replacing the ion-selective membrane with a non-selective membrane.[101,116,117] With E_{redox} in hand, I_{osm} and E_m are obtained applying the following expressions:[116]

$$I_{osm} = I_{SC} - I_{redox} = I_{SC} - GE_{redox} \quad (40)$$

$$E_m = OCV - E_{redox} \quad (41)$$

where I_{SC} is the short-circuit current (*i.e.* the current at $V_t = 0$ V), I_{redox} is the current due to the voltage drop at the electrode surface and G is the conductance. Note that if $E_{redox} = 0$ V due to the use of Ag/AgCl electrodes with salt bridges, $I_{osm} = I_{SC}$ and $E_m = OCV$.

Typically, there are two classical routine SGE experiments and therefore, two common ways to obtain the SGE parameters: (a) *I–V* curves by scanning the transmembrane voltage employing a potentiostat (or an ammeter with a voltage source); (b) current–load resistance (*I–R*) and power–load resistance (*P–R*) curves. In the former method, as depicted in eqn (21), the response is characterized by a linear *I–V* curve shifted from the (0;0) point (Fig. 5(c)). From the intersection in the x and y-axis, OCV and I_{SC} are obtained. Then, E_m and I_{osm} are deduced by subtracting the contribution of the redox potentials (eqn (40) and (41), if applicable). Finally, it is possible to obtain P_{max}, t_+, and η_{max} from eqn (26), (20), and (35), respectively.[63] It is worth noting that in some systems, the *I–V* response can be slightly non-linear and the employment of eqn (26) could lead to little deviations in the P_{max} estimation.[118] In these cases, representing power *vs.* voltage (*P–V*) curves and obtaining P_{max} graphically could be the best option. In the latter method, the extracted osmotic power is transferred to an external circuit with an electronic load (eqn (24)) (Fig. 5(d)). When $R_{load} = R_c$, the curve exhibits a maximum value corresponding to the maximum extracted output power.[51,101] However, some authors have reported overestimation in the P_{max} obtained by this method due to the difficulty in subtracting the redox contribution.[116,119]

To increase the voltage generated, different unit cells can be connected in series (tandem cells), or cation-selective and anion-selective membranes can be stacked alternately (full cells) separating concentrated and diluted solutions (Fig. 5(e)). In this regard, under ideal conditions, the purely osmotic open-circuit voltage linearly scales with the number (n_m) of nanoporous membranes:[52,104]

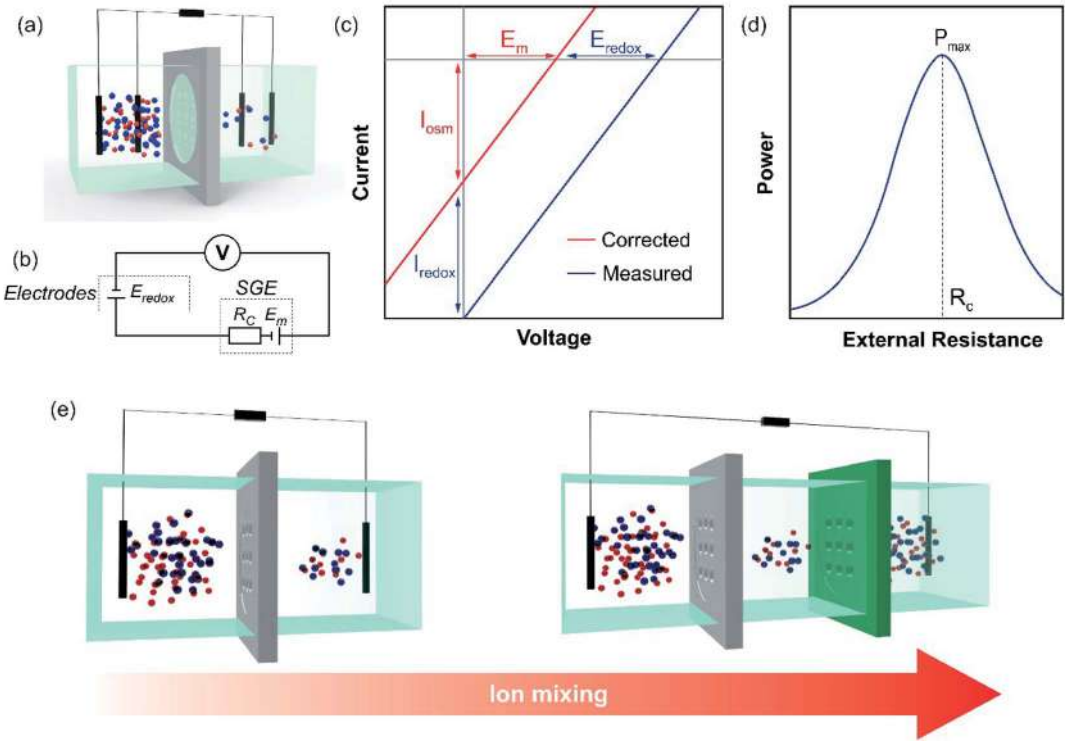

Fig. 5 (a) Schematic illustration of an experimental set-up with a four-electrode arrangement using nanofluidic reverse electrodialysis measurements. (b) Equivalent circuit diagram depicting the different contributions to the overall response. E_{redox}: voltage drop at the electrode surface; SGE: salinity gradient energy; R_c: membrane resistance and E_m: membrane potential. (c) Characteristic I–V curve in the presence of an electrolyte concentration gradient. The graph shows the redox (I_{redox} and E_{redox}) and osmotic energy contributions (I_{osm} and E_m). (d) Extracted power in terms of external resistance. Maximum power (P_{max}) is obtained when the external resistance acquires the value of membrane resistance (R_c). (e) Scheme illustrating the half (left) and full-cell (right) configurations. In the case of the full-cell configuration, the gray and green membranes correspond to cation-selective and anion-selective membranes.

$$\mathrm{OCV} = n_m E_m \tag{42}$$

In this case, E_m is the membrane potential of each cation and anion-selective membrane (considering the same permselectivity in both cases). Moreover, from a technological perspective, the use of full cells results in a promising alternative to maximize the energy extracted regarding the total volume of high- and low-concentration solutions (specific extractable energy) since, in contrast to half-cells, the mixing is due to the flux of both cations and anions.[108] It is worth mentioning that, in practice, the scale-up is not linear due to different sources of energy losses such as additional resistances which lead to the need to optimize the architecture of the cell and electrodes.[52,107,120–122] Finally, as it will be shown later, by employing full or tandem cells, several authors have demonstrated the possibility to switch on LEDs, calculators, and other electronic devices.[53,123,124]

Beyond the experimental aspect, it is possible to carry out a theoretical analysis of NRED performance by Poisson–Nernst–Planck and Navier–Stokes (PNP–NS) model-based simulations. The results based on the PNP–NS model have acquired great relevance regarding the influence of experimental variables such as length, size, electrolyte gradient, *etc.*, either in single-pore or high-pore density systems. Details about PNP–NS simulations for single and multi-channel systems are addressed in ref. 125–130.

Although routine experiments related to energy conversion are performed under asymmetric electrolyte conditions, experiments in the presence of symmetric salt concentration are very common for characterizing the ion transport properties of the nanoporous membranes. In these cases, the membrane is placed in a two-half cell separating two reservoirs filled with two identical electrolyte solutions, and two or four-electrodes are connected to a potentiostat or picoammeter (with a voltage source) in a similar way to those used for the SGE experiments (Fig. 6(a)). Commonly, a cyclic linear sweep voltage program is applied, and simultaneously, the current is recorded. As the ions are the signal carriers, the response is often called the iontronic output. Under surface-charge governed transport, symmetric membranes display an ohmic behavior, *i.e.* a linear relationship between transmembrane current and voltage, with a surface charge-dependent conductance (slope of I–V curve) (Fig. 6(b)). On the other hand, when the ion-selective membrane is asymmetric either by the presence of asymmetrical channels or asymmetric modifications, the response is characterized by an ionic current rectifying behavior (diode-like behavior) (Fig. 6(c)).[131] In other words, the platform displays a non-ohmic (non-linear) transport described by an enhanced current at

a given voltage polarity. Moreover, the rectification efficiency is quantified employing the rectification ratio (or rectification factor) which is determined from the ratio between the current in the high and low conductance branches, respectively.[132] Usually, the rectification ratio increases as the surface charge increases.[133,134] As explained below, this kind of transport provides attractive features related to energy conversion applications.[11,41,135]

5 Nanofabrication methods

One of the major challenges behind the construction of platforms based on nanoporous membranes for energy applications is centered on the reproducible synthesis of the nanostructure. For this reason, researchers have made great efforts in the study and development of new ways for the controlled fabrication of nanoporous membranes from different materials. So far, the creation of membranes containing nanopores or nanochannels with size and density well-defined has been achieved by techniques involving ion, electron beams, and electrochemical methods. It should be noted that the synthesis protocols for ultrathin, two-dimensional (2D), and three-dimensional (3D) membranes, are very different. This section is a summary of drilling and synthesis methods employed in the design of nanoporous membranes.

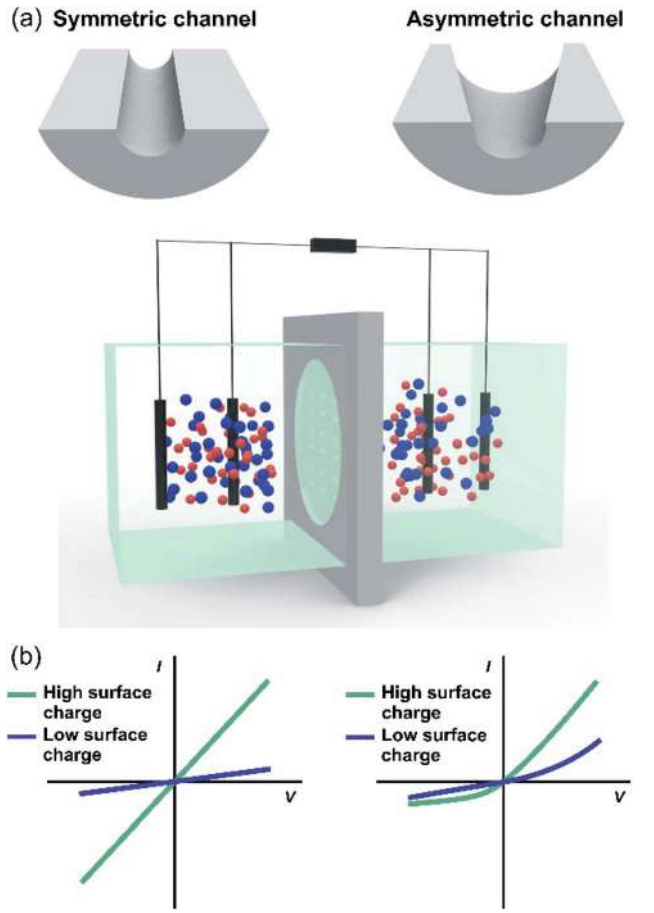

Fig. 6 (a) Schematic illustration of an experimental set-up with a four-electrode arrangement routinely used in ion transport routine experiments. The membrane can contain either symmetric or asymmetric channels. (b) Left – characteristic linear *I*–*V* curve for a membrane with symmetric nanochannels. Under a surface-charge-governed regime, the response is strongly dependent on the surface charge. High concentration of surface charges leads to high conductance (steep slope). Right – characteristic *I*–*V* curve with a rectifying behavior for a membrane containing asymmetric nanochannels. Under a surface-charge-governed regime, the response is strongly influenced by the surface charge. Higher surface charge leads to higher rectification efficiency (ratio between *I* (high conductance branch) and *I* (low conductance branch)).

5.1 Multi-channel membranes – 1D membranes

5.1.1 Ion-track-etching technology. Taking advantage of the damage caused by high-energy ion beams, it is possible to produce solid-state nanochannels in polymer membranes (*e.g.*, polyimide – PI-, polycarbonate – PC-, polyethylene terephthalate – PET-, *etc.*) in a two-step procedure called the ion-track-etching technique (Fig. 7(a)(i)).[72,136–139] Towards this aim, in a first step, a polymeric membrane with a thickness in the micrometric range is irradiated with swift heavy ions (kinetic energy $\sim$ MeV to GeV) generating a cylindrical damaged region of several nanometers in diameter along the ion path called the ion-track.

Also, the final number of tracks per area unit can be adjusted during irradiation from a single ion up to 10^{12}–10^{13} ions per cm^2 (ion fluence) (Fig. 7(a)(ii)).[140] This fact has important technological relevance since it makes possible the accurate control of the final channel number in a certain membrane area (pore density).

After irradiation, in a second step, each ion-track is transformed into a nanochannel by a selective chemical etching procedure.[69,141] The selectivity of the track etching process is based on the radiation damage with pronounced changes in the chemical and physical properties compared to the non-irradiated bulk material. For track etching, the irradiated materials, such as PC or PET, are typically exposed to aqueous NaOH solutions whereas PI foils require NaOCl solutions with active Cl.[142] The geometry and size of the final channels is controlled by choosing suitable etching conditions, *e.g.* increasing the time of etching results in larger channels or adding a surfactant to the etchant modifies the opening geometry of the nanochannels (Fig. 7(a)(iii)–(v)).[34,36,143–148] For nanosized channels, the channel shape (cylindrical or conical) has a strong influence on the *I*–*V* curve, *e.g.* leading to a diode-like behavior. The geometry control thus has a significant effect on the performance of SGE devices based on track-etched nanochannels.

5.1.2 Anodic oxidation method. Until now, several methods have been reported for the generation of alumina membranes containing nanochannels.[149–151] Most of them are based on the two-step electrochemical anodization (oxidation) of aluminum in acidic electrolytes (Fig. 7(b)).[152] In a first step, a clean aluminum sheet is anodically oxidized in an acidic electrolyte (*e.g.* oxalic acid, sulfuric acid, phosphoric acid, *etc.*) to form an alumina layer onto the metallic membrane. Then, the preformed alumina is removed by a chemical treatment with phosphor-chromic acid giving rise to a textured concave

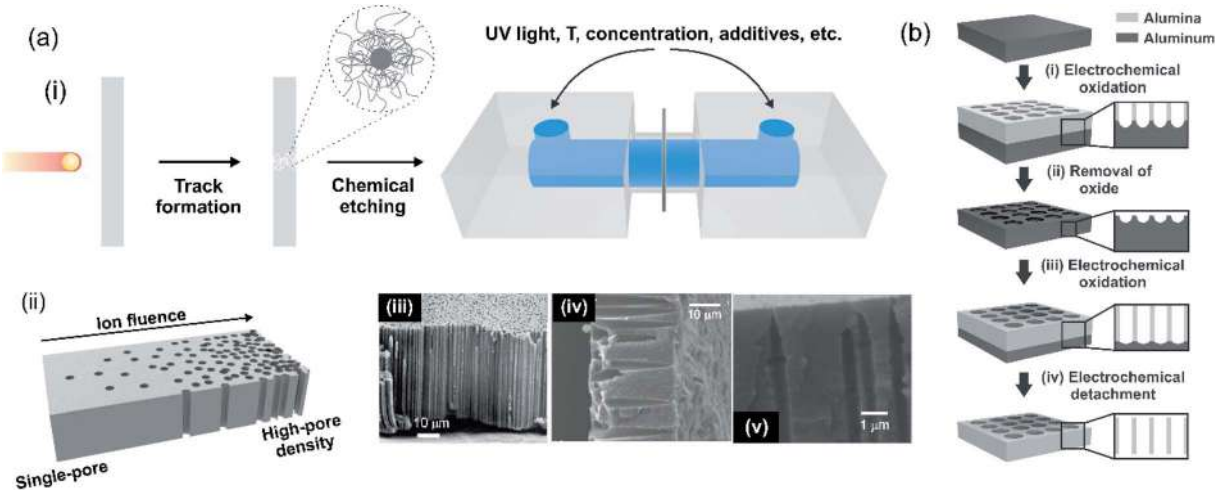

Fig. 7 (a) (i) Scheme of ion-track-etching nanofabrication technique. (ii) Scheme illustrating the possibility of obtaining membranes with different pore densities by tuning the ion fluence. Scanning electron microscopy images of different membrane cross-sections containing channels with different geometries: (iii) cylindrical in polyimide (PI); (iv) conical in polycarbonate (PC) and (v) bullet in polyethylene terephthalate (PET). (b) Schematic illustration of the different steps involved in the fabrication of anodic aluminum oxide (AAO) membranes containing nanochannels by electrochemical anodization. Figure (a)(i) adapted with permissions from ref. 140. Copyright © 2012, Toimil-Molares. Figure (b) adapted with permissions from ref. 152. Copyright © 2004 American Chemical Society. Figure (a) (iii) was adapted with permissions from ref. 142. Copyright © 1996 Published by Elsevier B.V. Figure (a) (iv) was adapted with permissions from ref. 38. Copyright © 2018 WILEY-VCH Verlag GmbH & Co. KGaA, Weinheim. Figure (a) (v) was adapted with permissions from ref. 63. Copyright © 2020 Published by Elsevier B.V.

pattern on the aluminum substrate. Subsequently, the aluminum substrate is exposed to a second anodic oxidation step in some acidic electrolyte to form highly ordered pores in the alumina. Finally, the aluminum barrier is detached by applying a voltage pulse (or chemical etching) and concomitantly, a free-standing anodic aluminum oxide (AAO) membrane with well-ordered pores is obtained. These methods allow the creation of pores in a honeycomb-like array in the diameter range of 5 to 250 nm and pore density $\sim 10^{11}$ pores per cm^2.[151,153] Nevertheless, it is worth mentioning that in these systems, the pore density is linked to the pore diameter due to the hexagonal package and, therefore, it is difficult to vary both parameters independently. Porous alumina membranes containing ordered nanochannels are commercially available in a wide variety of dimensions.

5.2 Single nanopores on 2D materials

5.2.1 Focused ion beam. In focused ion beam techniques, low energy focused ion beam, typically Ga ions with energies in the range of keV, impinges the surface and removes the material until a nanopore is formed.[154–158] This process is based on sputtering, which removes atoms due to collisions of the projectile with surface atoms. One of the major drawbacks of this technique is the fact that each pore has to be drilled individually and the membrane material needs to be ultra-thin (~100 nm), and have a low roughness. This technique has mainly been applied to produce nanopores in materials such as SiN or SiC. It was also demonstrated that these ultrathin membranes with pores can be used as support for other nanostructures such as boron nitride nanotubes or MoS_2 nanopores.[46,159] Considering the difficulty in obtaining up-scaled membranes, this method is often confined to single-pore systems, and therefore, its utilization in the creation of nanoporous membranes for energy conversion is limited. Nevertheless, single-pore membranes created by focused ion beam techniques have been useful for the analysis of the influence of different experimental variables related, *e.g.* the pore size.

5.2.2 Electron beam (e-beam). A focused electron beam can also be used to produce solid-state nanopores. In this technique, the sample is irradiated with the high-energy electron beam of a transmission electron microscope (TEM) which causes sputtering and drills a hole in the material.[160–165] Similar to the focused ion beam technique, this nanofabrication technology is mostly confined to the creation of single-pore systems in ultrathin membranes.

5.3 2D laminar and ultrathin nanoporous membranes

The balance between ion selectivity and high conductance gave rise to 2D laminar and ultrathin membranes, which are a desirable feature for the development of the SGE platforms.[57] 2D laminar nanoporous membranes are typically obtained by stacking nanosheets, thus creating interstitial interlayer spaces that work as nanofluidic channels.[61] Until now, 2D laminar nanoporous membranes have been created using various materials, such as carbides, nitrides,[166] carbonitrides of early transition metals (MXene),[167] graphene,[123,168,169] black-phosphorus (phosphorene),[170] boron nitride nanosheets,[124] and kaolinite,[171] among others.[172]

There are at least two common methods for the creation of 2D laminar membranes: (a) vacuum filtration and (b) layer-by-layer (LbL) assembly. Membranes based on MXene, graphene, black phosphorus, and reconstructed kaolinite are usually obtained by vacuum filtration of a stable colloidal dispersion of the material that produces the assembly of the membrane (Fig. 8(a)).[123,170,173] Subsequently, the material needs to be

detached to form the free-standing membrane. In some cases, the preparation of the material dispersion requires some pretreatments. For instance, in the case of MXene, the starting solid often contains an Al layer in the phase. This is why a selective chemical etching (*e.g.* with HF) is required beforehand to replace the A-group layer from the $M_{n+1}AX_n$ phase with other terminal groups such as –OH, –O, or –F.[174–177] In the case of graphene, the dispersion can be obtained either commercially or by exfoliation of graphite applying different protocols (modified Hummers' method).[178]

The layer-by-layer method is attractive for the creation of composite 2D nanoporous membranes (Fig. 8(b)).[179] For each component of the composite membrane a dispersion is prepared and then, a substrate (*e.g.* a glass slide) is alternately immersed in each dispersion. The assembly of the material onto the substrate surface during immersion is achieved by exploiting different intermolecular interactions such as electrostatic interaction or van der Waals forces. The thickness of the composite membrane is adjusted by the number of immersion cycles. After a given number of immersion cycles, the material is dried and the free-standing membrane is peeled off from the substrate.

5.4 3D nanoporous membranes

3D membranes consist of micrometric networks with interconnected pores, as in the case of hydrogel-based membranes. The generation of 3D nanoporous membranes is accomplished with a wide variety of reactions depending on the chemical nature of the network such as sulphonation reactions, non-solvent induced phase separation, photoinduced polymerizations of different precursor solutions, chemical oxidations (*e.g.* using 2,2,6,6-tetramethylpiperidine-1-oxyl radical as the catalyst), generation of agarose hydrogels, just to name a few.[64,180–184] Conventionally, this kind of membranes can not only be created with a wide variety of thickness (in the micrometric range), pore sizes, and distribution but also can be used as a building block for the development of different asymmetric structures through its combination with other nanofluidic platforms such as AAO or track-etched foils. Also, in contrast with the previous systems, 3D nanoporous membranes containing interconnected nanopores enable the ion flow in various directions which promotes a decrease in the resistance.[64] These concepts will be addressed in more detail in Section 7.2.

6 Enhanced nanofluidic osmotic energy – the impact of structural and experimental variables on SGE performance

Recently, researchers have dedicated great efforts to determine the principal parameters that define the performance of SGE generators. Understanding the influence of the different structural and experimental variables on the energy conversion performance of nanofluidic-based platforms is crucial on the way to technological readiness. This section presents and discusses the effect of parameters such as nanochannel geometry (diameter, shape, length), pore density, and surface charge density, and experimental variables such as pH, concentration gradient, electrolyte nature, and temperature on the nanoporous membrane energy-conversion capability. Since many of these variables are often interconnected, the experimental situation is rather complex. Here we use a simplified scenario to provide guidelines for the creation and study of SGE platforms based on nanofluidic devices.

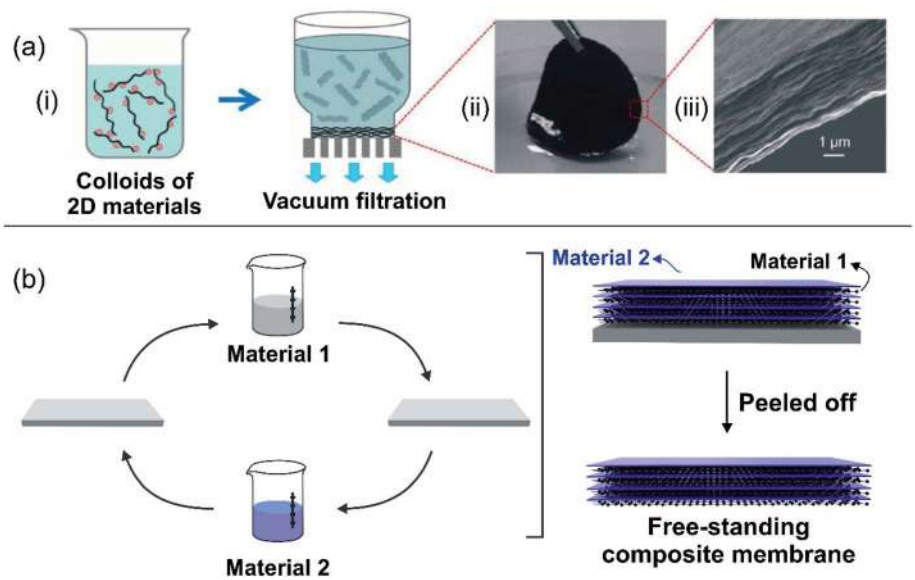

Fig. 8 (a) Schematic illustration of a 2D-laminar membrane created by vacuum filtration. (ii) Picture and (iii) scanning electron microscopy image of graphene oxide membrane. (b) Schematic illustration of 2D-laminar membranes created by layer-by-layer assembly. Figure (a) adapted with permission from ref. 43. Copyright 2017 WILEY-VCH Verlag GmbH & Co. KGaA, Weinheim.

6.1 Channel diameter

Nanochannel diameter is one of the most critical parameters and it has been the subject of study in several research papers. As an example, Tseng *et al.* theoretically studied the influence of diameter in a single cylindrical channel *via* Poisson–Nernst–Planck model simulations.[126] Their results showed a remarkable effect of the channel dimension both on E_m and I_{osm}. Conventionally, a lower channel dimension results in a better ionic selectivity due to the EDL overlapping that leads to a maximization of E_m. Also, a small channel enables working with a high concentration gradient keeping the ion selectivity, which yields high η_{max} values. However, the diminution of the channel diameter generates a decrease of I_{osm} (per channel) and therefore, a reduction of the power.[63] This fact can be attributed to the decrease in the ion flux per channel caused by the critical decrease in the inner space.[45,63]

Power maximization is a trade-off situation in which it is necessary to maximize ion selectivity and effective gradient but without compromising the I_{osm} values. Experimentally, this fact was evidenced by Feng *et al.* in their work focused on the NRED performance of a nanopore in a single-layer MoS_2.[45] When the pore size was lower than 10 nm, the pore displayed best E_m values but it negatively impacted on I_{osm}. On the other hand, when the pore size was slightly higher than 10 nm, the pore displayed a high I_{osm} but with a decrease of E_m. Finally, the estimated maximum output power density was 10^6 W m^{-2} for a pore diameter of 10 nm. A similar trend was also evidenced in bullet-shaped single nanochannels (Fig. 9(b)).[63]

In contrast to this behavior seen in single-pore membranes, the results obtained in multi-channel systems show that smaller pores can be a key to minimizing the detrimental effects of concentration polarization and thus, maximizing the output power in up-scaled membranes. This effect will be addressed in more detail in the following sections.[182,185]

Although pore diameters comparable to λ_D could be thought of as a limiting constraint, some authors have reported interesting counter-examples.[119,186] Siria *et al.* reported the development of a single boron nitride nanotube with an inner radius of 40 nm that achieved an extracted power density of 4 kW m^{-2}.[46] The authors claim that the current generated by a diffusio-

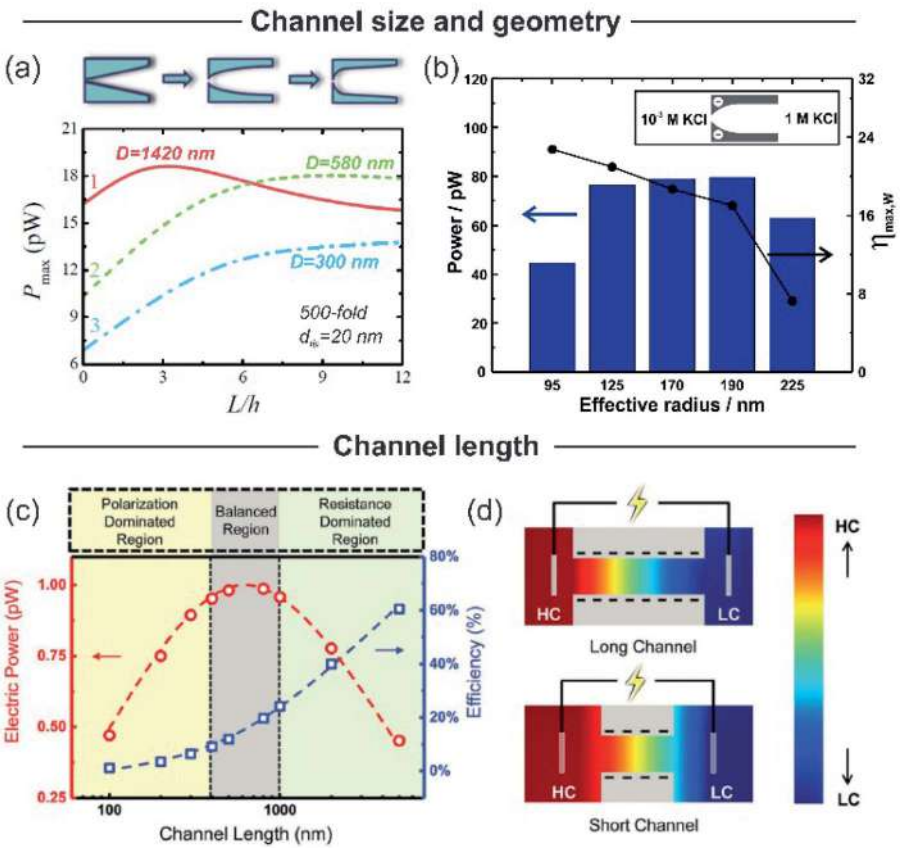

Fig. 9 (a) Dependence of calculated output power with the channel curvature for channels with a tip diameter of 20 nm and variable base diameters (*D*). Reproduced with permission.[128] Copyright 2018, Elsevier Ltd. All rights reserved. (b) Dependence of output power and maximum efficiency ($\eta_{max,w}$) on the effective channel size for bullet-shaped polyethylene terephthalate nanochannels at pH 10 and a 1000-fold gradient. Reproduced with permission.[63] Copyright, 2020 Elsevier Ltd. All rights reserved. (c) Dependence of the calculated electrical output power and efficiency on the channel length for a cylindrical channel with a diameter of 10 nm and a surface charge of −0.06 C m^{-2} and applying a 3000-fold concentration gradient. (d) Ion concentration distribution for two channels with different lengths. The ion concentration polarization effect is higher for shorter channels. HC and LC refer to high and low concentrations respectively. Reproduced with permission.[193] Copyright 2017, WILEY-VCH Verlag GmbH & Co. KGaA, Weinheim.

osmotic process has its origin in the osmotic pressure gradient in the interfacial diffusion layer due to the difference in salt concentration. They provide this reason why high performance was obtained with a nanotube appreciably larger than EDL.

6.2 Geometrical asymmetry

To overcome the trade-off between the size and the SGE parameters, membranes with channels of asymmetric geometry have been proposed. The membranes are typically 10–20 μm thick and have nanochannels with a small aperture (tip) of a few nanometers in diameter, whereas the other aperture has a diameter in the micrometer range (>100 nm). By employing this strategy, it is possible to decrease the channel resistance without considerably affecting ion selectivity.[41,103,187,188] Furthermore, the disruption of the symmetry usually promotes the generation of devices with diode-like behavior which is advantageous since this non-ohmic behavior can suppress the back current and thus boost the output power by reducing the Joule heating loss.[11,41,135] Within asymmetric geometry, the most studied systems contain bullet-shaped and conical nanochannels. Hsu *et al.* compared the performance of a channel with the same length, tip, and base diameter but different shapes using PNP simulations.[128] The authors found that if the base diameter of the channel is not excessively large (<1400 nm), the bullet-shaped geometry achieved the best power values because its higher inner space leads to a significant enlargement of I_{osm} (Fig. 9(a)). In contrast, the trumpet geometry results in the lowest power value due to its low inner space, which yields the lowest I_{osm} values. According to the simulations, the efficiency (or selectivity) of the trumpet geometry yields best results whereas the bullet shape displays the worst values and the conical geometry has intermediate efficiency. In this regard, Laucirica *et al.* reported for the first time an experimental analysis on the performance of a PET membrane with a single bullet-shaped nanochannel as the SGE device (Fig. 9(b)).[63] In a similar way to that observed in cylindrical channels, the channel size and the power obtained denoted a trade-off situation. On the one hand, the increment of tip and base diameter enabled higher I_{osm} values (if the ion selectivity was maintained) but produced a decrease of E_m. Beyond this trend, the device with an optimized size displayed a high output power of 80 pW per channel by combining appropriate experimental conditions with this bullet-shaped geometry which exceeded the reported values in conical nanochannels of similar dimensions.[51]

6.3 Channel length

The decrease of the channel length is considered to produce an increment in I_{osm} (R_c diminution) with a loss of selectivity (E_m diminution), setting another trade-off situation.[126,127,189–192] To shed light on this problem, Cao *et al.* conducted a comprehensive analysis of the impact of the channel length on the energy-conversion performance.[193] Employing PNP simulations, the authors found that the trade-off between the increment of I_{osm} and the decrease of E_m resulted in an enhancement of the output power at low and moderate concentration gradient (<300-fold) as the channel length decreases. However, when the SGE experiment was carried out at high concentration gradients (>300-fold) an anomalous dependence between the output power and the channel length was evidenced (Fig. 9(c)). Increasing the concentration gradient causes a severe ion concentration polarization (ICP) in short nanochannels (<400 nm) that gives rise to a diminution in the effective concentration gradient. Thus, the real difference of transmembrane concentration (effective concentration gradient) is lower than the bulk concentration differences at each side (concentration gradient) (Fig. 9(d)). This fact induces a decrease in both E_m and I_{osm}. Concomitantly, in discrepancy with the intuitive viewpoint, if the concentration gradient was higher than 300-fold, an excessive decrease in the channel length led to a drastic drop in the maximum power. Considering this scenario, the authors claim that a length in the range of 400–1000 nm is the best option when the concentration gradient is around 3000-fold. For channel lengths lower than 400 nm the behavior is controlled by ICP (polarization-dominated region) whereas for channel lengths larger than 1000 nm, the power decreases due to the high R_c values (resistance-dominated region) (Fig. 9(c)). This behavior was experimentally observed by Su *et al.* in AAO membranes.[194] By varying the time of the second anodization step during the AAO membrane synthesis, the authors created membranes with a wide range of channel lengths for SGE studies. In agreement with the PNP simulations, they found that a significant decrease in the channel length led to a detriment in the osmotic power due to the ICP-induced decline in the effective concentration gradient. On the other hand, a significant increase in channel length led to lower osmotic power values due to the higher membrane resistance. According to the simulations, the relationship between P_{max} and the channel length has a maximum value when the thickness of the membrane was about 8 μm. Additionally, these authors demonstrated that this trend is independent of the surface charge value and polarity.

6.4 Pore-density

Beyond the studies on single-pore membranes with accurate control of the different structural parameters, to create SGE devices with potential technological applications, the scale-up to high-pore density membranes is a major challenge. Although initial experimental studies estimated the multi-channel device potential considering it a linear dependence of the single-pore power, several recent theoretical[129,130,195] and experimental studies[180] have reported important deviations from linearity. Yazda *et al.* reported a comprehensive experimental study about this topic by analyzing the energy conversion performance of a 2D composite membrane formed by silicon nitride and boron nitride (Fig. 10).[196] Taking advantage of a novel nanopore fabrication technique called tip-controlled local breakdown, they were able to create membranes with different pore-to-pore spacing and subsequently, to evaluate the energy capabilities under the different conditions (Fig. 10(a)). The analysis of the results shows that the diminution in the interpore distance to values lower than ~500 nm yields an abrupt drop in both the E_m and I_{osm} which was ascribed to

a probable interplay between the Dukhin length and concentration polarization (Fig. 10(b) and (c)). Therefore, in order to minimize the pore–pore interaction and maximize the power density, the authors found a value of 500 nm as the optimum pore-to-pore spacing (Fig. 10(d)). Wei Guo and coworkers thoroughly investigated the reasons behind the anomalous behavior

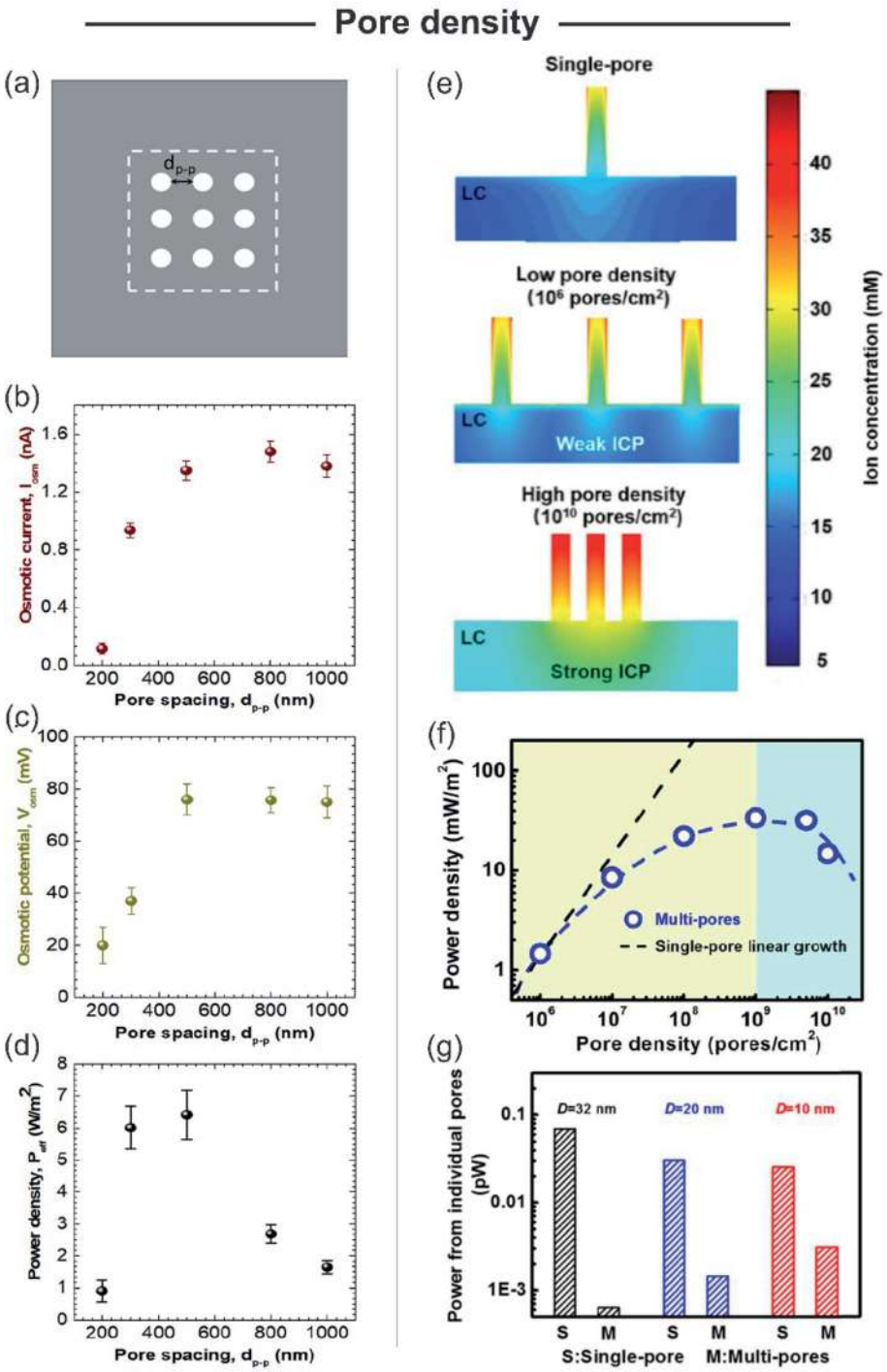

Fig. 10 (a) Scheme illustrating the system employed for studying the effect of pore spacing (d_{p-p}). The dashed box represents the working area used for maximum power density calculation. (b) Osmotic current (I_{osm}), (c) osmotic potential (or membrane potential, E_m) and (d) maximum power density in terms of the pore spacing. Adapted with permission.[196] Copyright 2021, American Chemical Society. (e) High-pore density membranes lead to strong ion concentration polarization (ICP). (LC refers to the low concentration reservoir). (f) Non-linear relationship between pore-density and output power. Power density *vs.* pore density curve was obtained by modeling cylindrical channels with length 60 nm, diameter 32 nm, surface charge density −0.06 C m^{-2}, and a 10-fold gradient. (g) Power from individual pores for different single-pore (S) and multi-channel (M) systems containing channels with different diameters (*D*). Reproduced with permission.[106] Copyright 2018, SIOC, CAS, Shanghai, & WILEY-VCH Verlag GmbH & Co. KGaA, Weinheim.

in multi-channel membranes in comparison to the extrapolated single-pore systems by PNP simulations (Fig. 10(e)).[106,197] They found that the power output achieved by a multi-channel system with pore densities lower than 10^6 pores per cm^2 could be appropriately estimated through the linear dependence of the single-pore results. However, for pore densities higher than 10^6 pores cm^{-2} the pore–pore distance is drastically diminished and the pore–pore interaction cannot be neglected. In these cases, the high pore densities induce a strong ICP near the membrane in the low-concentration reservoir that produces an increment of the entering resistance and, concomitantly, hindered the osmotic energy capabilities (Fig. 10(e)). This rationalizes why the power values strongly deviate from the value obtained by linear estimation from single-pore systems (Fig. 10(f)).[46,198] In addition, several studies have shown that the ICP effect in multi-channel systems is lower as the channel diameter decreases due to the diminution in the ion flux per pore for smaller channels and the concomitant mitigation in the ICP (Fig. 10(g)).[106,182,185] For this reason, the use of smaller nanochannels can be crucial for the development of up-scaled membranes. Furthermore, as described in the following sections, the use of heterogeneous membranes has been widely employed as an approach to reduce the mechanisms that vanish the output power harvested in membranes with high pore density. Despite the considerable advances in the last few years, the mitigation of the effects arising from pore–pore interaction in high-pore density membranes remains a major challenge in this area (see Section 8.1).

6.5 Surface charge density and location

The modulation of surface charge density is one of the most widely used strategies to experimentally improve the SGE conversion performance. There are at least two common approaches for adjusting the surface charge: (a) the control of experimental conditions such as pH or light; and (b) the attachment of different charged building blocks onto the channel surface.

(a) Surface charge modulated by pH or light. The pristine nanochannels/nanopores created in different materials such as MoS_2, silica, AAO, or polymers (PET, PI, or PC) have a pH-dependent surface charge density. Usually, an increment in the surface charge density is assumed to increase both E_m and I_{osm}. Hence, setting the pH under any condition that provides a high charged density on the surface is a simple option to enhance the performance of the SGE device.[51,63,198] Nevertheless, recently Hsu *et al.* showed an anomalous dependence between the surface charge density and the output power.[199] These authors conducted a comprehensive experimental study on the impact of pH (surface charge density) on the osmotic output power using a funnel-shaped single nanochannel in PET. The surface charge density of the channel grew with increasing pH, but the osmotic power diminished abruptly above pH = 10. The authors attributed this anomalous behavior to the increment in the ICP effect due to the massive rise in the surface charge density when the pH value exceeded 10. In more detail, the high surface charge density combined with the small tip size (diameter of 15 nm) generates a strong EDL overlap that causes an increment in the ion concentrations at both sides of the membrane (ICP effect). This fact leads to a decline in the effective transmembrane gradient (effective chemical potential difference) and, concomitantly, in the output power.[200] Therefore, while a highly charged state of the surface is a primordial requirement to achieve ionic selectivity and, usually a good performance, the excessive increment of the surface charge can induce a negative impact, mainly in highly confined nanofluidic devices.[201]

In a different approach, some materials offer the opportunity to modulate the surface charge density *via* a non-invasive stimulus, such as light. For instance, Graf *et al.* demonstrated an increase in the energy-conversion properties of MoS_2 nanopores *via* light irradiation.[201] This fact was ascribed to the light-induced increment in the surface charge of the pores. Similar strategies have been reported in 2D MXene membranes and TiO_2/C_3N_4 heterojunction nanotubes.[202,203] These examples illustrate the possibility to combine solar energy and SGE with a relatively simple strategy.

(b) Surface charge modulated by building block immobilization. Another common approach to tune the surface charge density is based on the immobilization of different molecular systems with charged groups.[204–206] As an example, Laucirica *et al.* reported the development of an SGE device by the asymmetrical modification of a single PET bullet-shaped nanochannel with a polyaniline (PANI) film.[114] Amino and imino groups of PANI are partially charged at low pH which enabled the utilization of this platform as an energy conversion system operative under almost unexplored acidic pH conditions. The surface charge inversion due to the integration of PANI film was evidenced by the sign inversion of E_m when *I–V* curves were recorded applying a concentration gradient. By applying a 1000-fold gradient of KCl at acidic pH, PANI film promoted an increment of 100% of output power (~15 pW) compared to the unmodified channel. Recently, Lin *et al.* introduced a novel development of a high-performance SGE device by functionalizing a conical channel with poly-L-lysine.[186] Notably, the channel contained both aperture diameters above 400 nm. Although this magnitude widely exceeded the Debye length (at $C_{KCl} = 1$ mM $\lambda_D = 9.6$ nm), the system presented ion selectivity and remarkable performance as an osmotic power nanogenerator given by a $P_{max} = 120$ pW (per pore) applying a 500-fold gradient. This peculiar behavior was attributed to the high positive charge provided by poly-L-lysine chains. In this regard, a recent study showed analytically that the ionic selectivity in these cases is further explained in terms of the Dukhin number rather than the EDL overlap (see Section 3.1).[75]

Beyond the importance of surface charge magnitude and sign, the location of charges also acquires a crucial role. For instance, a recent study showed that the immobilization of a polyelectrolyte layer not only on the walls of the channels but also on the outer walls of the membrane represents a simple approach to enhance the power output.[188,207] On the other hand, the creation of systems with a distribution of net charges within the entire volume of the nanochannel interior (space charge) rather than just on the nanochannel walls (surface charge) has

demonstrated to be a simple way to improve the SGE performance.[65,118,208]

In the last few years, asymmetric modifications producing heterogeneous membranes composed of two different monolayer porous membranes have been used as an essential strategy to boost the power in NRED systems.[209,210] In 2019, Wei Guo and coworkers carried out a PNP-based study on the fundamental aspects of heterogeneous membranes as osmotic nanogenerators.[211] In contrast to homogeneously charged nanofluidic devices, they demonstrated that the existence of a heterojunction suppresses the ICP phenomenon without compromising the ion selectivity. The effective concentration gradient does not vanish, and therefore, the I_{osm} and the extracted power increase. The analysis also includes the influence of the structural parameters of the heterogeneous region such as diameter and length. By employing a heterogeneous region with a small pore diameter (<20 nm), the ICP effect is overcome but a drastic reduction in the overall ion selectivity was also observed. These results suggest that it is indeed possible to boost the power exhibited by introducing a heterojunction region and to obtain an optimal balance between ICP suppression and high ion selectivity. For this, the optimization of the length and diameter of the heterogeneous region plays a crucial role. On the other hand, the disruption of the symmetry by introducing an asymmetric modification enables obtaining devices with diode-like behavior. This characteristic positively impacts the osmotic energy performance (see Section 6.2).[11]

6.6 Concentration gradient

Concentration gradient is one of the experimental variables that more critically impact the SGE generation. Typically, an increment in the concentration gradient causes a boost in the output maximum power since it generates a rise in both the I_{osm} and E_m (Fig. 11(a)).[45,51,63,114] However, in some cases, this relationship is not completely fulfilled and an excessive increment in the difference of transmembrane concentration can be counterproductive in the power exhibited. For a fixed diameter and pore-density, the concentration gradient has strong effects on the obtained power. On the one hand, the increment of the concentration gradient directly increases the power as it produces a richer free energy source from a thermodynamic point of view (eqn (20)). However, a high concentration gradient requires that one side of the membrane is exposed to a high electrolyte concentration, which concomitantly produces a loss of ion selectivity due to the efficient screening of surface charges (see the relationship between Debye length and salt concentration in eqn (2)).[102,117,126,212] Considering eqn (20), this fact produces a decline in E_m due to the diminution of counter-ion transference number. On the other hand, if the electrolyte concentration in the diluted reservoir is excessively low, a similar detriment in the output power can occur due to the diminution of t_+, but in this case, this effect is attributed to the diminution in the surface charge caused by the regulation charge effect at low electrolyte concentration.[190,213,214]

For asymmetric channels, also the directionality of the gradient is important; *i.e.* at which side of the nanoporous membrane the highly concentrated and diluted solutions are placed (Fig. 11(b)).[50,215,216] Supported by PNP simulations in geometrically asymmetric nanochannels, different authors showed a better energy-conversion performance when the diffusion flux was established from base-to-tip instead of tip-to-base which means that, to achieve the best output power and efficiency, placing the concentrated solution in the base side and the diluted solution in the tip side is convenient.[51,103,105] The reason behind this behavior is ascribed to the increase (decrease) of the selectivity when the tip side was exposed to the diluted (concentrated) solution since the ion-selective mechanism in asymmetric channels stems from the tip region.[217] However, when the asymmetry is provided by targeted surface modification, instead, anticipating which will be the best arrangement is more difficult. In these experiments, the system is usually tested in both configurations (Fig. 11(b)).[64,218,219]

6.7 Electrolyte nature

In addition to the concentration (*i.e.* activity) gradient, Cao *et al.* performed a comprehensive analysis of how the electrolyte nature impacts the performance of an SGE device based on a single conical PI nanochannel.[220] Combining experimental

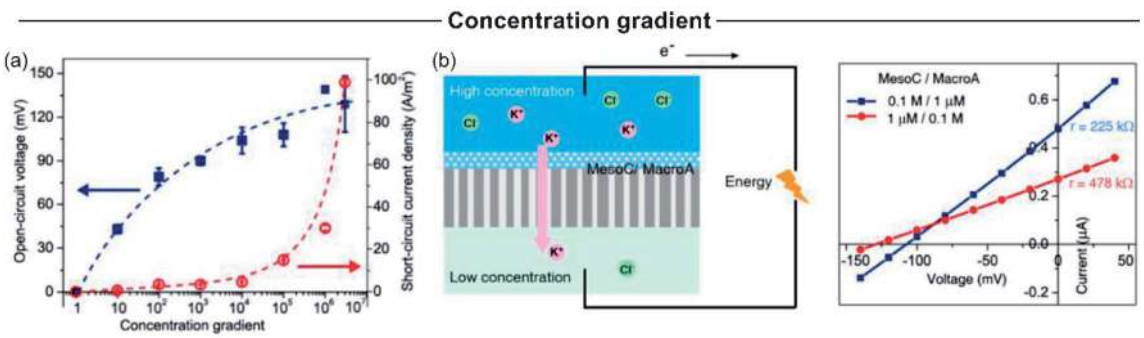

Fig. 11 (a) Influence of concentration gradient magnitude on the open-circuit voltage and osmotic current. (b) Influence of concentration gradient directionality on the produced osmotic power by asymmetrically modified membranes. Reproduced with permission.[219] Copyright 2014, American Chemical Society.

results with PNP simulations, the authors showed that the net diffusion current (I_{osm}) is dominated not only by the ion-selectivity of the nanoporous membrane which favored the counter-ion flux but also by the inherent different diffusive properties of counter-ions compared with the co-ions of a given compound. To boost output power and efficiency, these two mechanisms must act synergistically.[213]

Thus, the power in a cation-selective nanochannel can be increased by selecting KF instead of LiCl as the higher inherent diffusion of K^+ in comparison to F^- ($D_{K^+} > D_{F^-}$) and the cation flux favored due to the cation-selective membrane would have a collaborative effect. For the case of an anion-selective membrane, the use of LiCl instead of KF is recommended since the higher inherent diffusion of Cl^- in comparison to Li^+ ($D_{Cl^-} > D_{Li^+}$) and the anion flux favored due to the anion-selective nanoporous membrane would work synergistically.

In the case of sub-nanopore membranes, both size and diffusivity of hydrated and dehydrated ion sizes need to be considered.[221–223] For example, for nanoporous membranes based on metal–organic frameworks (MOF) with pore sizes around 6–7 Å it was shown that counter-ions with a size lower than the pore size of the MOF are able to pass through the MOF porosity yielding higher ion fluxes and selectivity.[224] Consistently, the transport across the porous MOF in the case of counter-ions with larger hydrated sizes is more restricted which leads to a detriment in the power capabilities. Quantitative results of different upscaled MOF-based membranes will be addressed in more detail in Section 7.2.

6.8 Temperature

Temperature is a relevant factor in the NRED performance since it directly affects the ion diffusion coefficients. In principle, the NRED experiment can be carried out both under isothermal and asymmetrical temperature conditions (*i.e.* the solution temperature at each side of the membrane being different). Until now, most experiments have been performed under isothermal conditions, where usually the P_{max} is enhanced as the reservoir temperature increases due to the maximization of both I_{osm} and E_m (see dependence of E_m on T in eqn (20)).[126,225,226]

$$E_m = (2t_+ - 1)\frac{RT}{F}\ln\left(\frac{a_H}{a_L}\right) \quad (43)$$

Otherwise, the η_{max} is practically not modified as both diffusion coefficients (counter-ion and co-ion) are modified similarly and, therefore, the transport numbers remain almost unchanged.[126,225] However, other temperature effects rather than that directly expressed in eqn (20) could arise. For some materials, temperature-induced changes in the surface charge which also cause variation in η_{max} have been reported.[175,227,228] As an example, on silica surfaces, an excessive increase in the temperature can result in a drastic diminution in E_m and power explained by a reduction in the effective surface charge density owing to the formation of hydrophobic patches that mask the mesoporous surface.[227]

An asymmetric temperature configuration in NRED was addressed in detail by Liu and coworkers in their studies based on numerical simulations in cylindrical nanochannels.[225,229] The effect of the temperature gradient was evaluated as a function of the temperature difference and the gradient direction, denoted as positive temperature difference (PTD) when the low-temperature reservoir coincides with the low concentration reservoir and as negative temperature difference (NTD) when the low-temperature reservoir coincides with the high concentration reservoir (Fig. 12(a)). The authors found that both NTD and PTD

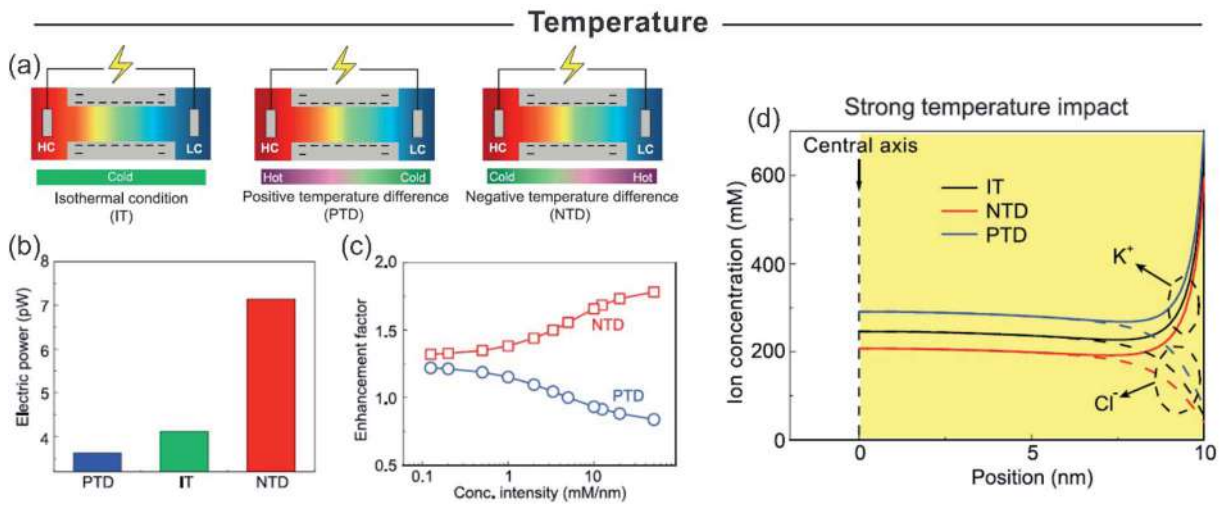

Fig. 12 (a) Different experimental configurations for temperature-dependent experiments of energy conversion. HC and LC refer to high and low concentration reservoirs respectively. (b) Electrical power displayed applying a 1000-fold concentration gradient at different temperature configurations. (c) Influence of the asymmetric temperature directionality on the power ratio compared with the isothermal condition (enhancement factor) in a cylindrical nanopore of diameter 20 nm, length 50 nm, surface charge density −0.05 C m^{-2}. (d) Ion concentration profiles for different temperature configurations. A negative temperature gradient (NTD) leads to a diminution of the ion concentration polarization. Reproduced from ref. 229 with permission. Copyright © 2019, Oxford University Press.

enable an increment in I_{osm} compared to the isothermal condition (considering the low temperature of the asymmetric experiment) since the electrical resistance depends on the average salt temperature. Nevertheless, while the NTD caused an increment in the selectivity and therefore, in E_m, the PTD produced a detriment in this parameter. This fact produced a boost in the extracted power for the NTD configuration but, in contrast, a trade-off situation for the PTD (Fig. 12(b) and (c)). The authors argued that in the NTD situation the diffusion coefficients are enhanced along the osmotic–diffusion direction owing to the temperature impact and thus, the ion concentration inside of the channel is diminished and the selectivity maximized. Also, in the NTD case, the concentration in the channel exit in the low concentration reservoir is diminished due to the effect of the temperature on the diffusion coefficients which suppresses the ICP effect enabling the best P_{max} (Fig. 12(d)) to be obtained. Considering these results, this configuration can acquire special relevance for avoiding the ICP promoted by the pore–pore interaction in multi-channel membranes.[230]

These results suggest that an increment in the osmotic energy can be achieved by simultaneously combining temperature and concentration gradients. Thus, the thermo-osmotic energy conversion obtained from the utilization of natural water sources (*e.g.* river and seawater) and low-grade heat waste could be a key for expanding the boundaries of NRED and thus, to widely exceed the commercial benchmark.[231] Furthermore, low-grade heat waste can be harnessed for the thermal regeneration of low and concentrated solution giving rise to a type of RED in a closed-loop called RED heat engine.[232]

7 Towards the construction of NRED platforms with technological applications

The fundamental insights for the optimization of an NRED device have been introduced in previous sections, presenting results on either single-pore membranes (or low-pore density) experiments or PNP simulations. Nevertheless, with the purpose of producing real NRED devices, the scaling-up from single-pore to multi-channel is a crucial issue. Unfortunately, this is not a trivial challenge due to the hindered P_{max} caused by the pore–pore interactions (see Section 6.4).[106] Furthermore, the NRED applicability would depend on the properties of the available water sources. As an example, from its conception, the RED system was usually intended to be operated with river water (~0.01 M) and seawater (~0.5 M) which not only establishes a specific gradient magnitude (~50-fold gradient) but also fixes other experimental variables such as the pH and electrolyte nature. In the last few years, the opportunity to use different water sources such as saline industrial waste or brine solutions as salinity gradient power resources has gained impetus due to their benefits in terms of power, environmental impact, and versatility.[26] Also, as we will see, all the results were obtained employing millimeter working areas which is not a realistic condition (see Section 8.1). For the construction of NRED platforms with technological applications, these aspects have to be considered. This section presents strategies reported by different researchers that enable them to tackle the aforementioned challenges. For ease of reading, this section is subdivided into two parts introducing the following systems: (a) two-dimensional (2D) and other ultrathin membranes, and (b) multi-channel and three-dimensional (3D) materials (see Fig. 1).

7.1 2D-materials based and ultrathin membranes for the development of SGE nanodevices

Up-scaled 2D membranes usually involve 2D-laminar membranes. Well-known examples of these materials for developing SGE devices are graphene,[123,168,233] hexagonal boron nitride, carbon nitride,[166] MXene,[167] molybdenum disulfide,[172] among others.[116,171,234] In the case of 2D layered membranes the interstitial spaces among the nanosheets act as "lamellar channels" enabling ion transport. As previously explained, the combination of ultrathin membranes and highly charged "lamellar channels" can be a key in the development of highly efficient membranes for osmotic energy conversion due to their intrinsic high ion selectivity and lower resistance.[113,235] In this section, some of those results obtained in up-scale 2D-based membranes are summarized.

Ji *et al.* created NRED stacks by alternating negatively and positively charged 2D graphene oxide membranes created by flow-induced self-assembly and subsequent thermal stabilization (Fig. 13(a)).[123] Due to the natural negative charge of graphene oxide, in the case of positive 2D membrane construction, the graphene oxide nanosheets were previously functionalized to form positively charged imidazolium groups. The ion selectivity of both membrane types in combination with the low resistance to the ion fluxes provides an output power density of 0.77 W m^{-2} per NRED stack applying a concentration gradient of 50-fold (simulated seawater and river water system) (Fig. 13(b) and (c)). Based on their platform, the authors were able to harvest osmotic energy from different water sources such as acid rain, industrial wastewater, brine, and urine which extends the applicability of this NRED system. Finally, the output voltage of the system reached 2.7 V by stacking 13 membrane pairs. It was demonstrated that this is sufficient to operate different electronic devices such as a calculator and light-emitting diodes (LEDs) (Fig. 13(d)).

One of the most employed strategies to decrease the membrane resistance and increase the ion selectivity is the appropriate functionalization of the membrane. In the case of 2D-layered membranes, the creation of hybrid membranes by assembling different materials has become an attractive option.[236–238] Wu *et al.* reported the construction of a composite membrane formed by graphene oxide and cellulose nanofibers (GO/CNFs).[228] Under optimized conditions and applying a concentration gradient of 50-fold (mimicking seawater/river water), the system exhibited an output power density of 4.19 W m^2 exceeding results obtained with isolated cellulose nanofibers and graphene oxide. This enhancement was ascribed to larger interlayer distances that allow fast ion transport and high transmembrane flux but without losing selectivity due to the space charge introduced by CNFs.

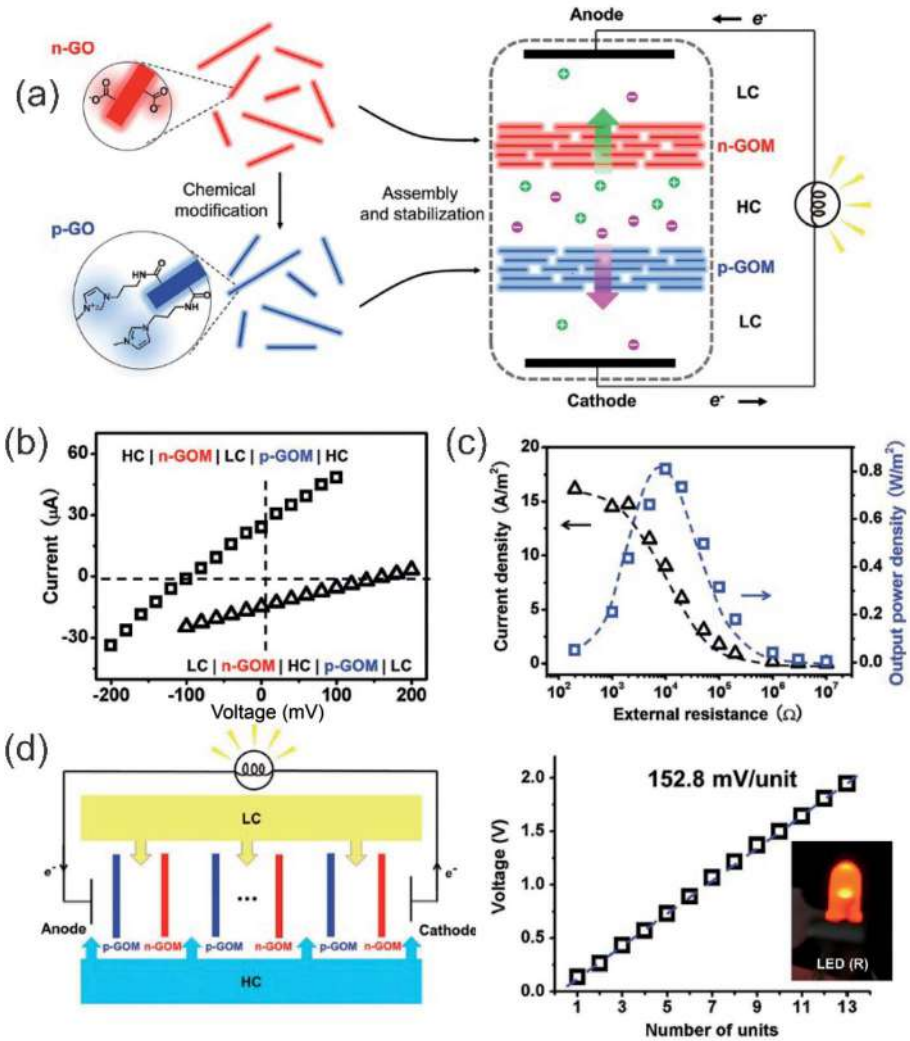

Fig. 13 (a) Scheme of the experimental set-up of nanofluidic reverse electrodialysis stacks based on negative and positive graphene oxide (n-GO and p-GO) membranes. (b) The iontronic output under different directionalities is shown too. HC – high concentration reservoir – denotes an aqueous solution of 0.5 M NaCl and LC – low concentration reservoir – corresponds to an aqueous solution of 0.01 M NaCl. (c) Current density (black) and output power (blue) in terms of external resistance. The curve displayed a maximum at $P \sim 0.8$ W m^{-2}. (d) Schematic cell and dependence of voltage for the different number of nanofluidic reverse electrodialysis stack units (50-fold gradient). Tandem graphene oxide-based nanofluidic reverse electrodialysis systems can power an LED. Reproduced with permission.[123] Copyright 2016, WILEY-VCH Verlag GmbH & Co. KGaA, Weinheim.

Additionally, these authors studied the osmotic energy performance in terms of temperature. When increasing the temperature from 298 to 323 K, the output power was boosted due to the rise of both ion mobility and negative surface charge density. However, above 323 K the output power decreased owing to the formation of so-called nanopancake-like gas layers that shielded the charged zone. A similar temperature-dependence was evidenced in a previous work carried out on silica nanochannels.[227]

More recently, Zhu *et al.* introduced the first up-scaled 2D-membrane based on MoS_2 for energy conversion purposes.[172] The main difficulty in creating large areas of MoS_2 2D-membranes comes from the low strength and stability of the stacked membrane. However, by combining MoS_2 nanosheets with cellulose nanofibers (CNFs), the authors demonstrated a MoS_2 lamellar nanoporous membrane with high conductivity, high ion selectivity, good mechanical strength, and stability in aqueous media. The nanocomposite membrane was created by vacuum filtration of a dispersion containing both components, the CNFs and MoS_2 nanosheets. The energy conversion performance was studied for CNFs/MoS_2 nanoporous membranes containing different amounts of CNFs and MoS_2 phases. The increase in CNF concentration boosted the ion selectivity due to a larger amount of surface charges, but an excessive increment in the amount of this component yielded a detriment in the ion flux because of the physical sterical hindrance. For its part, the employment of MoS_2 in the metallic phase (M-MoS_2) rather than in the semiconducting phase enables enhancement of the ion flux and selectivity due to the high electron density of M-MoS_2. Therefore, by using MoS_2 in

the metallic phase and optimizing the weight content of CNFs to 8%, the system displays $PD_{max} \sim 5.2$ W m^{-2} applying an electrolyte gradient mimicking the natural seawater/river water system. Furthermore, using natural seawater from the China East Sea and river water, a PD_{max} of around 6.7 W m^{-2} was achieved which exceeds the commercial ion-exchange membranes. Notably, the final response was independent of the pH which opens the door for the utilization of different water sources such as ultra-acidic or alkaline wastes.

In the last few years, MXene compounds have emerged as a promising material for the construction of 2D-membranes with applications in nanoosmotic generators.[239] These materials are based on the chemical formula $M_{n+1}X_nT_x$ where M is an early transition metal (*e.g.* Ti, Cr, Mo, *etc.*), X is carbon and/or nitride and *T* is the terminal group (typically –O, –OH, or –F). MXene compounds are usually synthesized by selective etching of the A-group layer in the $M_{n+1}AX_n$ (MAX) phase.[53,240,241] These terminal groups provide the surface charge to the MXene nanosheets and contribute to the interplanar spacing. One of the seminal articles on the MXene-based 2D layered membranes for NRED was published by Wang and coworkers in 2019.[175] The authors constructed lamellar $Ti_3C_2T_x$ membranes *via* the etching of Al from Ti_3AlC_2 followed by the assembly of the $Ti_3C_2T_x$ dispersion by vacuum-assisted filtration (Fig. 14(a)). The resultant device exhibited a highly charged state at alkaline pH that, in combination with the low membrane resistance, enabled them to harvest an output power of 21 W m^{-2} and maximum efficiency of 40% applying a 1000-fold concentration gradient at room temperature (Fig. 14(b)). Furthermore, the increment in the temperature allowed maximizing the ion mobilities and the surface charge yielding a PD_{max} of 54 W m^{-2} (Fig. 14(c)).

Exploiting the same material, Zhang *et al.* built a composite membrane based on $Ti_3C_2T_x$ MXene and aramid nanofibers (MXene/ANFs) (Fig. 14(d)).[208] The aramid nanofibers not only offered negatively charged groups but also enlarged the interlayer channel and acted as an interlocking agent to connect the nanosheets by hydrogen bonding. The aramid nanofiber content on the composite membrane had to be optimized since an excessive amount reduced the ion flux due to partial blocking of the 2D channels (Fig. 14(e)). Thus, under optimized conditions, these authors reported a PD_{max} of 4.1 W m^{-2} by using seawater from the Mediterranean Sea and river water from the Elbe River as gradient sources. Additional theoretical and experimental results showed that the good performance is explained not only by the increment of surface charge (and interlayer channels) but also by the spatial distribution ("space charge") of charges offered by aramid nanofibers (Fig. 14(f)).

Recently, the development of a bio-inspired layer-by-layer assembled nanocomposite membrane (ABN) based on aramid nanofibers (ANFs) and boron nitride nanosheets (BNn) was reported.[124] The system was created by the layer-by-layer

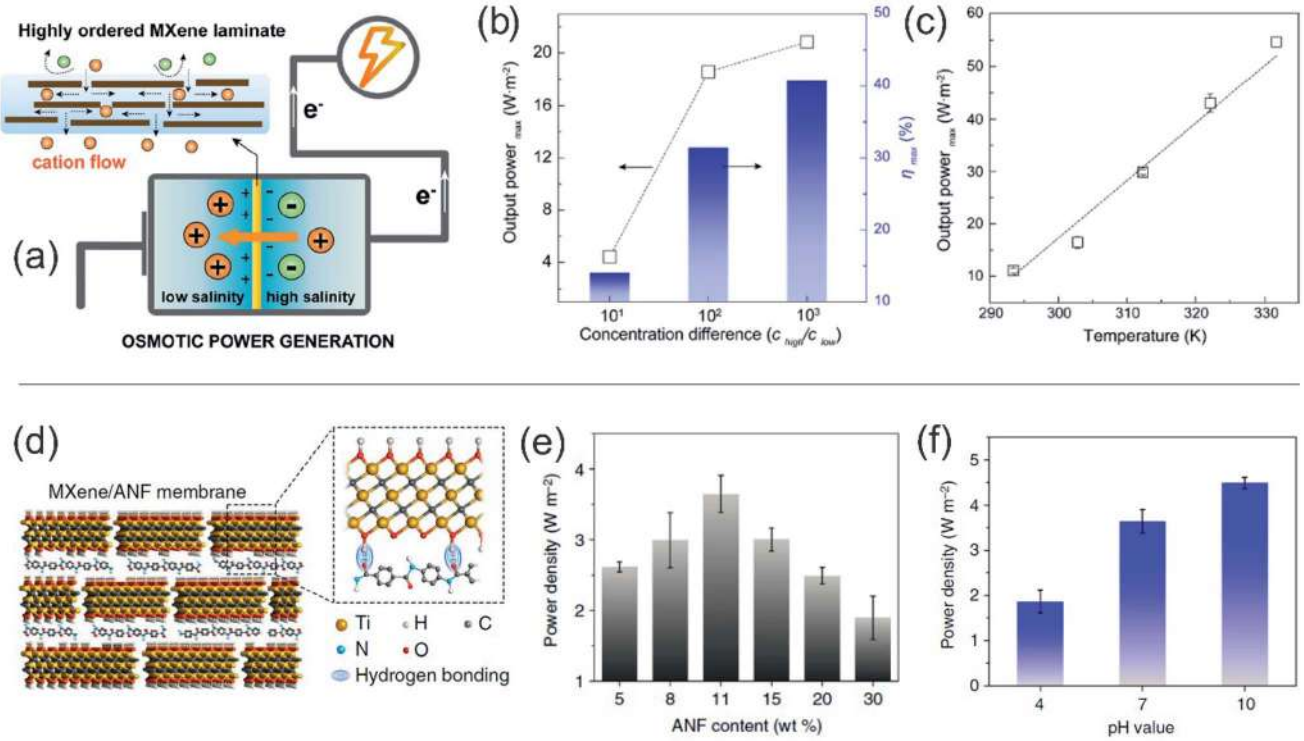

Fig. 14 (a) Scheme of the $Ti_3C_2T_x$ MXene membrane and the experimental set-up. (b) Output power density and the maximum efficiency extracted for different concentration gradients. (c) Power density as a function of the temperature. Adapted with permission.[175] Copyright 2019, American Chemical Society. (d) Schematic representation of $Ti_3C_2T_x$ MXene/aramid nanofiber (ANF) membrane structure (MXene/ANF). (e) Power density obtained for the composite membrane with different ANF contents. (f) Power density obtained for different pH values. Reproduced with permission.[208] Copyright 2019, The Author(s). Published by Springer Nature.

deposition of aramid nanofibers and boron nitride nanosheets onto a PDDA-pretreated glass. This revealed remarkable mechanical properties with a tensile strength of 370 MPa and chemical stability in a wide range of pH and temperature. The negative charge of ABN made it possible to use it as an electrical nanogenerator yielding an osmotic P_{max} density of 94 mW m^{-2} (without subtracting redox contribution $PD_{max} \sim 600$ mW m^{-2}) when applying a gradient of artificial seawater and river water. This result exceeds values obtained by other electrokinetic energy conversion methods.[242] Also, an NRED system constructed with 10 tandem-connected osmotic cells was able to supply electronic devices with a liquid crystal display and the ABN-based membrane was able to act as a nanopower generator even with organic solvents.[243] Interestingly, these results were obtained using an effective area of 3.14 mm^2 but, when the effective area was decreased to 0.03 mm^2, P_{max} density was boosted to 5.9 W m^{-2} (without subtracting redox contribution). This finding suggests a non-linear behavior of the response in terms of the effective areas. For this reason, the article highlights the importance to perform the NRED experiments under conditions that emulate practical applications. The trade-off between the output power and working area was also evidenced by Chen *et al.* in the study of the energy conversion performance of a nanocomposite membrane based on aramid nanofibers and graphene oxide.[238]

7.2 3D-materials and other multi-channel membranes for the development of SGE nanodevices

With the purpose of developing platforms with technological applications, the scientific community has made considerable efforts during recent years to achieve an efficient scale-up to multi-channel membranes. The employment of 3D materials has been proposed as a simple way to obtain membranes with low cost and easy scalability acting as efficient SGE devices.[65,135,184,244,245] The combination of interconnected 3D nanostructured networks together with the high surface and space charge leading to high conductance and selectivity has been identified as determining factors.[246] In the last year, several proofs-of-concept have been introduced in the synthesis, characterization, and energy conversion testing of these materials. Zhang *et al.* introduced an organic heterogeneous membrane constructed by the integration of a functional polyelectrolyte hydrogel based on polystyrene sulfonate (PSS) on a porous aramid nanofiber (ANF) membrane *via* the sequential blade-casting method (210 μm-thick) (Fig. 15(a)).[64] The chemical, electrostatic, and structural asymmetries resulted in a rectifying behavior with surface-charge-governed ion conductance below 0.1 M KCl. Furthermore, the enhancement of ion diffusion caused by a widely charged 3D hydrogel network added to the high cation selectivity provided by negative groups of PSS and ANF, and the advantages of interfacial design allowed it to act as an efficient energy nanogenerator. In order to obtain the best performance, both the gradient direction as well as the PSS content in the hybrid membrane were optimized. On the one hand, the results evidenced an increment in the power by establishing the ion diffusion direction from the ANF membrane to the PSS hydrogel (forward gradient) (Fig. 15(b) and (c)). On the other hand, an increment of PSS content up to 7% wt led to a boost in the power due to the increment in the surface charge (Fig. 15(d)). Additional increments of PSS are counterproductive owing to the increase of steric hindrance and concomitantly, a decrease in the ion flux. Finally, under optimized conditions, the device displayed a P_{max} density of ~5.06 W m^{-2} by mixing natural seawater and river water (~130-fold) exceeding the commercialization benchmark (Fig. 15(e)). This work demonstrated the technological potential of heterogeneous membranes based on 3D polyelectrolyte hydrogels as SGE platforms.

Recently, nanoporous membranes containing metal–organic frameworks (MOFs) or covalent organic frameworks (COFs) have emerged as an attractive approach due to the exceptional properties of these materials such as their distribution of ordered sub-nanochannels, the tailorable surface properties, the high surface area, and relatively straightforward chemical synthesis.[223,247,248] In this regard, Zhao *et al.* introduced an inorganic–organic composite membrane that consisted of the integration of MOF nanosheets into a heterogeneous organic membrane.[249] This ion-selective membrane was created in a two-step process. First, a sulfonated polysulfone (SPSF) solution was cast and, subsequently, dried on a Si wafer. Then, a dispersion of sulfonated poly(ether etherketone) (SPEEK) and previously synthesized MOF nanosheets (zinc(II) tetrakis(4-carboxy-phenyl)porphyrin) was spin-coated on the SPSF modified substrate (Fig. 16(a)). The formed membrane (MOF–SPEEK/SPSF) had a total thickness of 4.3 μm and displayed a good cation selectivity ascribed to the presence of sulfonated groups (Fig. 16(b)). Moreover, energy conversion experiments showed an enhancement of power output of the MOF–SPEEK/SPSF (6.96 W m^{-2}) compared to those obtained with the SPSF (2.7 W m^{-2}) and SPEEK/SPSF (5.95 W m^{-2}) membranes when a 50-fold salinity gradient was applied (Fig. 16(c)). These results were attributed to both the asymmetrical structure and the diminution of ion transport resistance promoted by the high porosity of MOF. Furthermore, this value could be maximized to 7.9 W m^{-2} and 24 W m^{-2} by setting the pH = 11 and applying a 500-fold salinity gradient respectively (Fig. 16(d)). Finally, the authors introduced a novel method to apply a temperature gradient by irradiating a Si wafer with light.

The functionalization of nanochannels with different molecular systems has been one of the most applied approaches to obtain a high performance in multi-channel membranes.[169,218,219,250–255] Liu *et al.* developed a highly selective nanoporous membrane based on the integration of the MOF UiO-66-NH_2 onto the surface of a highly ordered AAO membrane (UiO-66-NH_2–AAO).[224] The composite membrane was created by *in situ* growth of the MOF UiO-66-NH_2 onto a pre-synthesized AAO membrane modified with 3-triethoxysilylpropylamine (APTES). The previous modification of the AAO membrane with the APTES is a crucial step since it acts as a crosslinker enabling the successful integration of the MOF. Despite the asymmetric structure, the UiO-66-NH_2–AAO membrane displayed a low rectifying behavior which was ascribed to the trade-off between asymmetric wettability and

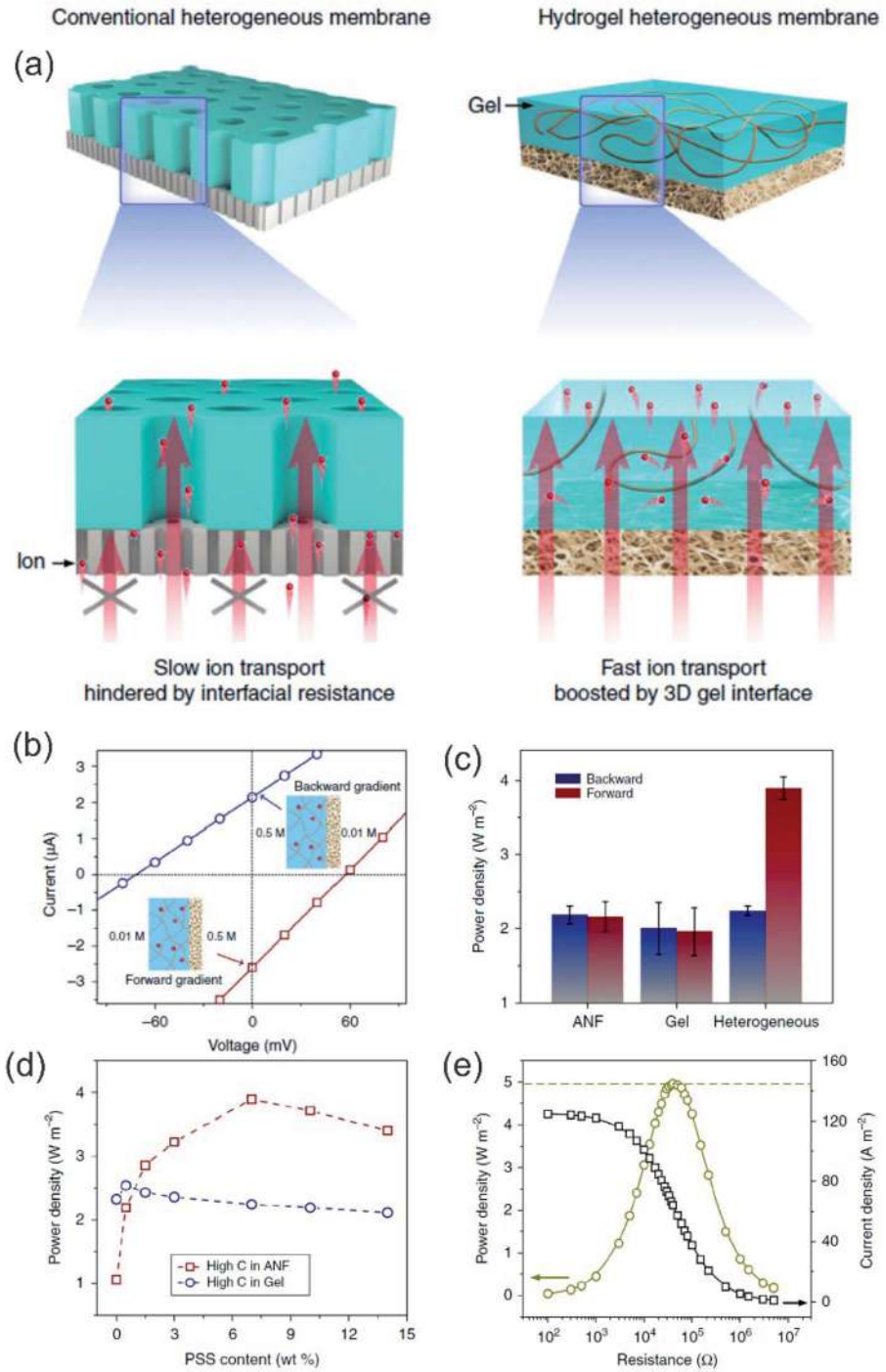

Fig. 15 (a) Scheme of hydrogel heterogeneous membrane structure constituted by a polystyrene sulfonate (PSS) film onto a porous aramid nanofiber membrane (ANF). The 3D gel interface enabled fast ion transport regarding the conventional heterogeneous membrane structure. (b) *I*–*V* curves applying a 50-fold gradient under different directionalities. (c) Power density for the hybrid membrane and the isolated building blocks in both gradient directions. (d) Power density *vs.* the PSS content. The graph depicts the trade-off between the increment of surface charge and the increment of steric hindrance. (e) Power density and current density in terms of load resistance applying a gradient of natural seawater and river water (~130-fold). Reproduced with permission.[64] Copyright 2020, The Author(s). Published by Springer Nature.

asymmetric pore-structure. The study of ion transport at different electrolyte concentrations showed a charge-governed transport below 1 M KCl due to the positively charged MOF and AAO membrane under neutral pH conditions. The ion-selective behavior was exploited in SGE experiments. The exposure of the composite membrane to asymmetric electrolyte concentrations (1000-fold KCl) evidenced the generation of $I_0 = 1.81$ μA and $E_m = 72.7$ mV when the MOF side was exposed to the concentrated solution (forward direction). The exposure of the MOF side to the diluted solution (the reverse direction)

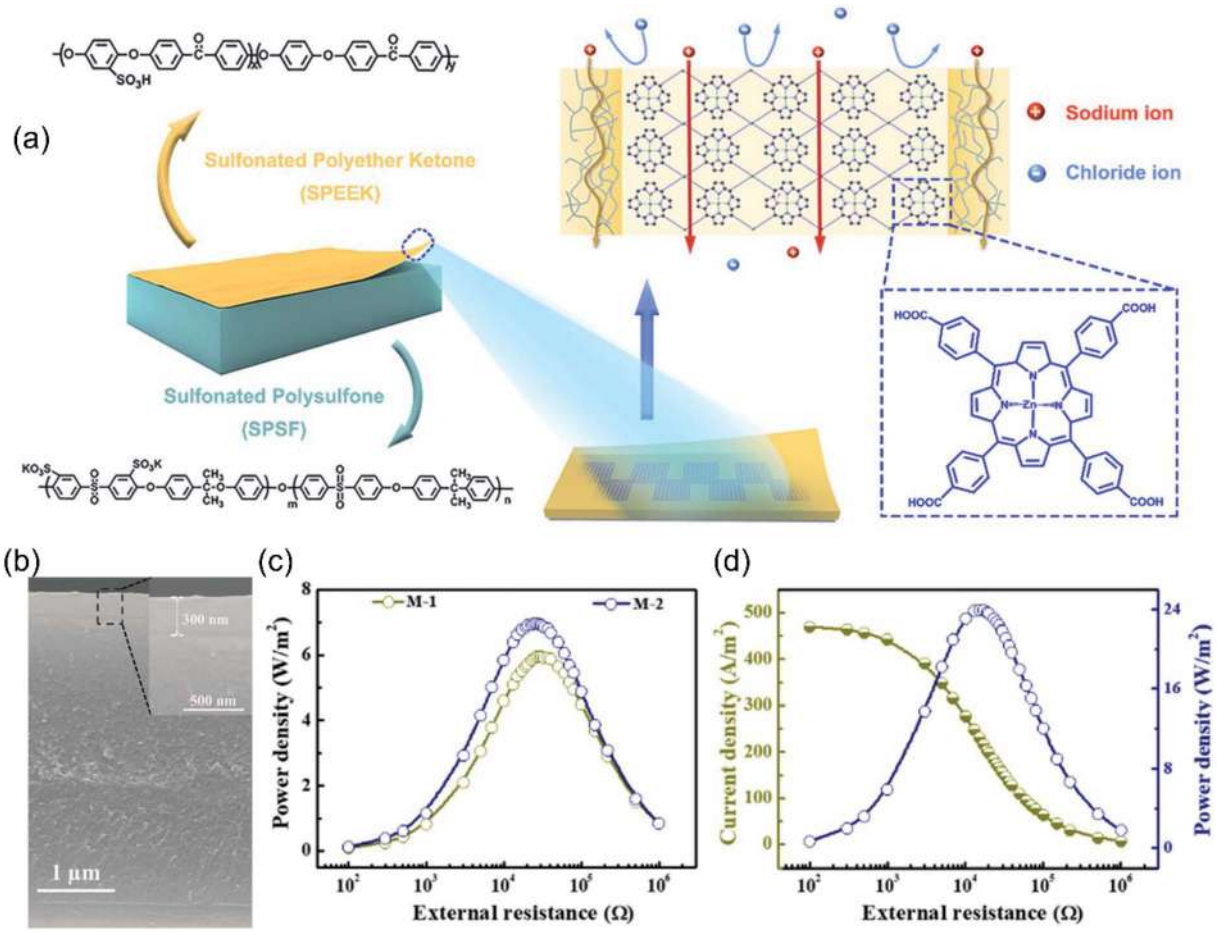

Fig. 16 (a) Schematic illustration and (b) scanning electron microscopy image of the inorganic–organic composite membrane metal–organic framework–sulfonated poly(ether etherketone)–polysulfone (MOF–SPEEK/SPSF). The zoom-in image demonstrates the asymmetric structure. (c) Power density in terms of load resistance for the SPEEK/SPFS (M-1) and MOF–SPEEK/SPSF (M-2) membranes applying a 50-fold gradient. The integration of MOF in the heterogeneous membrane led to an increment in the output power. (d) Power density in terms of load resistance for the MOF–SPEEK/SPSF membrane applying a 500-fold gradient. Reproduced with permission.[249] Copyright 2020 Elsevier Ltd. All rights reserved.

showed a clear diminution in the power capability. In this way, the analysis of power capabilities by *P–R* curves exhibited a respective value of 4.93 W m^{-2} and 7.12 W m^{-2} at 50-fold and 500-fold of KCl forward asymmetric concentration. Usually, it is assumed that the diffusion coefficients are the most relevant factor in the selection of the electrolyte. However, when nanoporous membranes based on MOFs are used, the hydrated ion radius acquires a central role due to the comparable magnitude of this parameter and the size of MOF cavities, as commented above. In this case, the performance as SGE of the composite membrane for a 100-fold gradient displayed power densities around 28.6 W m^{-2}, 11.0 W m^{-2}, and 0.0216 W m^{-2} for KBr, KCl, and KNO_3 respectively. Considering that the relationship between hydrated anion radii is Br^- (6.62 Å) < Cl^- (6.64 Å) < NO_3^- (6.70 Å) and the pore size of UiO-66 is around 6–7 Å, this trend was attributed to partial size exclusions in the MOF porosity. Finally, the composite membrane presented good stability showing a loss in the power capability of only 12% after seven days.

Xin *et al.* introduced a heterogeneous nanofluidic device created by the deposition of the abundant biomaterial silk nanofibers (SNF) onto a porous AAO substrate (Fig. 17(a)).[256] The hybrid membrane displayed interesting properties such as mechanical robustness, aqueous stability, long-term stability, and surface-charge-governed transport at high KCl concentration. The energy conversion properties were ascribed to the synergic mechanism of ion storage of the AAO substrate and the ionic selectivity of the SNF layer (Fig. 17(b)). Considering this mechanism, these authors ensured that the relationship between the size of SNF and AAO pores played a central role. On the one hand, an excessive decrease in the pore size of the AAO membrane (<70 nm) limited the effective contact between the SNF film and the AAO pores yielding a decrease in the power. On the other hand, an excessive increment in the pore size of the AAO membrane (>110 nm) reduced the ion storage capability of the AAO membrane diminishing the output power (Fig. 17(c)). Thus, by optimizing the pore size of the AAO membrane and the length of SNF film, this device was able to act as a nanopower generator with an artificial sea–river water system obtaining a maximum P_{max} density of 2.86 W m^{-2} under alkaline conditions (Fig. 17(d)). This value was enhanced by incrementing the

concentration gradient. Moreover, the system achieved SGE conversion efficiently in a broad range of pH (Fig. 17(e)).

Polymer membranes with a large pore density have been extensively used for the development of SGE devices.[180,183,186,205,257,258] Similar to those results obtained in AAO, the main methodology is focused on the creation of heterogeneous membranes *via* the deposition of a highly charged layer on the membrane interface. For instance, Xu *et al.* presented the development of an asymmetric membrane by the integration of negatively charged 2,2,6,6-tetramethylpiperidine-1-oxyl radical oxidized cellulose nanofibers (TOCNs) (9 μm-thick) onto a porous track-etched PET substrate (12 μm-thick; pore density ~10^8 pores per cm^{-2}).[182] The hybrid system displayed unique rectification properties and cation selectivity ascribed to the asymmetrical structure and the high negative charge density of the TOCN layer. Furthermore, supported by PNP simulations, the authors ensured that the heterogeneous membrane configuration allowed weakening of the ICP on the TOCN side. Exploiting these features, the NRED membrane showed a PD_{max} of ~0.96 W m^{-2} with efficiencies around 25.2%

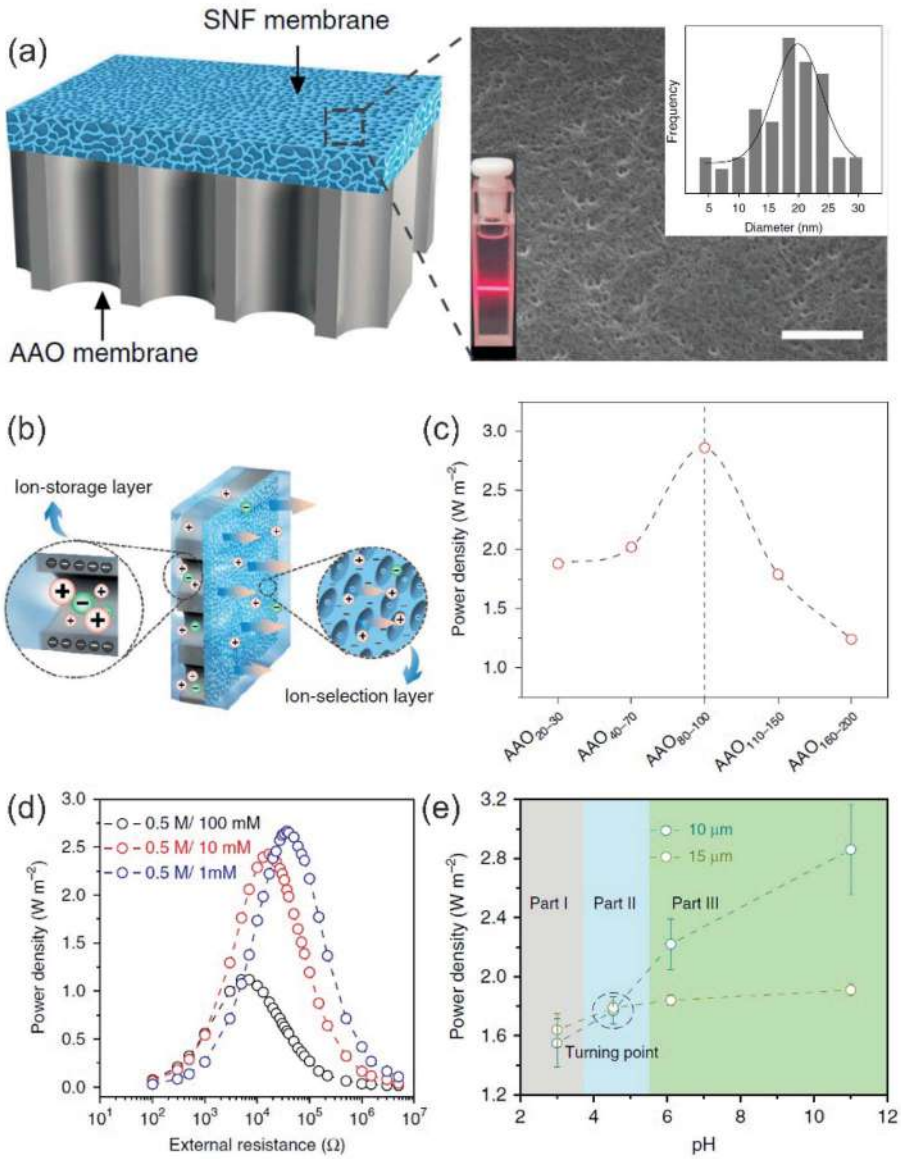

Fig. 17 (a) Scheme of the hybrid membrane created by the integration of the silk nanofibers (SNFs) onto the anodic aluminum oxide (AAO) membrane. Scanning electron microscopy image (scale bar 0.2 μm) of the SNF surface containing pores with an average diameter of around ~20 nm (inset). The Tindall effect promoted by the SNF solution is also shown. (b) Schematic representation of the AAO/SNF membrane. The AAO membrane acted as an ion storage layer, whereas the SNF film acted as an ion-selective layer. (c) Output power density in terms of the AAO pore size (the subindex refers to the pore size). Pore size between 80 and 100 nm led to an optimal response. (d) Extracted power density *vs.* the external resistance. (e) Power density as a function of the pH for two different SNF film thicknesses. The power displayed a maximum at basic pH. However, the hybrid system achieved a good performance in a broad range of pH. Reproduced with permission.[256] Copyright 2020, The Author(s). Published by Springer Nature.

mimicking the concentration gradient of seawater and river water. These values could be enhanced by alkalinizing the pH due to the deprotonation of carboxyl and hydroxyl groups of TOCNs and PET.

8 Upcoming challenges

Currently, there is vast knowledge about the main parameters affecting the energy performance in nanofluidic devices. Also, along Section 7, several articles based on up-scaled membranes either 2D or 3D materials achieving maximum power densities (PD_{max}) around or even exceeding the commercial benchmark (4–6 W m^{-2}) have been reported (Fig. 18). Undoubtedly, great advances in the use of nanoporous membranes as NRED devices at the laboratory scale have been achieved in the last few years. However, in order to convert these novel innovations into technological platforms, several issues must be tackled. In principle, there are, at least, three important issues that need to be addressed in the immediate future: (a) scaling-up the systems to realistic working areas and to reduce the ICP impact, (b) creation of full NRED cells, and (c) improvement of the mechanical and antifouling properties of nanoporous membranes.

8.1 Setting realistic scales for working areas

In Fig. 18, different reported PD_{max} values in terms of the membrane thickness are shown. Also, the color of the point indicates the working area employed. Results exposed in this figure denote the promising performances obtained in the last few years by employing nanoporous membranes. Furthermore, in several cases, the performances were compared (under the same conditions) with commercial membranes and these have shown overcoming energy capabilities.[219] However, the working area employed in each case is still far away from realistic values that enable the real application of these platforms. Specifically, most of the studies exhibiting output powers around the commercial benchmark were obtained with working areas below 0.1 mm^2. Considering that the degree of mixing with small areas is minimal, the driving force is maintained, and therefore, PD_{max} is maximized. However, under this condition, the amount of energy extracted is very low and therefore, constitutes a limitation.

In the last few years, several authors have expressed the relevance of increasing the working areas in order to mimic the real operation conditions.[124,208,238] The increment of the working area allows enhancement of the energy produced by a certain volume of solution (an increase of extractable energy efficiency) since this fact leads to transport of more moles of ions and, concomitantly, mixing of the solution. However, this increment dramatically affects the output power since more mixing reduces the gradient concentration and concomitantly, the driving force of SGE.[108,238] Thus, to obtain an adequate balance between energy efficiency and PD_{max}, it is imperative to increase the working areas beyond the millimeter scale.

The trade-off between extractable energy and PD_{max} by increasing the working area can be related to the previously

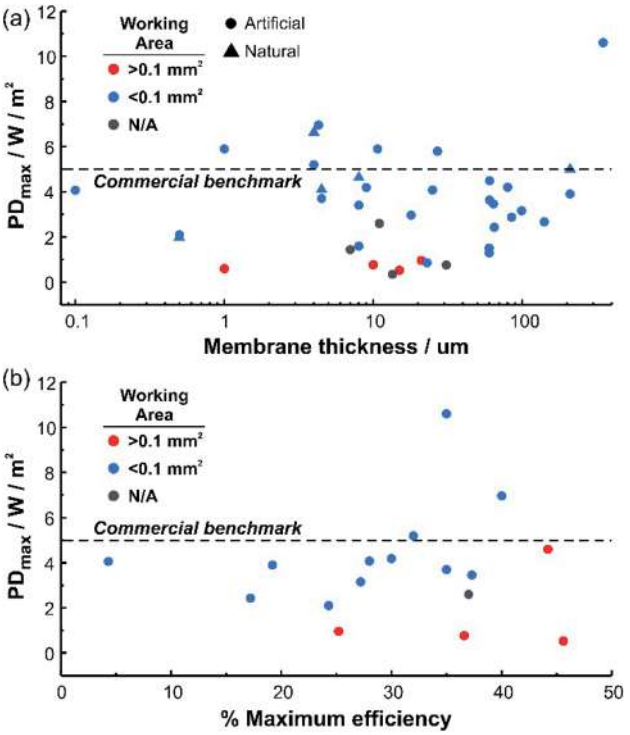

Fig. 18 Maximum power density (PD_{max}) as a function of the membrane thickness (a) and the maximum efficiency (b) for most of the different studies addressed in Section 7. Data are also summarized in Table 1.

explained commitment relationship between the output power and pore-density due to the ICP effect (Section 6).[107] While it is possible to despise this phenomenon in single-pore systems, ICP acquires a central role in nanoporous membranes. One way to analyze the ICP is considering that this leads to changes in the concentrations (or activities) at the membrane surface and, concomitantly, generates a diminution in the effective concentration gradient.[108] As depicted in eqn (27), this diminution in the gradient magnitude and, therefore in the driving force of NRED, has a direct consequence on P_{max},

$$P_{max} = \frac{\left[(2t_+ - 1)\frac{RT}{F}\ln\left(\frac{a_H}{a_L}\right)\right]^2}{4R_c} \quad (44)$$

Analyzing from another perspective, it is possible to consider that the ICP generates an increase in the entering resistance (*i.e.* the resistance in the reservoir and at the membrane/reservoir interface) as a result of which the extracted power vanishes.[107] Thus, beyond the conceptual richness of eqn (27), this equation is only applicable for ideal cases since if an equivalent electrical circuit is created, the presence of ICP (or diffusion boundary layers) introduces a new external resistance (in some articles referred to as boundary layer resistance, r_{BL}). From a theoretical perspective, this resistance is not accounted for by eqn (27). However, it is so relevant that the increase of the membrane conductance ($1/R_c$) above 10^5 S m^{-2} could not increase the obtained power due to the dominant role of r_{BL}.[108]

It is worth mentioning that, usually, the relationship between pore density and power has been mostly studied *via* numerical methods or in systems with very accurate control of porosity. Undoubtedly, these studies provided invaluable information about the fundamental basis of the scaling-up problem and constitute the foundations to address the creation of efficient membranes with high-pore density. However, it is necessary to be aware that, in practice, some additional issues not contemplated in fundamental studies could arise about this point. Some examples could involve the appearance of micrometer-sized defects and partial loss of mechanical properties due to the high porosity. In both cases, these facts could be another source of power capability loss. In this context, the scaling-up of nanoporous membranes remains a major challenge. In the last few years, several authors have found that the ICP can be diminished by optimizing several nanofluidic parameters such as channel size (see Section 6.4), channel length (see Section 6.3), the asymmetric integration of different building blocks (heterogeneous membranes) (see Section 6.5), or even the application of different temperature gradients (see Section 6.8).[193,211,229]

8.2 Full NRED cells

If the efficiency of extractable energy is considered, the use of a single nanoporous membrane (cation- or anion-selective) to construct the cell results in an inefficient NRED device (and even more if the currently employed working areas are considered).[107,108] This configuration only enables the diffusion of one kind of ion and consequently, it only allows harvesting (in an ideal process) half of the Gibbs free energy available. In contrast, the stacking of cation-selective and anion-selective nanoporous membranes separated by concentrated and diluted solutions makes it possible to appreciably increase the open-circuit voltage. This full cell configuration employing nanofluidic devices has already shown some promising results.[53,123] It is worth mentioning that while under ideal conditions the potential should scale linearly (eqn (42)), in practice, this increment rate is not achievable due to different sources of energy losses (*e.g.* ohmic resistance). In these cases, the optimization of several cell parameters, such as the reservoir thickness, is of paramount importance.[108]

For its part, the creation of full NRED cells involves the generation of both anion-selective and cation-selective membranes and this fact is a challenge that needs to be further addressed.[57] Considering the up-scaled devices cited in Table 1, only 25% of the reported systems correspond to anion-selective nanoporous membranes, which seem to be a major challenge.[224]

8.3 Improving the mechanical and antifouling properties of membranes

The membrane can be considered the heart of RED and NRED devices and, for this reason, it is highly desirable that certain features related to their mechanical and antifouling properties are accomplished. In Section 5, Nanofabrication methods, the main methods used for the development of NRED devices were introduced. Aiming to convert these novel platforms into applicable devices, the nanofabrication methods and the materials must enable us to not only obtain membranes with mechanical properties that ensure long durability but also easy and low-cost scalability.[57] Considering the eventual challenge of large-scale production, the study of different straightforward and robust chemical routes for the reproducible development of nanoporous membranes is needed. In this way, some studies have shown interesting procedures for the development of efficient membranes by combining relatively simple protocols and bioabundant materials.[256,259] However, until now, these issues have not been exhaustively studied.

Moreover, in contrast to laboratory experiments, water sources employed in up-scaled RED devices are expected to contain different non-desirable inorganic, organic and microbial constituents.[107,260] This acquires more relevance when the system operates with natural sea and river water since these materials could deposit onto the membrane promoting a dramatic decrease in the energy capabilities especially in anion-selective membranes.[261,262] Affordable ways to prevent fouling could involve the integration of different building blocks onto the NRED membrane surface with antifouling properties.[52,263,264] In this regard, the functionalization of membranes with 2D materials with antifouling properties has been highlighted as an interesting alternative.[57] Besides, in all the cases, the pretreatment of water and defouling generate non-negligible energy consumption. In order to be economically viable, these costs must also be afforded by the NRED system. Considering the early stage of development of NRED, this issue also remains scarcely studied.

8.4 Expanding the SGE possibilities

As has been addressed throughout the review, the current state of RED is not still completely viable in economic terms. On the other hand, while the use of nanoporous membranes has shown promising results at the laboratory scale, its future at the large scale is also uncertain. In this context, to expand the possibilities of SGE-based methods, researchers have proposed different alternatives such as desalination and energy conversion. In general, these alternatives were applied in RED systems rather than NRED. In this line, in order to analyze the economic potential of NRED, the study of these different alternatives will be imperative. In the following, these alternatives will be briefly explained (for further details ref. 18 is recommended).

8.4.1 Energy conversion. The power generated by RED (or eventually NRED) systems can be stored either by hydrogen production or converting into a storage battery.[18,26] In the former case, the hydrogen ion can be reduced in the cathode to form H_2 whereas the hydroxide ion is oxidized in the anode to form O_2 (water splitting). The potential needed for this process could be produced either by placing a RED stack between the cathode and anode (internal integration) or externally applying the RED process (external integration). Considering the growing interest in the use of H_2 as a fuel, its generation *via* SGE methods has been addressed in recent years.[265–268] Exploiting a similar concept, the combination of RED with microbial fuel cells for both H_2 production as well as CO_2 reduction into

Table 1 Summary of some of the up-scaled systems addressed in this review[a,b]

Membrane type	Description	Thickness/μm	Gradient concentration	PD_{max}/W m^{-2}	%η	Working area/mm^2	Ref.
2D and ultrathin membranes	Graphene oxide membranes (membrane pair)	10	50-fold (artificial, NaCl)	0.77	36.6	0.8	123
	Graphene oxide membrane vertically oriented	350	50-fold (artificial, NaCl)	10.6	35	~0.009	233
	Graphene/CNF membrane	9	50-fold (artificial, NaCl)	4.19	30	0.03	228
	Graphene/PPSU–Py copolymer	31	50-fold (artificial, NaCl)	0.76	N/A	N/A	237
	Black phosphorus membrane	8	50-fold (artificial, NaCl)	1.6	N/A	0.03	170
	Black phosphorus/graphene oxide composite membrane	8	50-fold (artificial, NaCl)	3.4	N/A	0.03	170
	Black phosphorus/graphene oxide composite membrane	8	150-fold (natural)	4.7	N/A	0.03	170
	MoS_2 nanosheets/CNF composite membrane	4	50-fold (artificial, NaCl)	5.2	32	0.03	172
	MoS_2 nanosheets/CNF composite membrane	4	~50-fold (natural sea water)	6.7	N/A	0.03	172
	$Ti_3C_2T_x$ membrane	2.7	1000-fold (artificial, KCl)	20.85	40.6	0.0163	175
	$Ti_3C_2T_x$ membrane	15	50-fold (artificial, NaCl)	0.53	45.6	0.78	241
	$Ti_3C_2T_x$ membranes (membrane pair)	N/A	50-fold (artificial, NaCl)	4.6	44.2	0.2	53
	$Ti_3C_2T_x$ membrane	N/A	50-fold (artificial, NaCl)	0.00168 (with light)	N/A	N/A	203
	$Ti_3C_2T_x$/ANF composite membrane	4.5	50-fold (artificial, NaCl)	~3.7	35	0.03	208
	$Ti_3C_2T_x$/ANF composite membrane	4.5	150-fold (natural)	4.1	N/A	0.03	208
	ANF/boron nitride nanosheets	1	50-fold (artificial, NaCl)	5.9	N/A	0.03	124
	ANF/boron nitride nanosheets	1	50-fold (artificial, NaCl)	0.6	N/A	3.14	124
	Carbon nitride membrane	0.25	1000-fold (artificial, KCl)	0.21	N/A	N/A	166
	Silk fibroin membrane	0.1	50-fold (artificial, NaCl)	4.06	4.3	0.03	289
	Reconstructed nanokaolinite membranes	25	100-fold (artificial, KCl)	0.18	44.2	0.2	171
	Block copolymer membrane	0.5	50-fold (artificial, NaCl)	2.1	24.3	0.03	209
	Block copolymer membrane	0.5	Natural sea and river water	2.04	N/A	0.03	209
	Core–rim polycyclic aromatic hydrocarbon membrane	2×10^{-3}	Artificial sea and river water	67	8	3×10^{-6}	113
3D and multipore membranes	PAEK/PES composite membrane	11	50-fold (artificial, NaCl)	2.6	37	N/A	135
	SPEEK membrane	~27	50-fold (artificial, NaCl)	5.8	N/A	0.03	65
	Free-standing COF membrane	10.7	50-fold (artificial, NaCl)	5.9	N/A	0.03	248
	MOF–SPEEK/SPSF composite membrane	4.3	50-fold (artificial, NaCl)	6.96	40	0.03	249
	AAO/MOF (UiO-66-NH_2)	~18	50-fold (artificial, NaCl)	2.96	N/A	0.03	224
	AAO/MOF (UiO-66-NH_2)	~18	50-fold (artificial, KCl)	4.93	N/A	0.03	224
	AAO/MOF (UiO-66-NH_2)	~18	100-fold (artificial, KBr)	26.8	43.7	0.03	224
	AAO/MOF-199–PSS	85	50-fold (artificial, NaCl)	2.87		0.03	218
	PSS/ANF	210	50-fold (artificial, NaCl)	3.9	19.2	0.03	64
	PSS/ANF	210	130-fold (natural)	5.06	N/A	0.03	64
	Polymer polyphenylsulphone with pyridine (PPSU–Pyx)	7	50-fold (artificial, NaCl)	1.44	N/A	N/A	244
	AAO/mesoporous carbon	64.2	50-fold (artificial, NaCl)	3.46	37.3	0.03	219
	AAO/silk nanofibers	65	50-fold (artificial, NaCl)	2.43	17.2	0.03	256
	AAO/SPEEK	80	50-fold (artificial, NaCl)	4.2	N/A	0.03	181
	PET/TOCNs	21	50-fold (artificial, NaCl)	0.96	25.2	~9	182
	PET/BCP (polystyrene-*b*-poly(4-vinylpyridine))	13.5	50-fold (artificial, NaCl)	0.35	N/A	N/A	258
	PET/Cyt C	23	50-fold (artificial, NaCl)	0.86	N/A	0.03	290
	PC/Hydrogel (acrylic acid-*co*-acrylamide-*co*-methyl methacrylate)	25	50-fold (artificial, NaCl)	4.08	~28	0.03	183
	AAO/nanoporous polymeric membrane	~60	50-fold (artificial, KCl)	1.3	N/A	0.03	252
	AAO/nanoporous polymeric membrane	~60	Natural sea and river water	1.51	N/A	0.03	252
	AAO/ionomer (copolymer of tetrafluoroethylene and perfluoro (4-methyl-3,6-dioxa-7-octene-1-sulfonic acid)) membrane	~99.2	50-fold (artificial, KCl)	3.15	27.2	0.03	253

Table 1 (*Contd.*)

Membrane type	Description	Thickness/μm	Gradient concentration	PD_{max}/W m^{-2}	%η	Working area/mm^2	Ref.
	AAO/mesoporous silica	∼60	50-fold (artificial, NaCl)	4.5	N/A	0.03	250
	AAO/polyamide and graphene oxide	∼61.5	50-fold (artificial, NaCl)	3.73	N/A	0.03	169
	AAO/carbonaceous ordered mesoporous nanowires	∼135	50-fold (artificial, NaCl)	2.78	N/A	0.03	255
	Ionized wood (pair)	1000	60-fold (artificial, NaCl)	0.005	46.1	100	259

[a] N/A: not available. [b] For comparative purposes, mainly results at 50-fold gradients and under neutral pH conditions in up-scaled membranes were selected. In all cases, 50-fold gradient concentration corresponds to a gradient mimicking the sea/river water system, *i.e.* $C_H = 0.5$ M and $C_L = 0.01$ M.

different carbonaceous compounds has also been studied.[269–271] Remarkably, this last combination displayed better performance in terms of power and efficiency compared with the isolated constituents. Finally, in the case of storage batteries, the energy from the SGE system is converted into hydrogen and, subsequently, stored in a flow battery.[272–274]

8.4.2 Desalination. Desalination technologies are widely used for obtaining potable water from seawater.[275] This process generates brine solutions with a high salinity content (*e.g.* ∼1–2 M of NaCl) that can be used as the highly concentrated solution in the RED (or eventually NRED) process which could involve a benefit for the RED process in terms of power (see Section 6.6).[26,275] On the other hand, the energy produced by the RED can be used in the desalination process. Thus, different hybrid systems based on the combination of desalination technology and RED have been proposed, *e.g.* reverse osmosis (desalination technology) with RED.[275–279] Remarkably, this combination showed both diminution of energy consumption during the desalination process as well as mitigation of the environmental impact related to the disposal of desalination brine solutions.[280,281]

8.4.3 Closed-loop. Since its conception, RED (and NRED) has been mostly conceived for utilization in open-loop with river and seawater. While this setup has the main advantage of harnessing the energy directly from these natural sources, it also has some disadvantages such as: the system has to be installed in specific places (estuaries), the conditions of water are not stable (salinity and temperature) and, water pretreatment is required to avoid fouling of the membrane.[18] In this regard, the RED heat engine system appears as an interesting alternative.[232] In this procedure, the salinity gradient between the high- and low-concentration solutions is regenerated *via* thermal post-treatment with a heat engine. Thus, the effluents are firstly mixed during the RED process, and then, these are regenerated into the high- and low-concentration solutions by thermal treatment (*e.g.* using waste heat) and finally, coming back into the RED system (closed-loop). The regeneration can be achieved either by salt (*e.g.* using thermolytic salts) or solvent (*e.g.* membrane distillation) extraction.[18,232,282–284] Consequently, this technology also allows converting low-grade waste heat into energy which expands the application possibilities.[232]

9 Conclusions and perspectives

In summary, lab-scale experiments to generate sustainable and low-environmental impact from saline gradients employing nanofluidic devices have shown promising results. The reason is associated with the increment in the balance between resistance and selectivity displayed in nanofluidic membranes. Also, there is vast knowledge about the impact of different experimental variables such as electrolyte gradient, structural parameters, pH, and temperature, on the SGE conversion performance of nanoporous membranes. Undoubtedly, interdisciplinary efforts from different fields such as materials science, engineering, nanotechnology, and electrochemistry, will be key in the further growth of this emerging field. In particular, the integration of different building blocks for the creation of hybrid (or heterogeneous) nanoporous membranes based on either ultrathin, 2D, 3D, or multi-channel materials has shown to be an interesting alternative to find a good balance between ion selectivity and low ion resistance. By exploiting this strategy, a considerable amount of new nanoporous membranes displayed a response exceeding (or around) the commercial benchmark at laboratory scale (Fig. 18 and Table 1).

While the results obtained in the last few years are promising, there are some conditions and concepts that remain scarcely studied and need to be addressed in the immediate future. So far, most of the reported results were obtained using small working areas, which are not adequate for real applications as the great results in terms of power density and efficiency come together with low net energy values. As it was exposed, the increment in the working area results in a detriment in the power density, and therefore, it is an issue that must be tackled to convert these lab-scale innovations into promising technological platforms with real applications. Also, the transference of results obtained in single-pore systems to upscaled nanoporous membranes remains a challenge, the reason behind this behavior is related to the ICP effect and consequently, the drastic diminution in the driving force of salinity gradient power, the effective concentration gradient. These issues are perhaps the main problems to be faced in the immediate future.

On the other hand, most of the studies introduced in NRED are based on half-cells, *i.e.* the cell is constituted by a single nanoporous membrane (anion or cation-selective) separating the reservoirs with the concentrated and diluted solutions. These configurations are ideal to study the performance of new membranes but, in order to enhance the extracted energy, it is also important to consider the design of full cells. This issue opens the doors to different problems still scarcely studied. For instance, the construction of full cells is linked to the availability of both cation and anion-selective membranes. While the design of efficient up-scaled nanoporous membranes has rapidly grown over the last few years, it is important to look for further chemical and nanofabrication routes conferring optimum mechanical properties and promising scalability. Moreover, except for some examples of anion-selective membranes with appreciable energy-conversion performance, the design of this kind of membrane, in particular, is still a major challenge. On the other hand, the importance of scaling the systems to full cells brings with it the need to optimize several parameters related to the cell architecture, fluid management, and electrodes to diminish the energy loss.[285]

Usually, NRED is designed to be applied to sea and river water due to their wide availability. However, the aperture to different effluents could not only increase the technological potential of this emerging field but also enables the exploitation of different water and organic wastes. In this regard, the understanding of ion transport and specifically, the energy conversion properties of these nanoporous membranes exposed to organic solvents remains limited. Furthermore, beyond the specific source, the use of different waste or natural effluents involves the presence of different non-desirable compounds. This fact denotes the importance of implementing different antifouling strategies to supply the NRED systems. Again, this highlights the importance of further developing different chemical and physical routes for the creation of nanoporous membranes with not only tailorable ion transport but also fulfilling other requirements related to the cost, scalability, and long-term stability.

It is important to highlight the wide range of opportunities to couple NRED systems with different devices and technologies. Considering that NRED is in the early stage of development, this issue has not been deeply addressed. Nevertheless, several examples are employing RED systems combined with other technologies to expand the possibilities of this field.[18] In this regard, several authors have proposed different ways of storing the energy provided by RED.[265–267] Also, by taking advantage of low-grade waste heat, RED systems can be used in a closed-loop.[232] The RED devices can be coupled with different desalination technologies enabling both a decrease in energy consumption and environmental impact.[277,278,286] Finally, several authors have proposed the use of RED for water remediation by the direct or indirect reactions in the electrode chambers.[287,288] These applications need to be addressed in the years to come.

Even though much work still needs to be done to turn the lab-scale nanoporous membranes into platforms with real applications, the results obtained in this emerging field are promising.

Author contributions

All the authors contributed to the bibliographic research, discussion, writing and revision of the article.

Conflicts of interest

There are no conflicts to declare.

Acknowledgements

G. L. acknowledges a doctoral scholarship from CONICET and a short-term grant from DAAD. G. L. would also like to acknowledge the support of the GET_INvolved program of GSI. W. A. M. and O. A. are CONICET fellows and acknowledge financial support from Universidad Nacional de La Plata (PID-X867) and ANPCyT (PICT-2017-1523 and PICT-2016-1680). C. T. and M. E. T. M. acknowledge support by the LOEWE project iNAPO funded by the Hessen State Ministry of Higher Education, Research and Arts.

References

1 S. Chu, Y. Cui and N. Liu, *Nat. Mater.*, 2017, **16**, 16–22.
2 S. Chu and A. Majumdar, *Nature*, 2012, **488**, 294–303.
3 P. A. Østergaard, N. Duic, Y. Noorollahi, H. Mikulcic and S. Kalogirou, *Renewable Energy*, 2020, **146**, 2430–2437.
4 M. S. Nazir, A. J. Mahdi, M. Bilal, H. M. Sohail, N. Ali and H. M. N. Iqbal, *Sci. Total Environ.*, 2019, **683**, 436–444.
5 A. Hussain, S. M. Arif and M. Aslam, *Renewable Sustainable Energy Rev.*, 2017, **71**, 12–28.
6 E. Kabir, P. Kumar, S. Kumar, A. A. Adelodun and K.-H. Kim, *Renewable Sustainable Energy Rev.*, 2018, **82**, 894–900.
7 B. E. Logan and M. Elimelech, *Nature*, 2012, **488**, 313–319.
8 G. Z. Ramon, B. J. Feinberg and E. M. V. V. Hoek, *Energy Environ. Sci.*, 2011, **4**, 4423.
9 S. E. Skilhagen, *Desalin. Water Treat.*, 2010, **15**, 271–278.
10 N. Y. Yip and M. Elimelech, *Environ. Sci. Technol.*, 2012, **46**, 5230–5239.
11 A. Siria, M.-L. Bocquet and L. Bocquet, *Nat. Rev. Chem.*, 2017, **1**, 0091.
12 R. E. Pattle, *Nature*, 1954, **174**, 660.
13 R. S. Norman, *Science*, 1974, **186**, 350–352.
14 S. Loeb, Method and apparatus for generating power utilizing pressure-retarded-osmosis, *US Pat.*, US3906250A, Sept. 16,1975.
15 S. Loeb, Method and apparatus for generating power utilizing reverse electrodialysis, *US Pat.*, US4171409A, Oct. 16, 1979.
16 R. E. Lacey, *Ocean Eng.*, 1980, **7**, 1–47.
17 M. Tedesco, E. Brauns, A. Cipollina, G. Micale, P. Modica, G. Russo and J. Helsen, *J. Membr. Sci.*, 2015, **492**, 9–20.
18 H. Tian, Y. Wang, Y. Pei and J. C. Crittenden, *Appl. Energy*, 2020, **262**, 114482.

19 J. W. Post, J. Veerman, H. V. M. M. Hamelers, G. J. W. W. Euverink, S. J. Metz, K. Nymeijer and C. J. N. N. Buisman, *J. Membr. Sci.*, 2007, **288**, 218–230.
20 D. Brogioli, R. Zhao and P. M. Biesheuvel, *Energy Environ. Sci.*, 2011, **4**, 772.
21 D. Brogioli, *Phys. Rev. Lett.*, 2009, **103**, 058501.
22 R. A. Tufa, E. Curcio, E. Fontananova and G. Di Profio, in *Comprehensive Membrane Science and Engineering*, Elsevier, 2017, pp. 206–248.
23 M. Tedesco, A. Cipollina, A. Tamburini and G. Micale, *J. Membr. Sci.*, 2017, **522**, 226–236.
24 M. Tedesco, C. Scalici, D. Vaccari, A. Cipollina, A. Tamburini and G. Micale, *J. Membr. Sci.*, 2016, **500**, 33–45.
25 https://www.redstack.nl/.
26 R. A. Tufa, S. Pawlowski, J. Veerman, K. Bouzek, E. Fontananova, G. di Profio, S. Velizarov, J. Goulão Crespo, K. Nijmeijer and E. Curcio, *Appl. Energy*, 2018, **225**, 290–331.
27 A. Daniilidis, R. Herber and D. A. Vermaas, *Appl. Energy*, 2014, **119**, 257–265.
28 M. Tagliazucchi and I. Szleifer, *Chemically Modified Nanopores and Nanochannels*, Elsevier Inc., 1st edn, 2016.
29 G. Pérez-Mitta, C. Trautmann, M. E. Toimil-Molares and O. Azzaroni, in *Chemically Modified Nanopores and Nanochannels*, ed. M. Tagliazucchi and I. Szleifer, Elsevier, 2017, pp. 61–83.
30 M. Tagliazucchi and I. Szleifer, *Mater. Today*, 2015, **18**, 131–142.
31 Z. Zhang, L. Wen and L. Jiang, *Chem. Soc. Rev.*, 2018, **47**, 322–356.
32 X. Hou, W. Guo and L. Jiang, *Chem. Soc. Rev.*, 2011, **40**, 2385–2401.
33 C. Dekker, *Nat. Nanotechnol.*, 2007, **2**, 209–215.
34 G. Laucirica, Y. Toum Terrones, V. M. Cayón, M. L. Cortez, M. E. Toimil-Molares, C. Trautmann, W. A. Marmisollé and O. Azzaroni, *Nanoscale*, 2020, **12**, 18390–18399.
35 G. Pérez-Mitta, A. S. Peinetti, M. L. Cortez, M. E. Toimil-Molares, C. Trautmann and O. Azzaroni, *Nano Lett.*, 2018, **18**, 3303–3310.
36 G. Laucirica, G. Pérez-Mitta, M. E. M. E. Toimil-Molares, C. Trautmann, W. A. W. A. Marmisollé and O. Azzaroni, *J. Phys. Chem. C*, 2019, **123**, 28997–29007.
37 P. Wang, M. Wang, F. Liu, S. Ding, X. Wang, G. Du, J. Liu, P. Apel, P. Kluth, C. Trautmann and Y. Wang, *Nat. Commun.*, 2018, **9**, 569.
38 G. Pérez-Mitta, W. A. Marmisolle, L. Burr, M. E. Toimil-Molares, C. Trautmann and O. Azzaroni, *Small*, 2018, **14**, 1703144.
39 G. Xie, L. Wen and L. Jiang, *Nano Res.*, 2016, **9**, 59–71.
40 R. Li, X. Fan, Z. Liu and J. Zhai, *Adv. Mater.*, 2017, **29**, 1702983.
41 K. Xiao, L. Jiang and M. Antonietti, *Joule*, 2019, **3**, 2364–2380.
42 L. Wen, X. Hou, Y. Tian, J. Zhai and L. Jiang, *Adv. Funct. Mater.*, 2010, **20**, 2636–2642.
43 Y. Feng, W. Zhu, W. Guo and L. Jiang, *Adv. Mater.*, 2017, **29**, 1702773.
44 R. Qu, X. Zeng, L. Lin, G. Zhang, F. Liu, C. Wang, S. Ma, C. Liu, H. Miao and L. Cao, *ACS Nano*, 2020, **14**, 16654–16662.
45 J. Feng, M. Graf, K. Liu, D. Ovchinnikov, D. Dumcenco, M. Heiranian, V. Nandigana, N. R. Aluru, A. Kis and A. Radenovic, *Nature*, 2016, **536**, 197–200.
46 A. Siria, P. Poncharal, A. Biance, R. Fulcrand, X. Blasé, S. T. Purcell and L. Bocquet, *Nature*, 2013, **494**, 455–458.
47 Y. Xie, X. Wang, J. Xue, K. Jin, L. Chen and Y. Wang, *Appl. Phys. Lett.*, 2008, **93**, 163116.
48 F. Qian, W. Zhang, D. Huang, W. Li, Q. Wang and C. Zhao, *Phys. Chem. Chem. Phys.*, 2020, **22**, 2386–2398.
49 F. H. J. Van Der Heyden, D. Stein and C. Dekker, *Phys. Rev. Lett.*, 2005, **95**, 9–12.
50 J. Cervera, A. Alcaraz, B. Schiedt, R. Neumann and P. Ramírez, *J. Phys. Chem. C*, 2007, **111**, 12265–12273.
51 W. Guo, L. Cao, J. Xia, F. Q. Nie, M. Wen, J. Xue, Y. Song, D. Zhu, Y. Wang and L. Jiang, *Adv. Funct. Mater.*, 2010, **20**, 1339–1344.
52 Z. Jia, B. Wang, S. Song and Y. Fan, *Renewable Sustainable Energy Rev.*, 2014, **31**, 91–100.
53 L. Ding, D. Xiao, Z. Lu, J. Deng, Y. Wei, J. Caro and H. Wang, *Angew. Chem.*, 2020, **132**, 8798–8804.
54 T. Thorsen and T. Holt, *J. Membr. Sci.*, 2009, **335**, 103–110.
55 K. Gerstandt, K.-V. Peinemann, S. E. Skilhagen, T. Thorsen and T. Holt, *Desalination*, 2008, **224**, 64–70.
56 K. Xiao, L. Wen and L. Jiang, *Small*, 2016, **12**, 2810–2831.
57 M. Macha, S. Marion, V. V. R. Nandigana and A. Radenovic, *Nat. Rev. Mater.*, 2019, **4**, 588–605.
58 Y. Zhu, K. Zhan and X. Hou, *ACS Nano*, 2018, **12**, 908–911.
59 R. Spohr, *Ion Tracks and Microtechnology*, Vieweg+Teubner Verlag, Wiesbaden, 1st edn, 1990.
60 W. Kim and S. Nair, *Chem. Eng. Sci.*, 2013, **104**, 908–924.
61 Y. Kang, Y. Xia, H. Wang and X. Zhang, *Adv. Funct. Mater.*, 2019, **29**, 1902014.
62 Y. Zhou and L. Jiang, *Joule*, 2020, **4**, 2244–2248.
63 G. Laucirica, A. G. Albesa, M. E. Toimil-Molares, C. Trautmann, W. A. Marmisollé and O. Azzaroni, *Nano Energy*, 2020, **71**, 104612.
64 Z. Zhang, L. He, C. Zhu, Y. Qian, L. Wen and L. Jiang, *Nat. Commun.*, 2020, **11**, 875.
65 Y. Zhao, J. Wang, X.-Y. Kong, W. Xin, T. Zhou, Y. Qian, L. Yang, J. Pang, L. Jiang and L. Wen, *Natl. Sci. Rev.*, 2020, **7**, 1349–1359.
66 A. J. Bard and L. R. Faulkner, *Electrochemical Methods. Fundamentals and Applications*, Wiley, USA, 2nd edn, 2001.
67 J. N. Israelachvili, *Intermolecular and Surface Forces*, Elsevier, 3rd edn, 2011.
68 C. M. A. Brett and A. M. Oliveira Brett, *Electrochemistry: Principles, Methods, and Applications*, Oxford University Press, USA, 1993.
69 G. Pérez-Mitta, M. E. Toimil-Molares, C. Trautmann, W. A. Marmisollé and O. Azzaroni, *Adv. Mater.*, 2019, **31**, 1901483.

70 P. C. Hiemenz and R. Rajagopalan, *Principles of Colloid and Surface Chemistry*, Marcel Dekker, 3rd edn, 1997.
71 H.-J. Butt, K. Graf and M. Kappl, *Physics and Chemistry of Interfaces*, 2003.
72 T. Ma, J. M. Janot and S. Balme, *Small Methods*, 2020, **4**, 1–36.
73 I. Vlassiouk, S. Smirnov, Z. Siwyt and Z. Siwy, *Nano Lett.*, 2008, **8**, 1978–1985.
74 R. B. Schoch and P. Renaud, *Appl. Phys. Lett.*, 2005, **86**, 253111.
75 A. R. Poggioli, A. Siria and L. Bocquet, *J. Phys. Chem. B*, 2019, **123**, 1171–1185.
76 L. Bocquet and J.-L. Barrat, *Soft Matter*, 2007, **3**, 685.
77 S. Marbach and L. Bocquet, *Chem. Soc. Rev.*, 2019, **48**, 3102–3144.
78 L. Joly, C. Ybert, E. Trizac and L. Bocquet, *J. Chem. Phys.*, 2006, **125**, 204716.
79 L. Joly, C. Ybert, E. Trizac and L. Bocquet, *Phys. Rev. Lett.*, 2004, **93**, 257805.
80 Q. Xie, M. A. Alibakhshi, S. Jiao, Z. Xu, M. Hempel, J. Kong, H. G. Park and C. Duan, *Nat. Nanotechnol.*, 2018, **13**, 238–245.
81 T. Mouterde and L. Bocquet, *Eur. Phys. J. E: Soft Matter Biol. Phys.*, 2018, **41**, 148.
82 D. J. Rankin and D. M. Huang, *Langmuir*, 2016, **32**, 3420–3432.
83 R. Long, Y. Zhao, Z. Kuang, Z. Liu and W. Liu, *Desalination*, 2020, **477**, 114263.
84 L. Ma, K. Lin, Y. Qiu, J. Zhuang, X. An, Z. Yuan and C. Huang, *J. Phys. Chem. C*, 2021, **125**, 14195–14203.
85 J. Kuleszo, C. Kroeze, J. Post and B. M. Fekete, *J. Integr. Environ. Sci.*, 2010, **7**, 89–96.
86 O. A. Alvarez-Silva, A. F. Osorio and C. Winter, *Renewable Sustainable Energy Rev.*, 2016, **60**, 1387–1395.
87 X. Gao and C. Kroeze, *J. Integr. Environ. Sci.*, 2012, **9**, 177–190.
88 J. W. Post, C. H. Goeting, J. Valk, S. Goinga, J. Veerman, H. V. M. Hamelers and P. J. F. M. Hack, *Desalin. Water Treat.*, 2010, **16**, 182–193.
89 S. Pawlowski, J. Crespo and S. Velizarov, in *Electrokinetics Across Disciplines and Continents*, Springer International Publishing, Cham, 2016, pp. 57–80.
90 K. Nijmeijer and S. Metz, in *Sustainability Science and Engineering*, 2010, vol 2, pp. 95–139.
91 A. Cipollina and M. Giorgio, *Sustainable Energy from Salinity Gradients*, Elsevier/Woodhead Publishing, 2016.
92 J. W. Post, H. V. M. Hamelers and C. J. N. Buisman, *Environ. Sci. Technol.*, 2008, **42**, 5785–5790.
93 L. Zhang and X. Chen, *Angew. Chem., Int. Ed.*, 2013, **52**, 7640–7641.
94 A. Campione, L. Gurreri, M. Ciofalo, G. Micale, A. Tamburini and A. Cipollina, *Desalination*, 2018, **434**, 121–160.
95 H. Strathmann, *Ion-Exchange Membrane Separation Processes*, Elsevier Science, 1st edn, 2004, vol. 9.
96 H. Strathmann, A. Grabowski and G. Eigenberger, *Ind. Eng. Chem. Res.*, 2013, **52**, 10364–10379.
97 N. Lakshminarayanaiah, *Equations of Membrane Biophysics*, Academic Press Inc., UK, 1984.
98 A. H. Galama, J. W. Post, H. V. M. Hamelers, V. V. Nikonenko and P. M. Biesheuvel, *J. Membr. Sci. Res.*, 2016, **2**, 128–140.
99 Y. Tanaka, *Ion Exchange Membranes - Fundamentals and Applications*, Elsevier, 2007, vol. 12.
100 P. Ramirez, J. Cervera, V. Gomez, M. Ali, S. Nasir, W. Ensinger and S. Mafe, *J. Membr. Sci.*, 2019, **573**, 579–587.
101 J. Kim, S. J. Kim and D. K. Kim, *Energy*, 2013, **51**, 413–421.
102 D. K. Kim, C. Duan, Y. F. Chen and A. Majumdar, *Microfluid. Nanofluid.*, 2010, **9**, 1215–1224.
103 H. C. Yeh, C. C. Chang and R. J. Yang, *RSC Adv.*, 2014, **4**, 2705–2714.
104 J. Veerman and D. A. Vermaas, in *Sustainable Energy from Salinity Gradients*, Elsevier, 2016, pp. 77–133.
105 J. P. Hsu, S. C. Lin, C. Y. Lin and S. Tseng, *J. Power Sources*, 2017, **366**, 169–177.
106 J. Su, D. Ji, J. Tang, H. Li, Y. Feng, L. Cao, L. Jiang and W. Guo, *Chin. J. Chem.*, 2018, **36**, 417–420.
107 X. Tong, S. Liu, J. Crittenden and Y. Chen, *ACS Nano*, 2021, **15**, 5838–5860.
108 Z. Wang, L. Wang and M. Elimelech, *Engineering*, DOI: 10.1016/j.eng.2021.02.016.
109 J. C. Fair and J. F. Osterle, *J. Chem. Phys.*, 1971, **54**, 3307.
110 N. Y. Yip, D. A. Vermaas, K. Nijmeijer and M. Elimelech, *Environ. Sci. Technol.*, 2014, **48**, 4925–4936.
111 B. V. Derjaguin, S. S. Dukhin and M. M. Koptelova, *J. Colloid Interface Sci.*, 1972, **38**, 584–595.
112 C. Lee, C. Cottin-Bizonne, A.-L. Biance, P. Joseph, L. Bocquet and C. Ybert, *Phys. Rev. Lett.*, 2014, **112**, 244501.
113 X. Liu, M. He, D. Calvani, H. Qi, K. B. S. S. Gupta, H. J. M. de Groot, G. J. A. Sevink, F. Buda, U. Kaiser and G. F. Schneider, *Nat. Nanotechnol.*, 2020, **15**, 307–312.
114 G. Laucirica, M. E. Toimil-Molares, C. Trautmann, W. A. Marmisollé and O. Azzaroni, *ACS Appl. Mater. Interfaces*, 2020, **12**, 28148–28157.
115 R. S. Kingsbury, S. Flotron, S. Zhu, D. F. Call and O. Coronell, *Environ. Sci. Technol.*, 2018, **52**, 4929–4936.
116 H. Wang, L. Su, M. Yagmurcukardes, J. Chen, Y. Jiang, Z. Li, A. Quan, F. M. Peeters, C. Wang, A. K. Geim and S. Hu, *Nano Lett.*, 2020, **20**, 8634–8639.
117 W. Ouyang, W. Wang, H. Zhang, W. Wu and Z. Li, *Nanotechnology*, 2013, **24**, 345401.
118 D.-C. Zheng and L.-H. Yeh, *Micromachines*, 2020, **11**, 949.
119 M. Gao, P. Tsai, Y. Su, P. Peng and L. Yeh, *Small*, 2020, **16**, 2006013.
120 E. Güler and K. Nijmeijer, *J. Membr. Sci. Res.*, 2018, **4**, 108–110.
121 J. Veerman, M. Saakes, S. J. Metz and G. J. Harmsen, *Environ. Sci. Technol.*, 2010, **44**, 9207–9212.
122 R. Long, B. Li, Z. Liu and W. Liu, *Energy*, 2018, **158**, 427–436.
123 J. Ji, Q. Kang, Y. Zhou, Y. Feng, X. Chen, J. Yuan, W. Guo, Y. Wei and L. Jiang, *Adv. Funct. Mater.*, 2017, **27**, 1603623.
124 C. Chen, D. Liu, L. He, S. Qin, J. Wang, J. M. Razal, N. A. Kotov and W. Lei, *Joule*, 2020, **4**, 247–261.

125 J. Wang, M. Zhang, J. Zhai and L. Jiang, *Phys. Chem. Chem. Phys.*, 2014, **16**, 23–32.
126 S. Tseng, Y. M. Li, C. Y. Lin and J. P. Hsu, *Nanoscale*, 2016, **8**, 2350–2357.
127 S. Tseng, Y. Li, C. Lin and J. Hsu, *Electrochim. Acta*, 2016, **219**, 790–797.
128 J.-P. Hsu, T.-C. Su, C.-Y. Lin and S. Tseng, *Electrochim. Acta*, 2019, **294**, 84–92.
129 F. Xiao, D. Ji, H. Li, J. Tang, Y. Feng, L. Ding, L. Cao, N. Li, L. Jiang and W. Guo, *Inorg. Chem. Front.*, 2018, **5**, 1677–1682.
130 F. Xiao, D. Ji, H. Li, J. Tang, Y. Feng, L. Ding, L. Cao, N. Li, L. Jiang and W. Guo, *Mater. Chem. Front.*, 2018, **2**, 935–941.
131 Z. S. Siwy, *Adv. Funct. Mater.*, 2006, **16**, 735–746.
132 V. M. Cayón, G. Laucirica, Y. Toum Terrones, M. L. Cortez, G. Pérez-Mitta, J. Shen, C. Hess, M. E. Toimil-Molares, C. Trautmann, W. A. Marmisollé and O. Azzaroni, *Nanoscale*, 2021, **13**, 11232–11241.
133 G. Laucirica, W. A. Marmisollé, M. E. Toimil-Molares, C. Trautmann and O. Azzaroni, *ACS Appl. Mater. Interfaces*, 2019, **11**, 30001–30009.
134 G. Pérez-Mitta, A. Albesa, F. M. Gilles, M. E. Toimil-Molares, C. Trautmann and O. Azzaroni, *J. Phys. Chem. C*, 2017, **121**, 9070–9076.
135 X. Zhu, J. Hao, B. Bao, Y. Zhou, H. Zhang, J. Pang, Z. Jiang and L. Jiang, *Sci. Adv.*, 2018, **4**, eaau1665.
136 C. Trautmann, in *Ion Beams in Nanoscience and Technology*, ed. R. Hellborg, H. J. Whitlow and Y. Zhang, Springer-Verlag Berlin Heidelberg, 2009, pp. 369–387.
137 Z. Siwy and A. Fuliński, *Am. J. Physiol.*, 2004, **72**, 567–574.
138 P. Y. Apel, Y. E. Korchev, Z. Siwy, R. Spohr and M. Yoshida, *Nucl. Instrum. Methods Phys. Res., Sect. B*, 2001, **184**, 337–346.
139 Z. Siwy, P. Apel, D. Baur, D. D. Dobrev, Y. E. Korchev, R. Neumann, R. Spohr, C. Trautmann and K. O. Voss, *Surf. Sci.*, 2003, **532–535**, 1061–1066.
140 M. E. Toimil-Molares, *Beilstein J. Nanotechnol.*, 2012, **3**, 860–883.
141 P. Y. Apel and D. Fink, in *Transport Processes in Ion-Irradiated Polymers*, ed. D. Fink, Springer-Verlag Berlin Heidelberg, 2004, pp. 147–202.
142 C. Trautmann, W. Brüchle, R. Spohr, J. Vetter and N. Angert, *Nucl. Instrum. Methods Phys. Res., Sect. B*, 1996, **111**, 70–74.
143 G. Pérez-Mitta, W. A. Marmisollé, A. G. Albesa, M. E. Toimil-Molares, C. Trautmann and O. Azzaroni, *Small*, 2018, **14**, 1702131.
144 G. Pérez-Mitta, A. G. Albesa, W. Knoll, C. Trautmann, M. E. Toimil-Molares and O. Azzaroni, *Nanoscale*, 2015, **7**, 15594–15598.
145 L. C. T. Man, P. Apel, T. Cheung, L. Westerberg, K. N. Yu, C. Zet and R. Spohr, *Nucl. Instrum. Methods Phys. Res., Sect. B*, 2007, **265**, 621–625.
146 P. Y. Apel, I. V. Blonskaya, S. N. Dmitriev, O. L. Orelovitch, A. Presz and B. A. Sartowska, *Nanotechnology*, 2007, **18**, 305302.
147 Z. Siwy and A. Fuliński, *Phys. Rev. Lett.*, 2002, **89**, 4–7.
148 G. Laucirica, V. M. Cayón, Y. Toum Terrones, M. L. Cortez, M. E. Toimil-Molares, C. Trautmann, W. A. Marmisollé and O. Azzaroni, *Nanoscale*, 2020, **12**, 6002–6011.
149 N. Li, D. T. Mitchell, K.-P. Lee and C. R. Martin, *J. Electrochem. Soc.*, 2003, **150**, A979.
150 H. Masuda and K. Fukuda, *Science*, 1995, **268**, 1466–1468.
151 R. C. Furneaux, W. R. Rigby and A. P. Davidson, *Nature*, 1989, **337**, 147–149.
152 J. H. Yuan, F. Y. He, D. C. Sun and X. H. Xia, *Chem. Mater.*, 2004, **16**, 1841–1844.
153 L. A. Baker, P. Jin and C. R. Martin, *Crit. Rev. Solid State Mater. Sci.*, 2005, **30**, 183–205.
154 A.-L. Biance, J. Gierak, É. Bourhis, A. Madouri, X. Lafosse, G. Patriarche, G. Oukhaled, C. Ulysse, J.-C. Galas, Y. Chen and L. Auvray, *Microelectron. Eng.*, 2006, **83**, 1474–1477.
155 J. Gierak, A. Madouri, A. L. Biance, E. Bourhis, G. Patriarche, C. Ulysse, D. Lucot, X. Lafosse, L. Auvray, L. Bruchhaus and R. Jede, *Microelectron. Eng.*, 2007, **84**, 779–783.
156 P. Chen, M.-Y. Wu, H. W. M. Salemink and P. F. A. Alkemade, *Nanotechnology*, 2009, **20**, 015302.
157 J. Li, M. Gershow, D. Stein, E. Brandin and J. A. Golovchenko, *Nat. Mater.*, 2003, **2**, 611–615.
158 J. Li, D. Stein, C. McMullan, D. Branton, M. J. Aziz and J. A. Golovchenko, *Nature*, 2001, **412**, 166–169.
159 J. Feng, K. Liu, M. Graf, M. Lihter, R. D. Bulushev, D. Dumcenco, D. T. L. Alexander, D. Krasnozhon, T. Vuletic, A. Kis and A. Radenovic, *Nano Lett.*, 2015, **15**, 3431–3438.
160 A. J. Storm, J. H. Chen, X. S. Ling, H. W. Zandbergen and C. Dekker, *Nat. Mater.*, 2003, **2**, 537–540.
161 S. Liu, Q. Zhao, J. Xu, K. Yan, H. Peng, F. Yang, L. You and D. Yu, *Nanotechnology*, 2012, **23**, 085301.
162 J. B. Heng, C. Ho, T. Kim, R. Timp, A. Aksimentiev, Y. V. Grinkova, S. Sligar, K. Schulten and G. Timp, *Biophys. J.*, 2004, **87**, 2905–2911.
163 A. J. Storm, J. H. Chen, X. S. Ling, H. W. Zandbergen and C. Dekker, *J. Appl. Phys.*, 2005, **98**, 014307.
164 M. J. Kim, M. Wanunu, D. C. Bell and A. Meller, *Adv. Mater.*, 2006, **18**, 3149–3153.
165 S. Garaj, S. Liu, J. A. Golovchenko and D. Branton, *Proc. Natl. Acad. Sci. U. S. A.*, 2013, **110**, 12192–12196.
166 K. Xiao, P. Giusto, L. Wen, L. Jiang and M. Antonietti, *Angew. Chem., Int. Ed.*, 2018, **57**, 10123–10126.
167 H. Gao, W. Chen, C. Xu, S. Liu, X. Tong and Y. Chen, *Environ. Sci. Technol.*, 2020, **54**, 2931–2940.
168 W. Guo, C. Cheng, Y. Wu, Y. Jiang, J. Gao, D. Li and L. Jiang, *Adv. Mater.*, 2013, **25**, 6064–6068.
169 L. Zhang, S. Zhou, L. Xie, L. Wen, J. Tang, K. Liang, X. Kong, J. Zeng, R. Zhang, J. Liu, B. Qiu, L. Jiang and B. Kong, *Small*, 2021, **17**, 2100141.
170 Z. Zhang, P. Zhang, S. Yang, T. Zhang, M. Löffler, H. Shi, M. R. Lohe and X. Feng, *Proc. Natl. Acad. Sci. U. S. A.*, 2020, **117**, 13959–13966.
171 H. Cheng, Y. Zhou, Y. Feng, W. Geng, Q. Liu, W. Guo and L. Jiang, *Adv. Mater.*, 2017, **29**, 1700177.

172 C. Zhu, P. Liu, B. Niu, Y. Liu, W. Xin, W. Chen, X.-Y. Kong, Z. Zhang, L. Jiang and L. Wen, *J. Am. Chem. Soc.*, 2021, **143**, 1932–1940.

173 G.-R. Xu, J.-M. Xu, H.-C. Su, X.-Y. Liu, L. Lu-Li, H.-L. Zhao, H.-J. Feng and R. Das, *Desalination*, 2019, **451**, 18–34.

174 H. E. Karahan, K. Goh, C. Zhang, E. Yang, C. Yıldırım, C. Y. Chuah, M. G. Ahunbay, J. Lee, Ş. B. Tantekin-Ersolmaz, Y. Chen and T. Bae, *Adv. Mater.*, 2020, **32**, 1906697.

175 S. Hong, F. Ming, Y. Shi, R. Li, I. S. Kim, C. Y. Tang, H. N. Alshareef and P. Wang, *ACS Nano*, 2019, **13**, 8917–8925.

176 J. Li, X. Li and B. Van der Bruggen, *Environ. Sci.: Nano*, 2020, **7**, 1289–1304.

177 C. E. Ren, K. B. Hatzell, M. Alhabeb, Z. Ling, K. A. Mahmoud and Y. Gogotsi, *J. Phys. Chem. Lett.*, 2015, **6**, 4026–4031.

178 Y. Zhu, S. Murali, W. Cai, X. Li, J. W. Suk, J. R. Potts and R. S. Ruoff, *Adv. Mater.*, 2010, **22**, 3906–3924.

179 Z. Jakšić and O. Jakšić, *Biomimetics*, 2020, **5**, 24.

180 T. Ma, E. Balanzat, J.-M. Janot and S. Balme, *ACS Appl. Mater. Interfaces*, 2019, **11**, 12578–12585.

181 S. Hou, Q. Zhang, Z. Zhang, X. Kong, B. Lu, L. Wen and L. Jiang, *Nano Energy*, 2021, **79**, 105509.

182 Y. Xu, Y. Song and F. Xu, *Nano Energy*, 2021, **79**, 105468.

183 W. Chen, Q. Zhang, Y. Qian, W. Xin, D. Hao, X. Zhao, C. Zhu, X. Kong, B. Lu, L. Jiang and L. Wen, *ACS Cent. Sci.*, 2020, **6**, 2097–2104.

184 J.-M. Koo, C. H. Park, S. Yoo, G. W. Lee, S. Y. Yang, J. H. Kim and S. Il Yoo, *Soft Matter*, 2021, **17**, 3700–3708.

185 L. Wang, Z. Wang, S. K. Patel, S. Lin and M. Elimelech, *ACS Nano*, 2021, **15**, 4093–4107.

186 C. Lin, C. Combs, Y. Su, L. Yeh and Z. S. Siwy, *J. Am. Chem. Soc.*, 2019, **141**, 3691–3698.

187 G. Pérez-Mitta, A. G. Albesa, C. Trautmann, M. E. Toimil-Molares and O. Azzaroni, *Chem. Sci.*, 2017, **8**, 890–913.

188 Y. He, Z. Huang, B. Chen, M. Tsutsui, X. Shui Miao and M. Taniguchi, *Sci. Rep.*, 2017, **7**, 13156.

189 B. D. Kang, H. J. Kim, M. G. Lee and D.-K. Kim, *Energy*, 2015, **86**, 525–538.

190 Y. Zhang, Z. Huang, Y. He and X. Miao, *Nanotechnology*, 2019, **30**, 428–429.

191 F. Yan, L. Yao, K. Chen, Q. Yang and B. Su, *J. Mater. Chem. A*, 2019, **7**, 2385–2391.

192 R. Long, M. Li, X. Chen, Z. Liu and W. Liu, *Int. J. Heat Mass Transfer*, 2021, **171**, 121126.

193 L. Cao, F. Xiao, Y. Feng, W. Zhu, W. Geng, J. Yang, X. Zhang, N. Li, W. Guo and L. Jiang, *Adv. Funct. Mater.*, 2017, **27**, 1604302.

194 Y.-S. Su, S.-C. Hsu, P.-H. Peng, J.-Y. Yang, M. Gao and L.-H. Yeh, *Nano Energy*, 2021, **84**, 105930.

195 L. Cao, Q. Wen, Y. Feng, D. Ji, H. Li, N. Li, L. Jiang and W. Guo, *Adv. Funct. Mater.*, 2018, **28**, 1804189.

196 K. Yazda, K. Bleau, Y. Zhang, X. Capaldi, T. St-Denis, P. Grutter and W. W. Reisner, *Nano Lett.*, 2021, **21**, 4152–4159.

197 J. Gao, X. Liu, Y. Jiang, L. Ding, L. Jiang and W. Guo, *Small*, 2019, **15**, 1804279.

198 W.-C. Huang and J.-P. Hsu, *Electrochim. Acta*, 2020, **353**, 136613.

199 J.-P. Hsu, T.-C. Su, P.-H. Peng, S.-C. Hsu, M.-J. Zheng and L.-H. Yeh, *ACS Nano*, 2019, **13**, 13374–13381.

200 L.-H. Yeh, F. Chen, Y.-T. Chiou and Y.-S. Su, *Small*, 2017, **13**, 1702691.

201 M. Graf, M. Lihter, D. Unuchek, A. Sarathy, J.-P. Leburton, A. Kis and A. Radenovic, *Joule*, 2019, **3**, 1549–1564.

202 K. Xiao, P. Giusto, F. Chen, R. Chen, T. Heil, S. Cao, L. Chen, F. Fan and L. Jiang, *Natl. Sci. Rev.*, 2021, **8**(8), nwaa231.

203 P. Liu, T. Zhou, Y. Teng, L. Fu, Y. Hu, X. Lin, X.-Y. Kong, L. Jiang and L. Wen, *CCS Chem.*, 2020, 1325–1335.

204 L.-H. Yeh, Z.-Y. Huang, Y.-C. Liu, M.-J. Deng, T.-H. Chou, H.-C. Ou Yang, T. Ahamad, S. M. Alshehri and K. C.-W. Wu, *J. Mater. Chem. A*, 2019, **7**, 26791–26796.

205 S. Balme, T. Ma, E. Balanzat and J. Janot, *J. Membr. Sci.*, 2017, **544**, 18–24.

206 K. H. Lee, H. Park, W. Eom, D. J. Kang, S. H. Noh and T. H. Han, *J. Mater. Chem. A*, 2019, **7**, 23727–23732.

207 M. Khatibi, A. Sadeghi and S. N. Ashrafizadeh, *Phys. Chem. Chem. Phys.*, 2021, **23**, 2211–2221.

208 Z. Zhang, S. Yang, P. Zhang, J. Zhang, G. Chen and X. Feng, *Nat. Commun.*, 2019, **10**, 2920.

209 Z. Zhang, X. Sui, P. Li, G. Xie, X. Y. Kong, K. Xiao, L. Gao, L. Wen and L. Jiang, *J. Am. Chem. Soc.*, 2017, **139**, 8905–8914.

210 H.-C. Yang, Y. Xie, J. Hou, A. K. Cheetham, V. Chen and S. B. Darling, *Adv. Mater.*, 2018, **30**, 1801495.

211 H. Li, F. Xiao, G. Hong, J. Su, N. Li, L. Cao, Q. Wen and W. Guo, *Chin. J. Chem.*, 2019, **37**, 469–473.

212 S. Lee, H. Kim and D.-K. Kim, *Energies*, 2016, **9**, 49.

213 J. Hwang, S. Kataoka, A. Endo and H. Daiguji, *Lab Chip*, 2016, **16**, 3824–3832.

214 M. Tagliazucchi, O. Azzaroni and I. Szleifer, *J. Am. Chem. Soc.*, 2010, **132**, 12404–12411.

215 Z. Siwy, I. D. Kosińska, A. Fuliński and C. R. Martin, *Phys. Rev. Lett.*, 2005, **94**, 048102.

216 R. Long, Z. Kuang, Z. Liu and W. Liu, *Phys. Chem. Chem. Phys.*, 2018, **20**, 7295–7302.

217 J. Cervera, B. Schiedt, R. Neumann, S. Mafé and P. Ramírez, *J. Chem. Phys.*, 2006, **124**, 104706.

218 R. Li, J. Jiang, Q. Liu, Z. Xie and J. Zhai, *Nano Energy*, 2018, **53**, 643–649.

219 J. Gao, W. Guo, D. Feng, H. Wang, D. Zhao and L. Jiang, *J. Am. Chem. Soc.*, 2014, **136**, 12265–12272.

220 L. Cao, W. Guo, W. Ma, L. Wang, F. Xia, S. Wang, Y. Wang, L. Jiang and D. Zhu, *Energy Environ. Sci.*, 2011, **4**, 2259–2266.

221 H. Zhang, J. Hou, Y. Hu, P. Wang, R. Ou, L. Jiang, J. Z. Liu, B. D. Freeman, A. J. Hill and H. Wang, *Sci. Adv.*, 2018, **4**, eaaq0066.

222 J. Lu, H. Zhang, J. Hou, X. Li, X. Hu, Y. Hu, C. D. Easton, Q. Li, C. Sun, A. W. Thornton, M. R. Hill, X. Zhang,

G. Jiang, J. Z. Liu, A. J. Hill, B. D. Freeman, L. Jiang and H. Wang, *Nat. Mater.*, 2020, **19**, 767–774.
223 X. Li, H. Zhang, P. Wang, J. Hou, J. Lu, C. D. Easton, X. Zhang, M. R. Hill, A. W. Thornton, J. Z. Liu, B. D. Freeman, A. J. Hill, L. Jiang and H. Wang, *Nat. Commun.*, 2019, **10**, 2490.
224 Y.-C. Liu, L.-H. Yeh, M.-J. Zheng and K. C.-W. Wu, *Sci. Adv.*, 2021, **7**, eabe9924.
225 R. Long, Z. Kuang, Z. Liu and W. Liu, *J. Membr. Sci.*, 2018, **561**, 1–9.
226 Y. Fu, X. Guo, Y. Wang, X. Wang and J. Xue, *Nano Energy*, 2019, **57**, 783–790.
227 J. Hwang, T. Sekimoto, W.-L. Hsu, S. Kataoka, A. Endo and H. Daiguji, *Nanoscale*, 2017, **9**, 12068–12076.
228 Y. Wu, W. Xin, X.-Y. Kong, J. Chen, Y. Qian, Y. Sun, X. Zhao, W. Chen, L. Jiang and L. Wen, *Mater. Horiz.*, 2020, **7**, 2702–2709.
229 R. Long, Z. Kuang, Z. Liu and W. Liu, *Natl. Sci. Rev.*, 2019, **6**, 1266–1273.
230 V.-P. Mai and R.-J. Yang, *Appl. Energy*, 2020, **274**, 115294.
231 K. Chen, L. Yao, F. Yan, S. Liu, R. Yang and B. Su, *J. Mater. Chem. A*, 2019, **7**, 25258–25261.
232 A. Tamburini, M. Tedesco, A. Cipollina, G. Micale, M. Ciofalo, M. Papapetrou, W. Van Baak and A. Piacentino, *Appl. Energy*, 2017, **206**, 1334–1353.
233 Z. Zhang, W. Shen, L. Lin, M. Wang, N. Li, Z. Zheng, F. Liu and L. Cao, *Adv. Sci.*, 2020, **7**, 2000286.
234 C. Wu, T. Xiao, J. Tang, Q. Zhang, Z. Liu, J. Liu and H. Wang, *Nano Energy*, 2020, **76**, 105113.
235 M. I. Walker, K. Ubych, V. Saraswat, E. A. Chalklen, P. Braeuninger-Weimer, S. Caneva, R. S. Weatherup, S. Hofmann and U. F. Keyser, *ACS Nano*, 2017, **11**, 1340–1346.
236 W. Xin, H. Xiao, X.-Y. Kong, J. Chen, L. Yang, B. Niu, Y. Qian, Y. Teng, L. Jiang and L. Wen, *ACS Nano*, 2020, **14**, 9701–9710.
237 X. Zhu, Y. Zhou, J. Hao, B. Bao, X. Bian, X. Jiang, J. Pang, H. Zhang, Z. Jiang and L. Jiang, *ACS Nano*, 2017, **11**, 10816–10824.
238 C. Chen, D. Liu, G. Yang, J. Wang, L. Wang and W. Lei, *Adv. Energy Mater.*, 2020, **10**, 1904098.
239 M. Naguib, M. Kurtoglu, V. Presser, J. Lu, J. Niu, M. Heon, L. Hultman, Y. Gogotsi and M. W. Barsoum, *Adv. Mater.*, 2011, **23**, 4248–4253.
240 V. M. Hong Ng, H. Huang, K. Zhou, P. S. Lee, W. Que, J. Z. Xu and L. B. Kong, *J. Mater. Chem. A*, 2017, **5**, 3039–3068.
241 P. Liu, Y. Sun, C. Zhu, B. Niu, X. Huang, X.-Y. Kong, L. Jiang and L. Wen, *Nano Lett.*, 2020, **20**, 3593–3601.
242 S. Qin, D. Liu, Y. Chen, C. Chen, G. Wang, J. Wang, J. M. Razal and W. Lei, *Nano Energy*, 2018, **47**, 368–373.
243 C. Chen, D. Liu, X. Qing, G. Yang, X. Wang and W. Lei, *ACS Appl. Mater. Interfaces*, 2020, **12**, 52771–52778.
244 X. Zhu, J. Zhong, J. Hao, Y. Wang, J. Zhou, J. Liao, Y. Dong, J. Pang, H. Zhang, Z. Wang, W. Zhang, W. Zheng, Z. Jiang, Y. Zhou and L. Jiang, *Adv. Energy Mater.*, 2020, **10**, 2001552.
245 Y. Sun, T. Dong, C. Lu, W. Xin, L. Yang, P. Liu, Y. Qian, Y. Zhao, X. Kong, L. Wen and L. Jiang, *Angew. Chem., Int. Ed.*, 2020, **59**, 17423–17428.
246 W. Chen, Q. Wang, J. Chen, Q. Zhang, X. Zhao, Y. Qian, C. Zhu, L. Yang, Y. Zhao, X.-Y. Kong, B. Lu, L. Jiang and L. Wen, *Nano Lett.*, 2020, **20**, 5705–5713.
247 J. Lu, H. Zhang, X. Hu, B. Qian, J. Hou, L. Han, Y. Zhu, C. Sun, L. Jiang and H. Wang, *ACS Nano*, 2021, **15**, 1240–1249.
248 S. Hou, W. Ji, J. Chen, Y. Teng, L. Wen and L. Jiang, *Angew. Chem., Int. Ed.*, 2021, **60**, 9925–9930.
249 X. Zhao, C. Lu, L. Yang, W. Chen, W. Xin, X.-Y. Kong, Q. Fu, L. Wen, G. Qiao and L. Jiang, *Nano Energy*, 2021, **81**, 105657.
250 S. Zhou, L. Xie, L. Zhang, L. Wen, J. Tang, J. Zeng, T. Liu, D. Peng, M. Yan, B. Qiu, Q. Liang, K. Liang, L. Jiang and B. Kong, *ACS Appl. Mater. Interfaces*, 2021, **13**, 8782–8793.
251 S. H. Kwak, S.-R. Kwon, S. Baek, S.-M. Lim, Y.-C. Joo and T. D. Chung, *Sci. Rep.*, 2016, **6**, 26416.
252 X. Sui, Z. Zhang, C. Li, L. Gao, Y. Zhao, L. Yang, L. Wen and L. Jiang, *ACS Appl. Mater. Interfaces*, 2019, **11**, 23815–23821.
253 T. Xiao, Q. Zhang, J. Jiang, J. Ma, Q. Liu, B. Lu, Z. Liu and J. Zhai, *Energy Technol.*, 2018, **7**, 1800952.
254 A. Pendse, S. Cetindag, P. Rehak, S. Behura, H. Gao, N. H. L. Nguyen, T. Wang, V. Berry, P. Král, J. Shan and S. Kim, *Adv. Funct. Mater.*, 2021, 2009586.
255 L. Xie, S. Zhou, J. Liu, B. Qiu, T. Liu, Q. Liang, X. Zheng, B. Li, J. Zeng, M. Yan, Y. He, X. Zhang, H. Zeng, D. Ma, P. Chen, K. Liang, L. Jiang, Y. Wang, D. Zhao and B. Kong, *J. Am. Chem. Soc.*, 2021, **143**, 6922–6932.
256 W. Xin, Z. Zhang, X. Huang, Y. Hu, T. Zhou, C. Zhu, X. Kong, L. Jiang and L. Wen, *Nat. Commun.*, 2019, **10**, 3876.
257 K. Kwon, S. J. Lee, L. Li, C. Han and D. Kim, *Int. J. Energy Res.*, 2014, **38**, 530–537.
258 Z. Zhang, X. Y. Kong, K. Xiao, Q. Liu, G. Xie, P. Li, J. Ma, Y. Tian, L. Wen and L. Jiang, *J. Am. Chem. Soc.*, 2015, **137**, 14765–14772.
259 Q.-Y. Wu, C. Wang, R. Wang, C. Chen, J. Gao, J. Dai, D. Liu, Z. Lin and L. Hu, *Adv. Energy Mater.*, 2019, **10**, 1902590.
260 D. A. Vermaas, J. Veerman, M. Saakes and K. Nijmeijer, *Energy Environ. Sci.*, 2014, **7**, 1434–1445.
261 O. Schaetzle and C. J. N. Buisman, *Engineering*, 2015, **1**, 164–166.
262 D. A. Vermaas, D. Kunteng, J. Veerman, M. Saakes and K. Nijmeijer, *Environ. Sci. Technol.*, 2014, **48**, 3065–3073.
263 F. Kotoka, I. Merino-Garcia and S. Velizarov, *Membranes*, 2020, **10**, 160.
264 D. Pintossi, M. Saakes, Z. Borneman and K. Nijmeijer, *ACS Appl. Mater. Interfaces*, 2021, **13**, 18348–18357.
265 R. A. Tufa, E. Rugiero, D. Chanda, J. Hnàt, W. van Baak, J. Veerman, E. Fontananova, G. Di Profio, E. Drioli, K. Bouzek and E. Curcio, *J. Membr. Sci.*, 2016, **514**, 155–164.
266 R. A. Tufa, J. Hnát, M. Němeček, R. Kodým, E. Curcio and K. Bouzek, *J. Cleaner Prod.*, 2018, **203**, 418–426.
267 X. Chen, C. Jiang, Y. Zhang, Y. Wang and T. Xu, *J. Membr. Sci.*, 2017, **544**, 397–405.

268 X. Chen, C. Jiang, M. A. Shehzad, Y. Wang, H. Feng, Z. Yang and T. Xu, *ACS Sustainable Chem. Eng.*, 2019, **7**, 13023–13030.
269 J.-Y. Nam, R. D. Cusick, Y. Kim and B. E. Logan, *Environ. Sci. Technol.*, 2012, **46**, 5240–5246.
270 X. Li, I. Angelidaki and Y. Zhang, *Water Res.*, 2018, **142**, 396–404.
271 Y. Kim and B. E. Logan, *Environ. Sci. Technol.*, 2011, **45**, 5834–5839.
272 X. Zhu, T. Kim, M. Rahimi, C. A. Gorski and B. E. Logan, *ChemSusChem*, 2017, **10**, 797–803.
273 J.-H. Kim, J.-H. Lee, S. Maurya, S.-H. Shin, J.-Y. Lee, I. S. Chang and S.-H. Moon, *Electrochem. Commun.*, 2016, **72**, 157–161.
274 W. J. van Egmond, M. Saakes, S. Porada, T. Meuwissen, C. J. N. Buisman and H. V. M. Hamelers, *J. Power Sources*, 2016, **325**, 129–139.
275 F. E. Ahmed, R. Hashaikeh and N. Hilal, *Desalination*, 2020, **495**, 114659.
276 K. Kwon, J. Han, B. H. Park, Y. Shin and D. Kim, *Desalination*, 2015, **362**, 1–10.
277 R. A. Tufa, Y. Noviello, G. Di Profio, F. Macedonio, A. Ali, E. Drioli, E. Fontananova, K. Bouzek and E. Curcio, *Appl. Energy*, 2019, **253**, 113551.
278 W. Li, W. B. Krantz, E. R. Cornelissen, J. W. Post, A. R. D. Verliefde and C. Y. Tang, *Appl. Energy*, 2013, **104**, 592–602.
279 A. Zoungrana and M. Çakmakci, *Int. J. Energy Res.*, 2021, **45**, 3495–3522.
280 C. Tristán, M. Rumayor, A. Dominguez-Ramos, M. Fallanza, R. Ibáñez and I. Ortiz, *Sustainable Energy Fuels*, 2020, **4**, 4273–4284.
281 R. A. Tufa, E. Curcio, E. Brauns, W. van Baak, E. Fontananova and G. Di Profio, *J. Membr. Sci.*, 2015, **496**, 325–333.
282 X. Luo, X. Cao, Y. Mo, K. Xiao, X. Zhang, P. Liang and X. Huang, *Electrochem. Commun.*, 2012, **19**, 25–28.
283 R. Long, B. Li, Z. Liu and W. Liu, *J. Membr. Sci.*, 2017, **525**, 107–115.
284 M. Papapetrou, G. Kosmadakis, F. Giacalone, B. Ortega-Delgado, A. Cipollina, A. Tamburini and G. Micale, *Energies*, 2019, **12**, 3206.
285 D. A. Vermaas, E. Guler, M. Saakes and K. Nijmeijer, *Energy Procedia*, 2012, **20**, 170–184.
286 E. Brauns, *Desalination*, 2008, **219**, 312–323.
287 O. Scialdone, A. D'Angelo, E. De Lumè and A. Galia, *Electrochim. Acta*, 2014, **137**, 258–265.
288 O. Scialdone, A. D'Angelo and A. Galia, *J. Electroanal. Chem.*, 2015, **738**, 61–68.
289 J. Chen, W. Xin, X.-Y. Kong, Y. Qian, X. Zhao, W. Chen, Y. Sun, Y. Wu, L. Jiang and L. Wen, *ACS Energy Lett.*, 2020, **5**, 742–748.
290 L. Fu, J. Jiang, B. Lu, Y. Xu and J. Zhai, *ChemNanoMat*, 2019, **5**, 1182–1187.